BIOMIMETIC MEMBRANES EMBEDDED WITH AQUAPORINZ FOR WATER REUSE AND DESALINATION

Wang Honglei

NATIONAL UNIVERSITY OF SINGAPORE

2012

BIOMIMETIC MEMBRANES EMBEDDED WITH AQUAPORINZ FOR WATER REUSE AND DESALINATION

Wang Honglei

A THESIS SUBMITTED

FOR THE DEGREE OF DOCTOR OF PHILOSOPHY

DEPARTMENT OF CHEMICAL AND BIOMOLECULAR ENGINEERING

NATIONAL UNIVERSITY OF SINGAPORE

2012

ACKNOWLEDGEMENT

First of all, I would like to express my sincere appreciation to my PhD thesis committee members, Prof. Chen Shing Bor and Prof. Jiang Jianwen. Their suggestions to my PhD proposal have been constructive throughout my candidature in NUS.

This work is a multidisciplinary work. Therefore, I really appreciate the work that has been done by our collaborators from Department of Biochemistry, Department of Biological Science and Department of Electrical Engineering. Firstly, I would like thank my supervisors Prof. Tai-Shung Chung and Prof. Yen Wah Tong. I would like to thank Prof. Chung for his encouragement and supervision during my research study and his special force to push this project. He provided many opportunities for me to learn from oversea membrane experts. I am also grateful of his trust to let me in charge of the biomimetic research project for the past 3 years, which provides me a precious opportunity to advance my management skills and leadership in the team.

I would like to think Prof. Tong for his education to me and contribution to my research. Prof. Tong trained me how to get some crazy ideas and run through them critically. His clear mind as well as his knowledge helped me to overcome many scientific problems and helped me to find a solution. In his group, I have learnt how to analyze a problem logically, how to argue and defense my study, and how to organize a sound presentation.

I would like to thank Prof. Kandiah Jeyaseelan and Dr. Armugam Arunmozhiarasi, who are biochemistry experts, for continuously providing me precious Aquaporin Z samples and guidance through my PhD study. They also provided intriguing suggestions to my research. We have had a good time in working together to optimize the purification of Aquaporin Z.

I would like to thank Prof. Minghui Hong for his collaboration, his ideas and comments to my research and to my manuscript preparation. He helped me with great professional advices and shared with me his experience. He and his students helped me to try out some crazy ideas. Even though the results were frustrated most of the time, they were always patient and supportive.

I would like to thank Dr. Wolfgang Meier for his collaboration. Our researches were inspired by some of his work and a frequently used block copolymer PMOXA-PDMS-PMOXA. We learnt polymer synthesis and Aquaporin incorporation from his group. I am deeply grateful for all the help that has been provided from him and his group in the University of Basel.

I would like to acknowledge the financial support by the Environment and Water Industry Programme Office (EWI) (NUS grant number: R-279-000-293-272) under the Singapore National Research Foundation (NRF).

I would like to convey my personal appreciation of all the former and current members in our research group, especially, Dr. Li Yi and Dr. Xie Wenyuan for their invaluable suggestions and sharing of technical expertise. I developed friendships with the members in both Prof. Chung's and Prof. Tong's groups, which renders my study in NUS so pleasant.

Last but not least, I would like to express my gratitude to my parents and my family for their unconditional love and support. I would also like to thank my boyfriend Mr. Dai Mengqiao who makes my life in NUS memorable and enjoyable.

TABLE OF CONTENTS

SUMMARY

Fresh water scarcity is one of the problems that the whole world is facing today. Forward osmosis and low pressure reverse osmosis are solutions to provide high quality water from water treatment and seawater desalination. Thus, creating a robust and highly permeable yet selective membrane for water purification has gained much attention worldwide in recent years. In this thesis, a systematic study on the design and fabrication of AquaporinZ (AqpZ)-embedded biomimetic membrane is presented.

Firstly, the fundamental science of the mechanical property of the artificial AqpZ-embedded lipid bilayer membrane was established, with an emphasis on three aspects: (1) the membrane design strategy, (2) the coverage of resulted membrane on a porous support and (3) the local mechanical stability. It is found that the surface coverage of biomimetic membrane on the carboxylated-PEG coated substrate is 5-fold higher compared with that on the pristine porous alumina. In addition, the local membrane mechanical stability indicates the flexibility of the DMPC bilayer on the substrate is drastically improved by a layer of carboxylated-PEG polymer cushion and that AqpZ increases the energy barrier required for a normal force to punch through the resultant biomimetic membrane. Therefore, the carboxylated-PEG grafted porous alumina exhibits a promising platform for the fabrication of pore-spanning biomimetic membranes.

Secondly, a new biomimetic membrane configuration has been designed and its feasibility in water purification has been demonstrated. A pore-spanning biomimetic

membrane embedded with AqpZ has been fabricated via a combination of surface modification followed by pressure-assisted vesicle adsorption and finally, covalent conjugation-driven vesicle fusion onto a porous support. A critical pressure that is applied to push the vesicles against the polycarbonate track etched (PCTE) support is the key to improve the surface coverage of the biomimetic membrane. A subsequent UV crosslinking that induces vesicle to rupture further enhances the mechanical stability of the thin film. The water flux of the resulted biomimetic membrane embedded with AqpZ shows a positively increase as the increase of AqpZ contents in forward osmosis (FO), indicating a high coverage of biomimetic membrane on the support has also been achieved by using this method. The proposed AqpZ-embedded pore-spanning membrane design has shifted the water transport mechanism from solution-diffusion to channel mediated transport.

Thirdly, a new membrane configuration has been proposed to enhance the robust property and maintain high permeability and selectivity of the membrane. The desired membrane has been prepared using the concept of layer-by-layer thin film coating. Meanwhile, the correlation between PDA coating strategy and the separation performance of the resulted membrane has been discussed. The vesicular biomimetic membrane is fabricated by crosslinking AqpZ-embedded block copolymer vesicles, followed by immobilizing vesicles on the membrane support via covalent bonding, and then stabilizing through an optimized layer-by-layer polydopamine (PDA)-histidine (His) coating process. It is worth to emphasize that the current vesicular membrane is sufficiently robust to withstand tangential flow during FO tests. Thus, the vesicular

membrane design may provide new insights into the fabrication of Aqp-embedded biomimetic membranes.

Finally, water transport through the robust AqpZ-embedded vesicular membrane has been investigated through a newly modified transport model in a FO process. A series of data have been obtained in order to correlate the influences of vesicle size, vesicle permeability and concentration of the encapsulated salt inside the vesicle. Simulation indicates that both vesicle size and permeability have dominant effects on water flux, while the interior solute concentration of vesicles will mainly impact the hydrostatic pressure of the vesicles. Central to the performance of this vesicular membrane in FO is the synergy of (1) desirable vesicle size and (2) high vesicle permeability which is equivalent to high AqpZ density incorporated in the vesicle. This study provides a direction for the further development of the AqpZ-incorporated membrane for water purification.

NOMENCLATURE

a_i	area fraction, A_i/A_T
A	water permeability
A_e	the membrane area prepared in the experiment
A_i	area of the ith region
A_m	area of the membrane support (19.6 mm^2)
A_p	area of a single pore (1.96×10^{-9} mm^2)
A_{RO}	RO membrane area
A_s	constant (always negative)
A_T	total surface area of the vesicle
A_{tot}	total membrane area
B	solute permeability
c_{ABA}	concentration of vesicle
C_1	concentrations of NaCl near the surface of the vesicular membrane in compartments 1
C_2	concentrations of NaCl near the surface of the vesicular membrane in compartments 2
C_{2b}	bulk concentration of NaCl in compartment 2
C_{ABA}	total cost of the selective layer
C_{d1}	final salt concentration of the draw solution
C_{f0}	initial salt concentration of the feed
C_{in}	inlet salt concentration
C_{out}	outlet salt concentration
$C_v(t)$	NaCl concentration inside the vesicle

E_{2D}	Young's modulus in N/m
F	indentation force
h	penetration depth, in nm
h_{depth}	theoretical maximal penetration depth
J_m	membrane flux at steady state
J_s	solute flux in general
$\vec{J}_v(i)$	water volume flux evaluated at the start of the i-th time interval
$J_{v,in}$	absolute values of water flow in the vesicles
$J_{v,out}$	absolute values of water flow out of the vesicles
J_{vs}	net steady state water flux
J_w	water flux in general
k	initial rate constant, in s^{-1}
$L_{i(i=1,2)}$	hydraulic permeability coefficient of the membrane region in the ith compartment
L_p	hydraulic permeability coefficient
$L_{p,RO}$	Conventional RO membrane permeability
m_c	mass flux
m_{p1}	amount of AqpZ consumed in the membrane preparation
M_{ABA}	molecular weight of ABA block copolymer
M_p	molecular weight of AqpZ
M_s	molecular weights of NaCl
M_v	molecular weight of a vesicle
M_w	molecular weight of water
N_A	Avogardro's number

N_{ABA}	number of ABA block copolymer units
N_{AqpZ}	number of incorporated AqpZ subunits
N_v	number of vesicles that have been immobilized on the pores
$\overline{NDP}$	net transmembrane driving pressure
P_0	pressure of permeate
P_f	vesicle permeability
$P_{f,\,vesicle}$	average permeability of vesicles
$P_{f,in}$	feed inlet pressure
$P_{f,out}$	feed outlet pressure
Q_f	feed inlet flowrate
Q_p	permeate flowrate
r	radius of the pore, in nm
$r_{ABA/p}$	molar ratio of ABA to AqpZ
r_w	water recovery
R	gas constant
R_h	radius of the assumed hemisphere, in nm
R_{pore}	radius of the pore, in nm
R_{tip}	radius of the tip, in nm
R_v	vesicle radius
S	pore-spanning membrane area, in nm^2
S_m	membrane area, in m^2
SEC	specific energy consumption
t	t is the recording time, in s
T	Temperature, in K

$V(t)$	vesicle volume
V_0	initial vesicle volume
V_f	final volume the feed, in mL
V_{pre}	volume that is comsumed to prepare the selective layer
V_w	partial molar volume of water
$\dot{W}$	rate of work done by the pump
Y	intensity of signal
Δ_{osm}	osmotic driving force, osmolarity
ΔC_f	salt concentration change of the feed, in g/mL
ΔC_s	solute concentration difference between the feed and the permeate solutions
ΔP	hydrostatic pressure difference between the inside of the vesicle and the outside solution
ΔPc	pressure difference between the entrance and the exit of the channel
ΔS	dilatation area, in nm^2
Δt	time interval
ΔW	the weight increase of draw solution over timing Δt
$\Delta\pi$	osmotic pressure difference between the feed and the permeate solutions
$\Delta\pi_b$	bulk osmotic pressure
$\Delta\pi_{eff}$	osmotic pressure across the selective layer
$\Delta\pi_m$	osmotic pressure across the membrane
Ω	elastic energy stored in the membrane
δ	wall thickness of vesicle
ε	porosity

θ	angle, in degree
λ	molecularity. In the case of NaCl, λ=2
μ	viscosity of solution
v	specific volume of a vesicle (~1 cm^3/g)
π_{in}	osmotic pressure of inlet flow
π_{out}	osmotic pressure of brine flow
ρ	solution density
σ	reflection coefficient, is assumed to be 1
σ_s	lateral tension, in N/m

Abbreviation

AFM	Atomic Force Microscope
Aqp	Aquaporin
Aqp1	Aquaporin1
AqpZ	AquaporinZ
ar/R	aromatic/arginine
CHIP28	channel-like integral protein of 28 kDa
CP	Concentration polarization
DDM	dodecyl-β-d-maltoside
DLS	dynamic light scattering
DMPC	1,2-dimyristoyl-sn-glycero-3-phosphocholine
ECP	External concentration polarization
FESEM	Field Emission Scanning Electron Microscopy

FITC	fluorescein isothiocyanate
FO	Forward Osmosis
FT-IR	Fourier Transform Infrared
His	Histidine
ICP	Internal concentration polarization
LB	Langmuir-Blodgett
LPR	lipid protein ratio
LS	Langmuir-Schaefer
LUV	large unilamellar vesicles
MLV	multilamellar vesicles
NHS/EDC	N-hydroxysuccinimide/ 1-ethyl-3-(3-dimethylaminopropyl) carbodiimide
NF	Nanofiltration
NPA	asparagine-proline-alanine
PBS	phosphate buffered saline
PCTE	Polycarbonate track etched
PDA	Polydopamine
PDI	polydispersity indices
PEG	Polyethylene glycol
PMOXA-PDMS-PMOXA	Poly(2-methyloxazoline)-*b*-poly(dimethylsiloxane)-*b*-poly(2-methyloxazoline)
PEO-	poly(ethylene oxide)-*block* poly(dimethylsiloxane)-*block* poly(2-

PDMS-PMOXA	methyloxazoline)
RMS	root-mean-squared roughness
RO	reverse osmosis
rhodamine B-DHPE	rhodamine B 1,2-dihexadecanoyl-sn-glycero-3-phosphoethanolamine, triethylammonium salt
SUV	small unilamellar vesicles
TEM	transmission electron microscopy
VdW	Van der Waals
XPS	X-ray photoelectron spectroscopy

LIST OF TABLES

LIST OF FIGURES

CHAPTER 1: Introduction and background

Fresh water scarcity is a serious challenge that a large part of the world is facing today. This is mainly due to population growths, agricultural withdrawals, consumptions by power generation and industrial production. Membrane desalination through reverse osmosis (RO) is an option to augment the global water supply [1, 2]. RO has also been applied for developing fresh water resource from brackish water [3, 4] and ground water [5], as well as recycled wastewater [6]. RO process is accompanied with intensified consumption of energy due to the high osmotic pressure of the feed and the low water permeability of the membrane, which puts strains on the electricity production and result in adverse effect to environment. The permeability of RO membranes is very low (conventional RO membrane $<5\times10^{-7}m^3/m^2/s/bar$) [7], thus high pressure or large membrane area is required to ensure the water productivity (Figure 1-1 and Appendix A-1). Currently, energy consumption can reach about 45% of the total desalination cost. Hence, it has been a major challenge for the implementation of RO desalination as a new water supply option.

Innovations that reduce energy consumption will facilitate to reduce the cost of water production and provide sustainability to water supply. Especially, technological advances in RO membranes and system designs as well as global optimization have promoted the efficacy and affordability [8, 9]. A highly permeable membrane is a key. Figure 1-1 indicates that without any energy recovery devices and system optimization, the specific energy consumption (SEC) can be significantly reduced if the membrane permeability is

enhanced. A sufficiently high permeable membrane will enable the desalination to approach the limit of thermodynamic restriction. Consequently, a lower pressure can still provide equivalent or even higher productivity with smaller membrane area and thus lower water production cost.

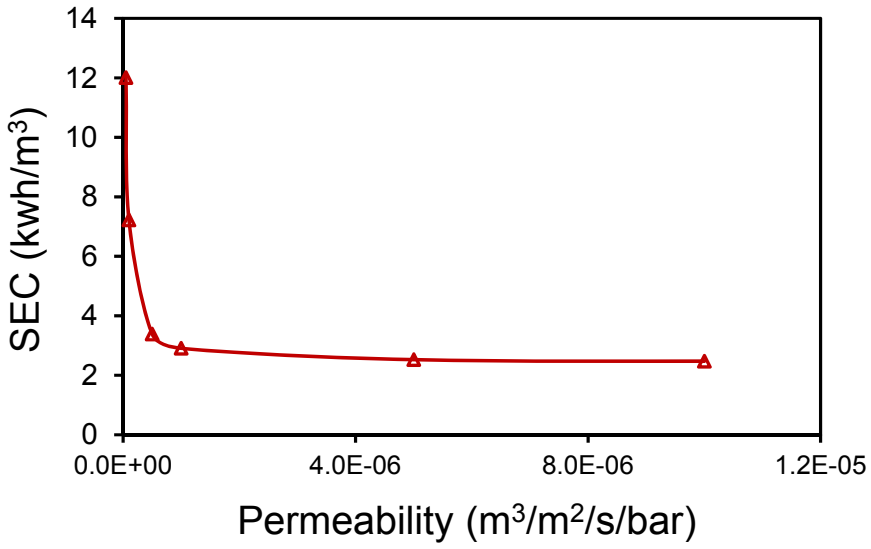

Figure 1-1 Variation of specific energy consumption (SEC) with the membrane permeability for a single stage RO.

Cell membrane possesses an array of transmembrane proteins that can facilitate the transport of water, K^+ and other molecules driven by the concentration gradient. Most importantly, cell membrane can permeate water at extremely high flow rate which is driven by osmotic pressure. Learning from nature, it may be argued that both highly permeable membrane and the forward osmosis (FO) could potentially reduce energy requirement of desalination process. In this study, I focused on developing a highly permeable membrane with near-perfect solute rejection and its application in an FO

process to demonstrate its potential in desalination process. It will provide guildence to further explore its application in the low pressure RO process.

1.1 Forward osmosis

1.1.1 Osmotic process

Osmosis, which is of pivotal importance in nature, is usually elucidated as a net water transport through a semi-permeable membrane driven by an osmostic pressure difference. As shown in Figure 1-2, osmosis can be classified into three categories, namely RO, pressure-retarded osmosis (PRO) and FO.

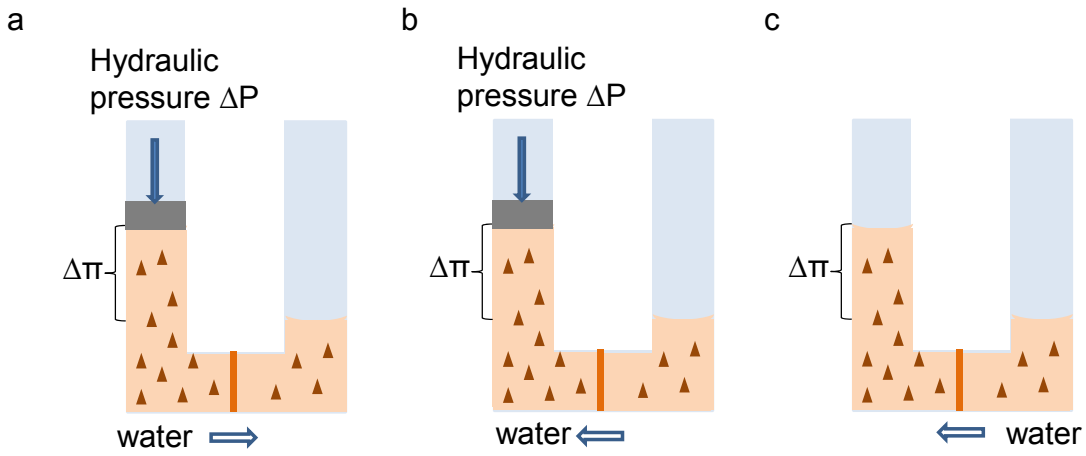

Figure 1-2 Schematic of three osmosis phenomena, (a) RO ($\Delta\pi < \Delta P$), (b) PRO ($\Delta\pi > \Delta P$) and (c) FO.

In nature, FO is the primary means by which water is transported through the cell membrane. For example, plants use naturally occurring osmotic pressure between the roots and the shoots to drive the uptake of water. A similar transport mechanism can be applied for water reuse if the semi-permeable membrane can provide high water permeability and near-perfect solute rejection. FO process utilizes a solution with a lower

water chemical potential than waste water or seawater to draw water through a semipermeable membrane. FO is an emerging technology that is capable for desalination and waste water reuse with lower energy consumption than traditional RO [10].

The transport of water and solutes through the polymeric FO membrane follows the solution-diffusion mechanism. There are several requirements for an FO membrane [11]. First, the intrinsic property of the selective layer should provide adequate high water permeation and low solute permeation. Second, an optimal support layer structure is required to eliminate internal concentration polarization. Third, the membrane must be chemically and mechanically robust. Finally, the membrane must be assembled in a way to provide sufficient membrane area per unit volume. Modern membranes are dominated by polymer membranes which include cellulose acetate [12], cellulose triacetate [13], polybenzimidazole [14], and thin film composite polyamide membranes [15]. Although many of them have shown improved efficiency in water permeability and salt rejection [12-15], there are several challenges that deter the successful implementation of FO for fresh water production. Among these, a crucial question is how to design semi-permeable membranes with enhanced water permeability.

Additionally, to obtain fresh water, a low-grade of energy will be needed to further separate draw solutes from draw solution [10]. Therefore, fabricating highly selective and permeable membranes will allow using a lower draw solute concentration to achieve a high water throughput with lower energy requirements. To do this, the membranes may

not follow the solution-diffusion mechanism that occurs in the dense polymeric membrane.

1.1.2 FO set-up and testing procedure

Figure 1-3 provides two different modes for laboratory-scale FO experiment. For the dynamic flow, two mesh spacers are added on each side of the membrane as a support. Co-current flow mode of draw and feed solutions is applied in a crossflow cell, driven by the peristaltic pumps. The water flux is estimated from the average weight increment of draw solution. For a dynamic test, the permeate flux is estimated by dividing the slope of the curve, as shown in Figure 1-4, with the membrane area. The salt reverse flux is estimated by measuring the conductivity of the feed solution at the end of the experiment.

a

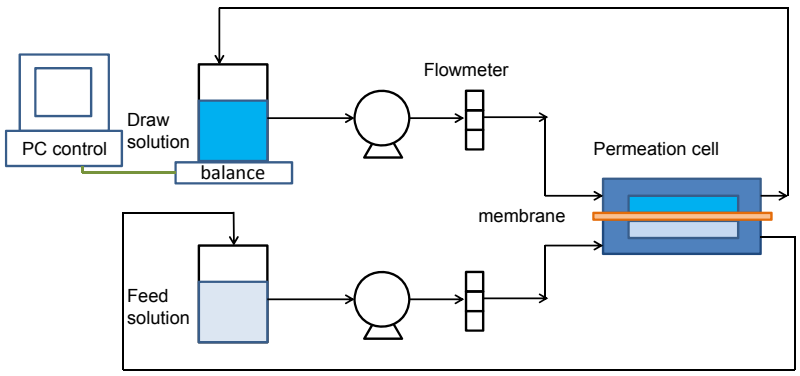

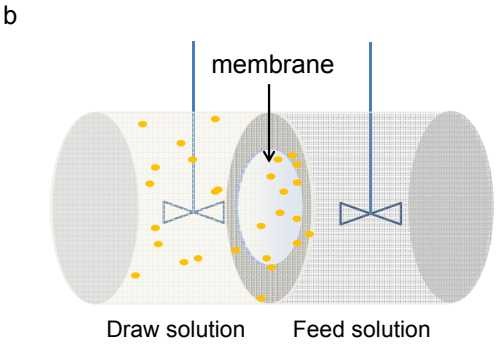

Figure 1-3 Laboratory-scale FO set-ups. (a) Dynamic FO process. (b) Static FO process.

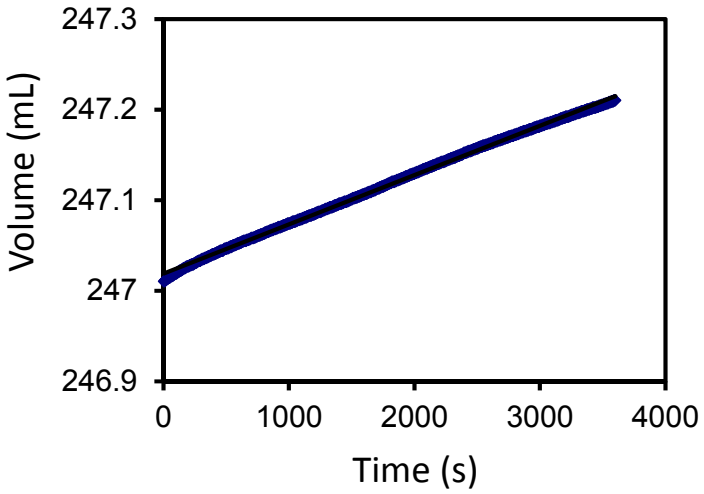

Figure 1-4 Example of permeate flux calculation (raw data).

1.1.3 Membrane transport mechanisms

Membranes for water purification can function mainly by two mechanisms: pore flow or solution-diffusion. Generally, pore flow follows a size-sieving principle, which usually happens in microfiltration or ultrafiltration. The pore-flow in membrane channel can be modeled as flow through a circular tube with a radius of R_t and a length of L_t, and can be described by Hagen-Poiseuille equation [16]:

$$m_c = \frac{\varepsilon \rho R_t^{\,2}}{8 \mu L_t} \Delta P_c \tag{1-1}$$

where m_c is the mass flux, ε is the porosity, ρ is the solution density, μ is the viscosity of solution and ΔP_c is the pressure difference between the entrance and the exit of the channel.

For the case of solution-diffusion, permeates molecularly dissolve in the polymer matrix, diffuse through the polymer dense layer and desorb at the downstream side. Thus, the water and solute fluxes are influenced by polymer properties, such as molecular structure (eg. degree of crosslinking) and polymer morphology. In a semi-permeable hydrophilic polymeric membrane, the polymer pores are not interconnected, so water molecules normally oscillate in the hydrated polymer chains. Self-diffusion of water can be accomplished only when the pores become interconnected, which results from thermal fluctuation. This phenomenon is called "jump" diffusion. On the other hand, the diffusion of solutes, such as NaCl, in the hydrated polymer is determined by the mobility of both Na^+ and Cl^- in order to satisfy electroneutrality. In a semi-permeable polymeric membrane, the diffusions of solutes are significantly lower than that of water molecules. The fluxes of water (J_w) and solutes (J_s) in the solution-diffusion model can be described by the following equations [17].

$$J_w = A\left(\Delta P - \Delta \pi\right) \tag{1-2}$$

$$J_s = B \Delta C_s \tag{1-3}$$

where ΔP is the transmembrane pressure difference, $\Delta \pi$ is the osmotic pressure difference between the feed and the permeate solutions. A and B are water and solute permeabilities,

respectively. ΔC_s is the solute concentration difference between the feed and the permeate solutions.

Equation (1-2) suggests that water flux is contributed by two factors: the water permeability of the membrane and the externally applied pressure. The water flux is achieved by the external pressure to overcome the osmotic pressure difference between the feed and the permeate solutions. For example, in sea water RO desalination process, the applied pressure must be greater than the osmotic pressure of sea water (29 bar) to obtain water productivity. For another example, we need to use a draw solution with higher osmotic pressure than sea water so as to gain water flux in a FO desalination process. Both examples suggest that high permeable membrane will render water purification to be more effective.

Facilitated diffusion is a passive transport, which is usually found in cells. Proteins, such as ion channels and water channels, act as pores or carriers, allowing that water and other solutes permeate following the concentration gradient. Aquaporins are passive water channels. Through the recent studies on Aquaporins in some model biomimetic membranes, it has been proposed that artificial membrane can be made specific to water and with much higher transport efficiency, as compared with conventional RO and FO polymeric membranes [18].

1.1.4 Concentration polarization in FO

The water flux in FO process is driven by the osmotic pressure difference $\Delta\pi$ across the membrane. As shown in Figure 1-5, in such process, the bulk osmotic pressure $(\Delta\pi_b)$ is usually much higher than the osmotic pressure across the selective layer $(\Delta\pi_{eff})$ and that across the membrane $(\Delta\pi_m)$, thus the obtained water flux is usually lower than expected. This phenomenon is called concentration polarization (CP), specifically external concentration polarization (ECP) and internal concentration polarization (ICP).

In FO process, as the permeating water flows from the feed solution to the draw solution, dilutive ECP will occur at the draw solution side (Figure 1-5a), meaning that it will dilute the draw solution near the membrane interface. Due to the permeating water flux, solutes can also build up at the interface of the selective layer facing the feed solution. This is called concentrative ECP (Figure 1-5b). Both dilutive and concentrative ECP have adverse effects to the FO process.

On the other hand, FO membrane is composed of a dense selective layer and a porous support. ICP refers to the concentration polarization occurs in the porous support layer. For example, if the porous support layer faces the draw solution (also referred as FO mode), the permeating water will dilute the draw solute across the porous layer. This phenomenon is referred as dilutive ICP, which usually happens in a real FO process, such as wastewater treatment (Figure 1-5b). Similarly, if the porous support faces the feed solution (also referred as PRO mode), it will lead to concentrative ICP. Since ICP

happens at the porous support, which is a dead zone, ICP cannot be eliminated by cross-flow (Figure 1-5a).

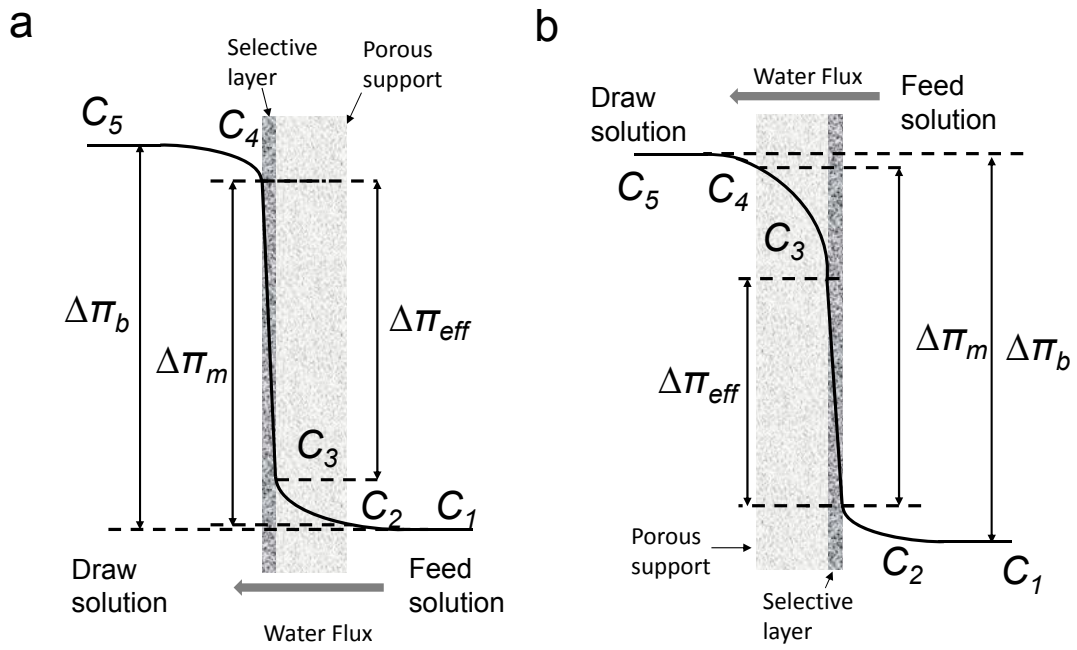

Figure 1-5 Concentration polarization across an asymmetric membrane in FO process.

1.2 Aquaporins

Biological membranes are perfect separation barriers in cells. This is mainly due to the fact that membrane channel proteins allow high permeability for specific components while maintaining tight control over selectivity. Cells, such as renal tubules, red cells or secretory glands, use an array of sophisticated pores formed by the passive channels called Aquaporins to achieve high water permeability and high selectivity, a feature not seen in any industrial polymeric membrane. In 1992, Agre and coworkers demonstrated the activity of Aquaporin1 (Aqp1) water channel proteins by using *Xenopus* ooctyes [19]. It has been found that the oocytes with channel-like integral protein of 28 kDa (CHIP28)

swelled and exploded rapidly in hypotonic solution as compared with the ones without CHIP28. Since then, another 10 Aqps (Aqp 0 to Aqp 10) with critical physiological functions have been discovered in human/mammalian bodies. Also, Aqps have been discovered in plants [20], bacteria [21] and archaea [22] . Driven by osmotic gradient, different solutes can diffuse through the neutral pore of Aqps. Some Aqps are featured of water transport (for example, Aqp 2 and Aqp Z). However, some Aqps, referred to as aquaglyceroporins, can transport neutral solutes, for example glycerol and urea [23, 24]. Aqp 6, which is from the family of mammalian Aqps, can transport anions (for example, nitrate) but only slightly permeable to water [25]. Mammalinan Aqp 8 has been shown to transport ammonia and hydrogen peroxide but exclude ammonium ions and protons [26, 27]. There are some other Aqps have shown to transport arsenite [28], antimonite [28, 29], CO_2 [30, 31] and NO[32]. The physiological roles of these unique transport capabilities of Aquaporins are still under investigation [33].

All Aqps exist in a tetrameric conformation and each monomer is a functional unit (Figure 1-6). Water transport Aqps have unique structure which allows them to solely transport water and reject all other solutes [34, 35]. Aqps have 6 intracellular domains which are collected by 5 extracellular loops (Figure 1-7), which means that they traverse a cell membrane 6 times. Aqps have intracellular cytoplasmic carboxyl and amino termini (Figure 1-7). Two small hydrophobic loops, each of which contains a conserved asparagine-proline-alanine (NPA) motif, dip halfway into the membrane to form the aqueous pore. It has been found that Aqps have two featured filters. NPA is one of the filters at the central part. The other filter is called aromatic/arginine (ar/R) region, which

is located on the extracellular side of the channel (Figure 1-7). The water molecules have to squeeze through the narrow NPA and ar/R regions and water-water hydrogen bonds will be ruptured. In this process, the energetic cost of water-water bond rupture will be largely compensated through the replacement interaction of Aqps. The activation barrier for water transport in Aqp is decreased to a large extent and thus allows fast water permeation [36]. The water permeation is referred as single-file permeation [34]. AqpZ obtained from reconstitution experiment has a water permeability above 10×10^{-14} cm^3/s, while AqpZ rejects glucose, sorbitol, sucrose, mannitol, glycerol and urea [37]. AqpZ has shown a stable permeability at a pH range of 5-7.

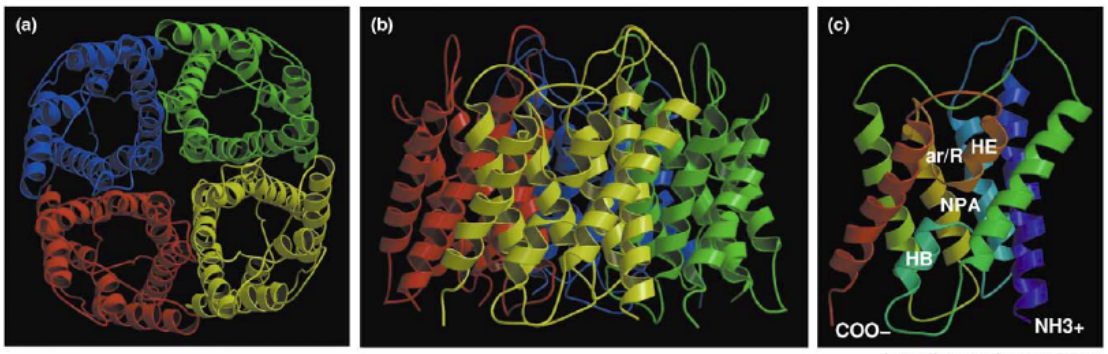

Figure 1-6 The structure of Aqp1. (a) and (b) are top view and side view respectively. (c) displays the NPA region and the ar/R constriction region. Loops B and E which contain the NPA sequences are folded back into the channel [34]. (Reprinted from Curr Opin Struct Biol., Vol 15, BL de Groot, H Grubmüller, The dynamics and energetics of water permeation and proton exclusion in aquaporins, Pages 176-183, Copyright (2005), with permission from Elsevier.

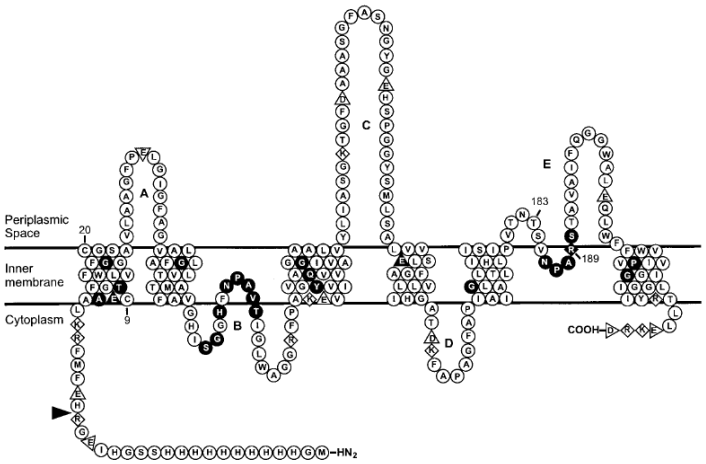

Figure 1-7 Membrane topology and predicted primary sequence of 10-histidine AqpZ [37]. Reprinted from J. Mol. Biol., Volume 291, M J Borgnia, D Kozono, G Calamita, P C Maloney, P Agre, Functional reconstitution and characterization of AqpZ, the E. coli water channel protein, Pages 1169–1179, Copyright (1999), with permission from Elsevier.

1.3 Amphiphilic materials

Amphiphilic lipid, which consist of a hydrophilic headgroup and one or two hydrophobic tails, are the major architectural component in cell membrane. Lipids can assemble into a variety of supramolecular structures when hydrated, due to the fact that the hydrophobic tails tend to aggregate to minimize the energetically unfavorable interaction with water [38]. The most widely studied form is the lipid bilayer configuration (i.e. lamellar form). Lipid bilayer functions as a barrier between the cell and its surroundings. It also provides an amphiphilic environment to accommodate transmembrane proteins and regulate the transport of ions and small molecules. Therefore, a wide variety of artificial lipid membranes, such as large unilamellar vesicles (LUV) [39-41], supported lipid membrane [42, 43] and tethered lipid bilayer membranes [44-46], have been developed to mimic the

structure of cell membrane. Nevertheless, natural lipids are very easy to be oxidized and their mechanical stability is too weak to pursue further industrial application.

Alternatively, amphiphilic block copolymers not only mimic the structure of lipids but also provide more chemical and mechanical stabilities compared to lipids. Additionally, the chemical synthesis of amphiphilic block copolymers affords freedom of tailoring the length of each block and ease of introducing specific functional end group. Amphiphilic block copolymers have hydrophilic and hydrophobic blocks that are covalently bonded together. In water, the hydrophilic block interacts favorably with water and the hydrophobic blocks are shielded, which results in a phase separation [47]. The block copolymers can assembly to several structures, such as micelles, rods and vesicles [48]. The relative size of the hydrophilic part to the hydrophobic part impacts the interface curvature, so as to determine the assembled structure [49]. As the increase of hydrophobic to hydrophilic ratio, the structure varies from spherical micelle to cylindrical micelle and to vesicles. To explain this phenomenon from a thermodynamic point of view, it is mainly related to the interfacial energy of the hydrophilic-hydrophobic interface and the entropy loss when the flexible polymer chains are assembled into a microstructure [50].

Some amphiphilic block copolymers are promising to have applications in encapsulation and release of active compounds as well as formation of block copolymer-protein hybrid systems [18, 51]. For example, polymersomes in drug delivery can target specific cell, which may result in fewer side effects and higher drug efficacy [52, 53]. Polymersomes

that are applied in biosensing can provide advantages, such as high loading capacity and high sensitivity [51]. Especially, it has been great potential as an amphiphilic matrix for transmembrane proteins. Generally, the thickness of lipid bilayers are about 4-5 nm [54]. Because they are vertically incompressible, their dimension has to match well with the hydrophobic parts of the transmembrane proteins in order to accommodate a transmembrane protein. If there is a perturbation in membrane thickness, it will prohibit protein insertion due to such a small dimensional mismatch. Similarly, it seems that a block copolymer film with a thickness of around 10 nm is likely to result in a dimensional mismatch and might denature transmembrane protein. However, this is not totally true. It has been shown recently that transmembrane proteins, such as LamB, OmpF, FhuA, Complex I and so on, could be inserted into the artificial membranes that are composed of amphiphilic block copolymers [55]. According to the result of the mean field analysis, the hydrophobic chains in the core of vesicle membrane are in an unfavorable stretched state. After protein incorporation, the hydrophobic part will be compressed, leading to an increase in the local surface tension energy but a reduction of the stretching energy [56]. Hence, in total, the protein incorporation may cause a very minor energy penalty in amphiphilic block copolymer membranes [56]. Additionally, it is envisioned that the block copolymer with shorter hydrophobic parts will distribute around the transmembrane proteins. Thus, a relatively broad polydispersity of the synthetic block copolymer may facilitate protein incorporation.

Several amphiphilic block copolymers may potentially apply for to the block copolymer protein hybrid systems. These block copolymers include poly(ethylene oxide)-*block*

poly(dimethylsiloxane)-*block* poly(2-methyloxazoline) (PEO-PDMS-PMOXA) and poly(2-methyloxazoline)-*block*–poly(dimethylsiloxane)-*block*–poly(2-methyloxazoline) (PMOXA-PDMS-PMOXA). Amphiphilic block copolymer PMOXA-PDMS-PMOXA has been found to have a highly flexible hydrophobic block that allows the artificial polymer membrane to fulfill the geometric and dynamic requirements of some channel proteins, such as AqpZ and OmpF [18, 57]. Researchers have found that the highly flexible PDMS middle block and the polymer dispersity could help to stabilize the block copolymer-protein hybrid systems [58]. It has also been found that the asymmetric triblock copolymers PEO-PDMS-PMOXA can orient the channel directions of the incorporated Aqp0 [49].

1.4 Biomimetic membrane design and preparation methods

Biomimetic membrane is a membrane design that can break down the complexity of cell membrane and enables us to investigate the membrane-related process. As shown in Figure 1-8, early concepts of biomimetic membrane are black lipid membranes, vesicles and solid-supported lipid/block copolymer membranes.

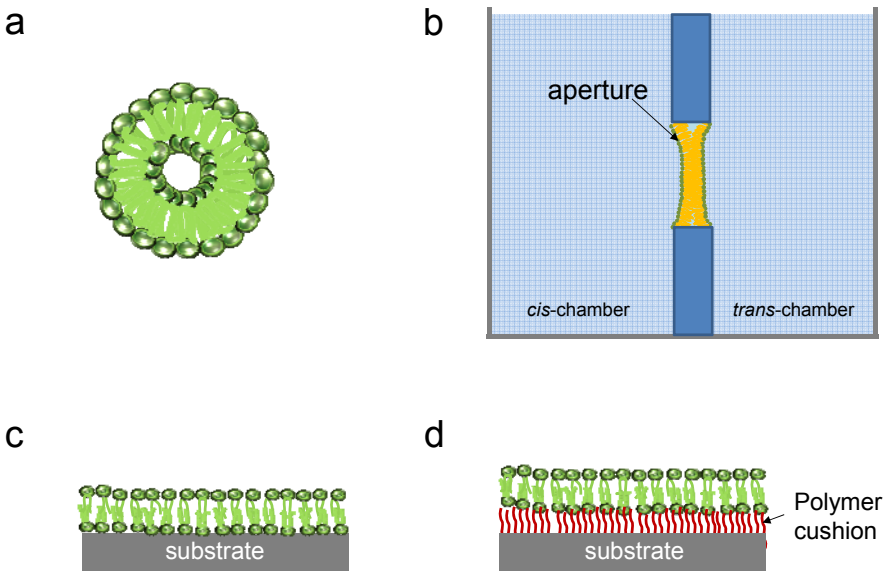

Figure 1-8 Schematic of biomimetic membranes (a) vesicle, (b) black lipid membrane, (c) solid-supported lipid membrane and (d) solid-supported lipid membrane with a polymer cushion.

Vesicles, composed from lipid bilayers or block copolymers, are colloidal assemblies and can encapsulate aqueous solution in the region that is enclosed by the hydrophilic parts of the amphiphilic materials. Based on the number of the layers and the size of the vesicles, they are classified as the multilamellar vesicles (MLV), the large unilamellar vesicles (LUV) and the small unilamellar vesicles (SUV). The LUVs shown in Figure 1-8a have a wide application in the fields of chemistry, physics and biology. LUVs can be used for drug and cosmetically active ingredients delivery [59, 60] as well as reconstitution of transmembrane proteins [61-63] and peptides [64] .

Vesicles are usually prepared via either solvent-free technique [65] or solvent-aided technique. In the solvent-free technique, the organic solvent will be removed from the amphiphile-solvent mixture, resulting in a dry film of amphiphile. Then, the amphiphilie

film is brought into contact with aqueous buffer to yield vesicles[66]. In this process, water will diffuse through the defects into the film layers. Then the films will swell and generate vesicles driven by the hydration forces [67]. For the second method, the amphiphile solvent mixture is dispersed in aqueous buffer through vigorous stirring and mixing [68]. The organic solvent is partially removed through evaporation, but a trace of solvent still remains in the hydrophobic part of the amphiphile. LUVs with narrow polydispersity can be further produced through repeated extrusions. Nevertheless, the first method is preferred for transmembrane protein incorporation, because the trace of organic solvent may impact protein's function and long term stability.

Black lipid membrane is the earliest model of lipid bilayer. It appears dark in the reflected light, because its thickness is only in nanometer range. The main advantage of this membrane is that the lipid/block copolymer layer separates two aqueous compartments, so it can mimic the environment of cell membrane without denaturing transmembrane protein channels. It is usually formed via dispersing lipids or block copolymers in a non-solvent, for example n-decane, across an aperture (200 μm diameter) of a hydrophobic partition (Figure 1-8b). Before the bilayer is formed over the aperture, a small amount of lipid dispersion is dropped around the hole and is allowed to dry. Then the aperture holder is placed between the *trans* and the *cis* chambers which are filled with buffer solutions. Additional lipid dispersion may be drawn across the aperture using a stick or a brush. Then, a film will form spontaneously. In the beginning, the film will be about several micrometer-thick and then reduce to several nanometers to form a bilayer [69].

Solid-supported phospholipid membranes, shown in Figures 1-8 c and d, can be prepared via (1) Langmuir-Blodgett (LB) and Langmuir-Schaefer (LS) monolayer transfer techniques as well as (2) vesicle rupture.

The LB technique allows orienting the lipids or block copolymers at an air/water interface. The Langmuir monolayer is usually formed from three steps: (a) amphiphilic materials are spread at the air/water interface; (b) amphiphilic materials are compressed by two mobile barriers and the surface pressure will increase; (c) all the amphiphilic molecules are aligned at the interface and a condensed monolayer is formed [70] (Figure 1-9). Such Langmuir monolayer can then be transferred via LB or LS technique to a solid support based on the interfacial interaction between the solid support and the monolayer (Figure 1-10). To mimic the structure of the lipid bilayer, a hydrophilic surface is used for deposition of the first monolayer and becomes hydrophobic. Subsequently, the second monolayer can be transferred.

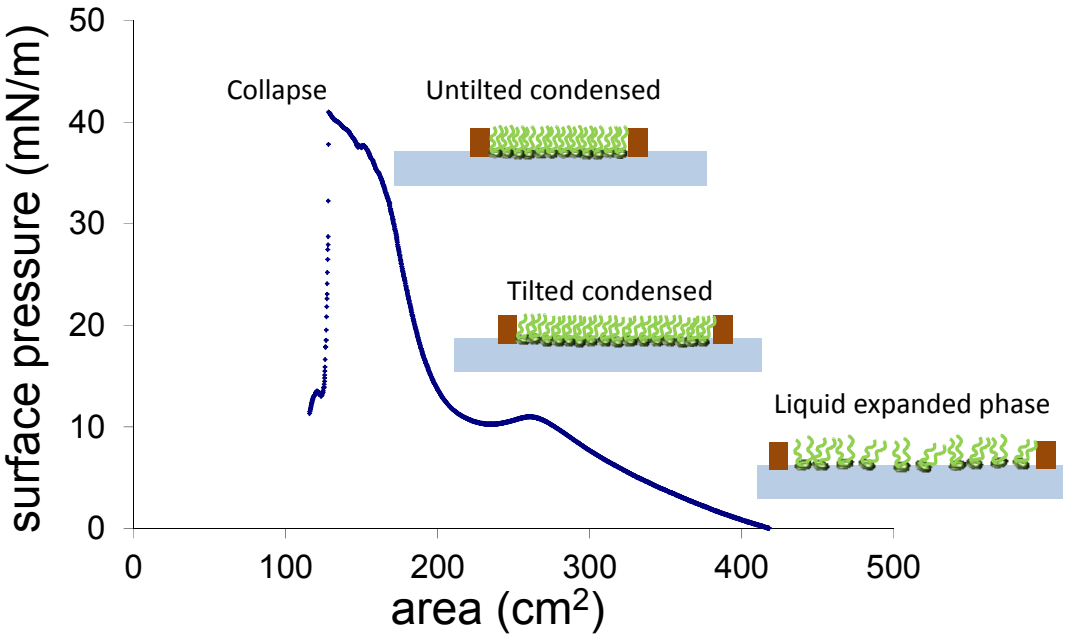

Figure 1-9 Surface pressure-area compression isotherm of a lipid monolayer. As the barrier continues to compress, the lipid monolayer will experience four different states.

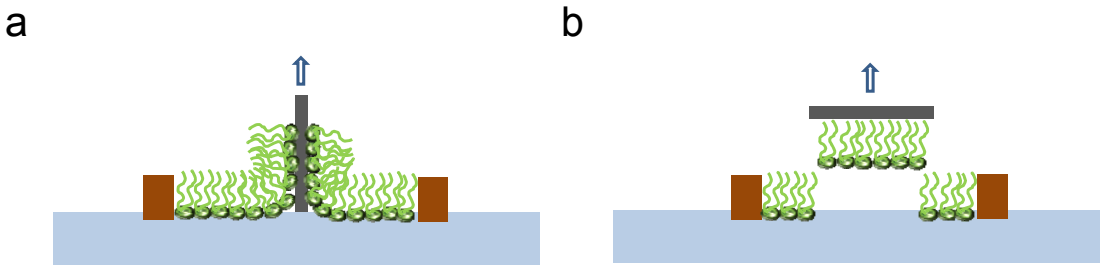

Figure 1-10 Langmuir monolayer transfer methods (a) Langmuir-Blodgett (LB) monolayer transfer on a hydrophilic substrate; and (b) Langmuir-Schaefer (LS) monolayer transfer on a hydrophobic substrate. The arrows indicate the deposition directions.

Supported lipid/block copolymer layer can also be formed by a spontaneous deposition of vesicles on a solid support. A general principle is that a sufficiently large deformation of vesicle will induce vesicle rupture and transform onto a flat bilayer disk. The bilayer disk

may induce other adsorbed vesicle to rupture and to form bigger patches [71] (Figure 1-11). These rupture events are governed by the interaction between the membrane and the support as well as intramembrane interactions. Specifically, these interactions depend on the nature of the vesicle (charge property, chemical composition and size), the surface characteristics of the solid support (surface chemical property and roughness) and the aqueous environment (ionic strength and pH). It is worth to mention that the block copolymers are more mechanically stable than lipids [72], thus it requires a stronger interfacial interaction for a polymer vesicle rupture to occur, such as electrostatic interaction and covalent bonding [73, 74].

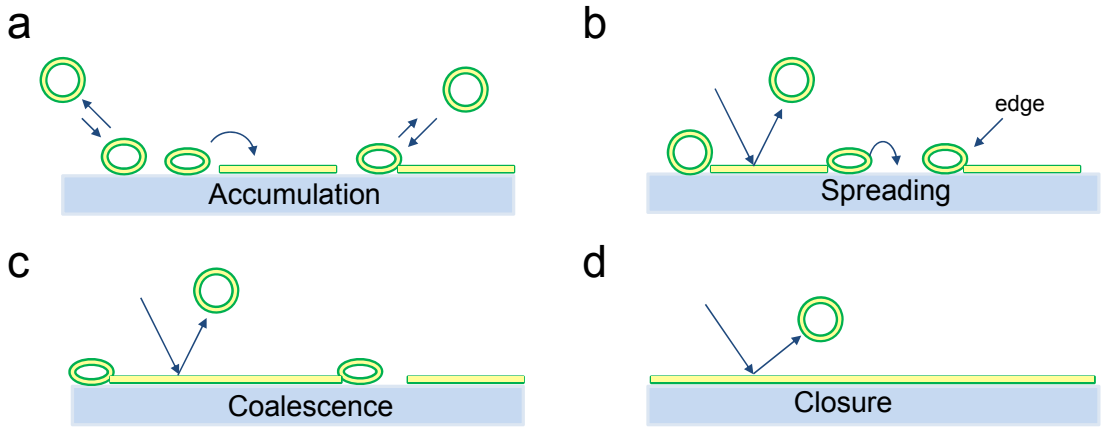

Figure 1-11 Schematic diagram of vesicle rupture process: (a) vesicles accumulate on the solid support; (b) vesicles rupture and the resulted edge promotes other vesicles to rupture; (c) bigger patch of lipid film is formed through film fusion; and (d) a homogeneous lipid bilayer is formed.

1.5 Transmembrane protein incorporation

Transmembrane protein incorporation is a useful tool to study the function and structure of the membrane associated proteins. Four different techniques have been used to achieve

protein incorporation, for example organic solvent-mediated incorporation, mechanical means, directly incorporation into preformed vesicles and detergent-mediated reconstitution [61]. The most successful and frequently used method is the detergent-mediated method. A proposed mechanism for a protein reconstitution process is shown in Figure 1-12. When the liposomes are mixed with the protein-detergent micelles, a ternary mixture will be formed. Some lipids can still exist in the detergent-saturated liposomes. Protein molecules which initially present in the detergent micelles will be slowly transferred into the detergent-saturated liposomes. The detergents are slowly removed through dialysis or biobeads methods, resulting in the homogeneous proteoliposomes. Some factors that have influences on the process of protein reconstitutions are detergent concentration, the rate of detergent removal and lipid-to-protein ratio. Generally speaking, transmembrane protiens are vectorial molecules, suggesting that they have a distinct direction in cell membranes. However, after isolated from the natural cell membranes, the proteins are incorporated into an artificial membrane system without a preferred direction. It may be a disadvantage for some applications, such as biosensor, but it may not impact the function of Aqps due to their bi-directional characteristics [75].

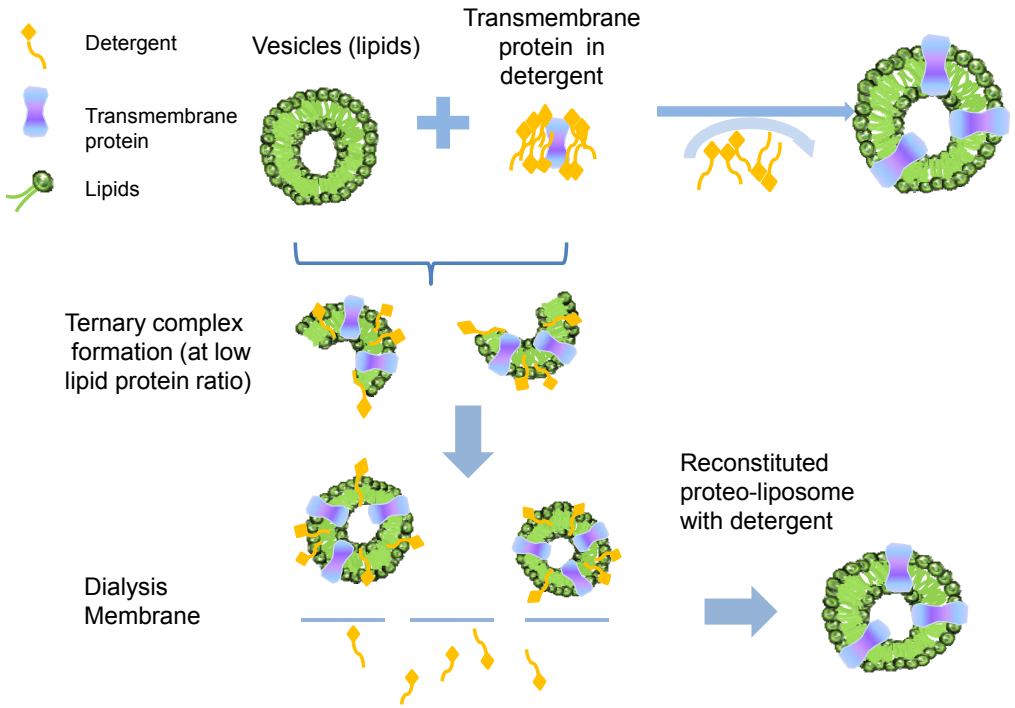

Figure 1-12 A proposed mechanism for an ideal protein reconstitution process.

1.6 Biomimetic membrane designs for separation

Due to the low mechanical stability of biomimetic membranes, a porous support must be involved in the designs for separation. Figure 1-13 shows a design that is derived from solid-supported biomimetic membrane. In this design, a biomimetic lipid membrane has been coated on the surface of a commercial nanofiltration membrane and the lipid bilayer renders to be robust enough to withstand high pressures [76].

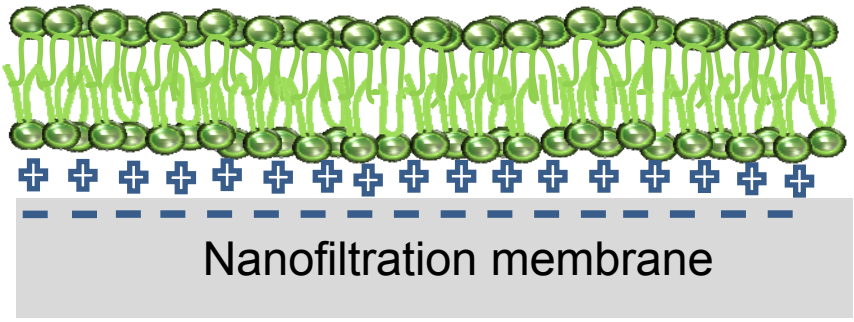

Figure 1-13 Design of biomimetic lipid membrane based on electrostatic charge interaction for RO application.

Recent developments in membrane encapsulation and substrate provide opportunity to scale up the black-lipid-membrane and the black-polymer-membrane. As shown in Figure 1-14, the biomimetic membrane is formed across a porous hydrophobic partition. Some attempts at fabricating biomimetic membranes based on this design have been reported in literatures [77]. Highly crosslinked hydrogel has been applied for in situ encapsulation of black lipid/block copolymer membranes which are formed across one or multiple apertures in a hydrophobic partition, leading to higher mechanical stability [77, 78]. The pore size of the partition ranges from 100 μm to 1 mm. Such design improves stability of the biomimetic devices; however challenges still remain. For example, the long term stability of the membrane is questionable. For a multiple apertures system, it is difficult to ensure all the apertures are fully covered. Another drawback is that the density of channel proteins is not well controlled [78].

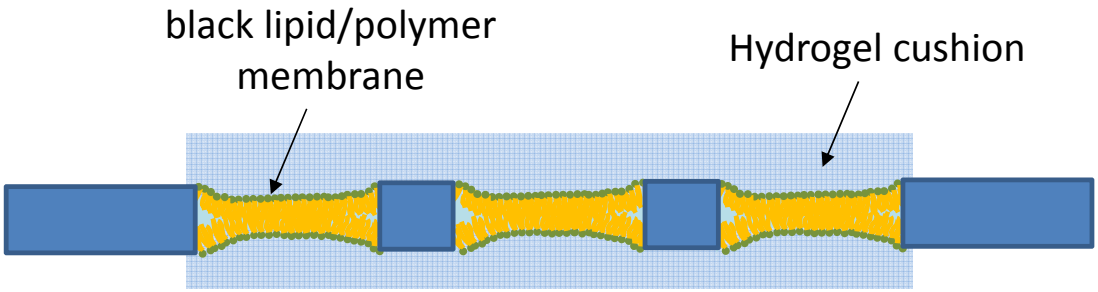

Figure 1-14 Design of hydrogel-encapsulated pore-spanning membrane [79]. Channel proteins are embedded in an amphiphilic matrix on a porous partition and cushion materials are used to support the membrane.

1.7 Characterization of biomimetic membrane

1.7.1 Characterizations of biomimetic membrane

1.7.1.1 Stopped flow technique

Stopped-flow technique has been applied to measure the water permeability of liposomes and erythrocytes [80, 81]. The instrument is shown in Figure 1-15. The syringes are filled with two solutions with different osmolality. The syringe piston will push the two syringes injecting simultaneously and the solutions will be mixed in a mixer. Within several milliseconds, the solution will flow through a cuvet and then into the stop syringe, and finally be stopped by the stop syringe. The light scattering is monitored at the cuvet after the flow is stopped.

The permeability of reconstituted Aqp in vesicles is characterized mainly by the stopped-flow spectroscopy technique. In a stopped-flow experiment, the osmotic permeability P_f ($m^3/m^2/s$) can be calculated by using the equation [37]:

$$P_f = \frac{k}{(S_0 / V_0) V_w \Delta_{osm}} \tag{1-4}$$

where k is the rate constant obtained from light scattering signal, S_0 (m^2) and V_0 (m^3) are the initial surface area and volume of the vesicle, respectively. V_w is the molar volume of water (18×10^{-6} m^3/mol) and Δ_{osm} is the osmolarity difference that drives the vesicle shrinkage.

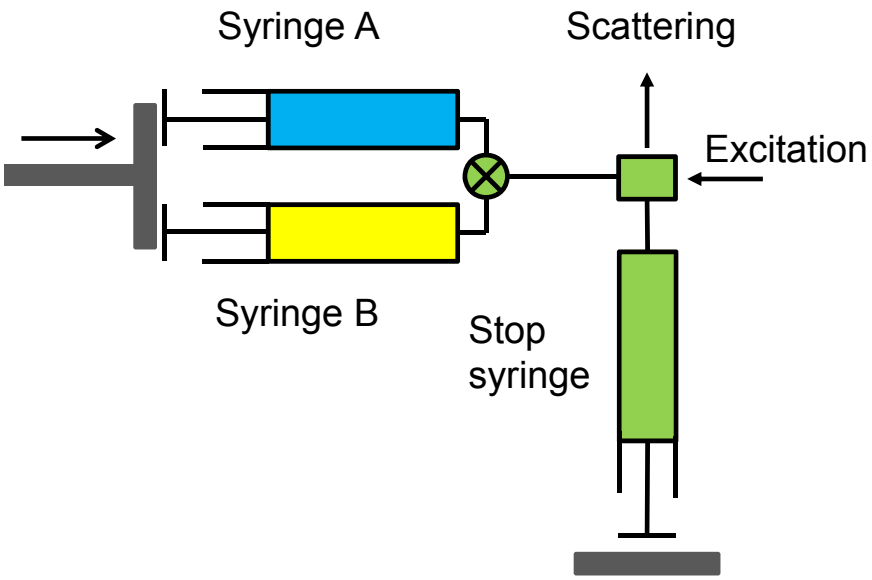

Figure 1-15 Schematic diagram of the stopped-flow device.

1.7.1.2 Atomic force spectroscopy (AFM) principle and force curves

AFM provides a 3-dimensional feature of a surface by measuring forces between the tips and the surface at a very short distance. As shown in Figure 1-16a, the movement of the tip across the surface is monitored by using a piezoelectronic scanner through a feedback loop. The laser that is reflected from the back of a cantilever will be recorded by a position sensitive photodiode detector. In this process, the bending of the cantilever will be measured and a map of the surface topography of a sample will be generated.

van der Waals (VdW) interaction is the dominant force at a short distance. During contact with the sample surface, the tip will experience a VdW repulsion force, which leads to the tip deflection. Force curve records the amount of force felt by the tip when the tip approaches or retracts from a sample surface. Force curve analyses can be applied to determine the adhesion force and the affinity between the molecules as well as the

rupture bond length. For example, a tip with functional groups on the surface can measure the interactions between the functional groups and a surface. Nevertheless, the AFM tip applies a force at a local scale. Thus, such measurement may not represent the bulk property of a material.

The mechanical behavior of the lipid bilayers that is spanned over on a porous support can be observed by using the AFM local indentation experiments. As shown in Figure 1-16b, it can be conceived that the membrane will experience several steps of deformation before rupture occurs [82]. At the beginning, the membrane deforms because of the vertical indentation of the tip. Then, due to the deformation, the membrane generates some small holes. When the diameter of a hole reaches a critical radius, the rupture occurs, coupling with a disintegration of the whole membrane. Subsequently, the AFM cantilever relaxes and the tip penetrates several hundred nanometers below until it hits the wall of the pore.

The nanomechanics and the membrane thickness of a lipid bilayer can also be measured by using AFM indentation. Usually in these measurements, a hydrophilic tip, such as silicon nitride tips, is needed. As shown in Figure 1-16c (1), when the tip is pushed onto the lipid bilayer, cantilever deflection occurs as the tip is physically in contact with the bilayer (point 1). Then, the membrane deforms elastically, as shown in Figure 1-16c (2), until the membrane reaches its limit to withstand the force. At this point, a jump is shown on the force curve, which is a signature of the event that the membrane has been punched

through, as shown in Figure 1-16c (3). At a higher pushing force, the cantilever will contact the solid substrate, resulting in further cantilever deflection [83].

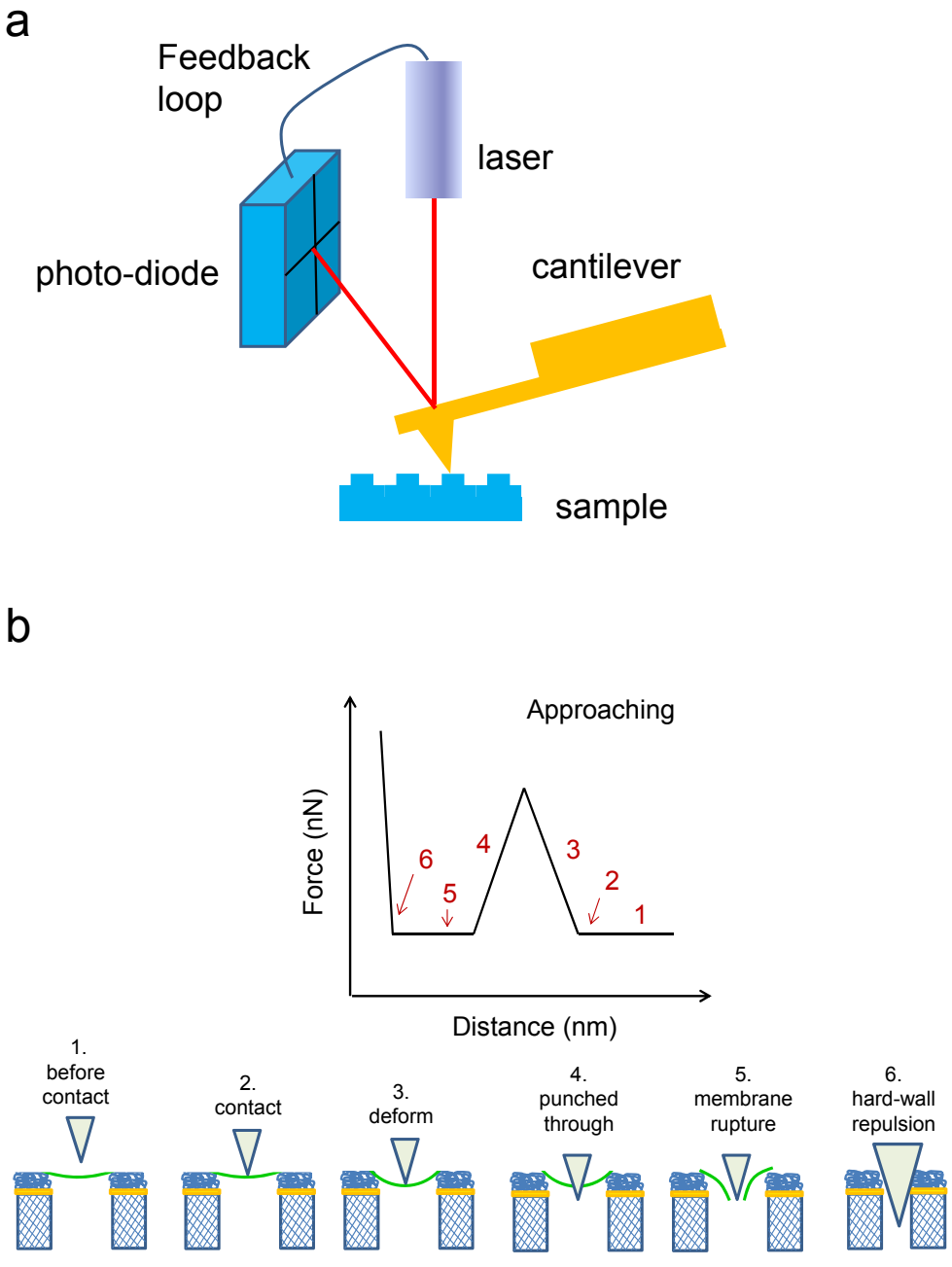

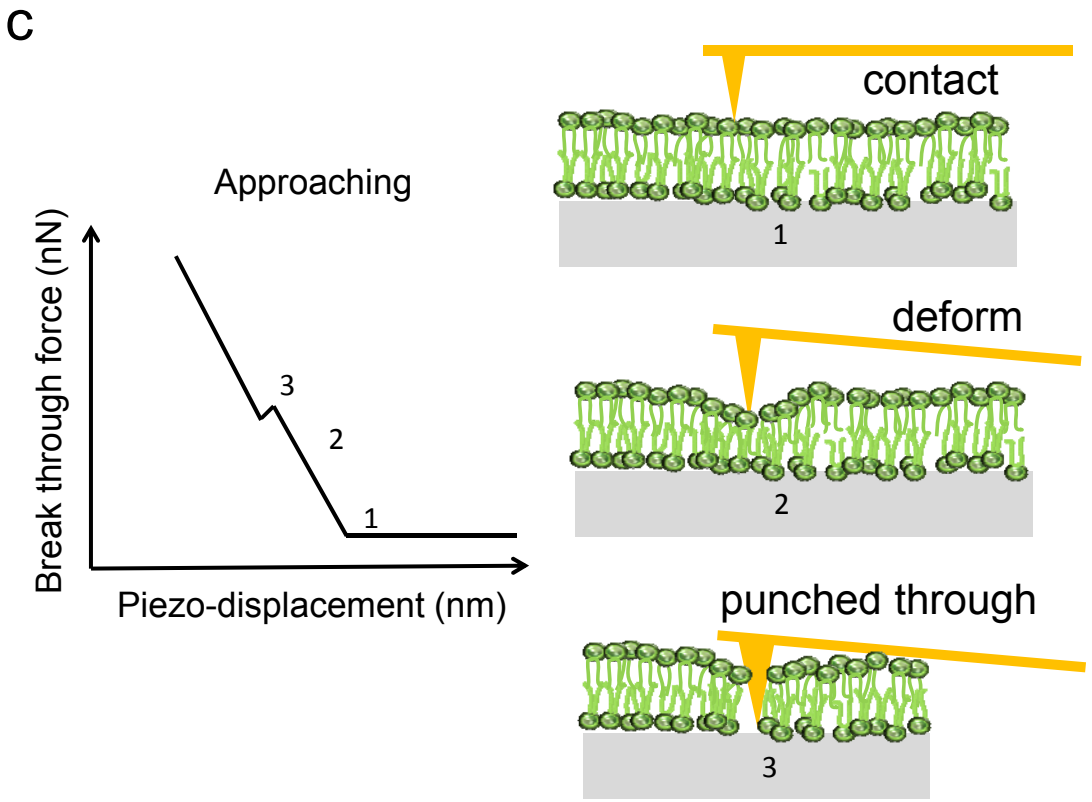

Figure 1-16 Schematic diagrams of mechanical stability measurements using an AFM tip. (a) Experimental set-up of AFM instrument. The detection is realized by using a laser and position sensitive photodiode detector. (b) Illustration of the pathway of a rupture event of pore-spanning membrane upon AFM indentation. (c) Illustration of a conceived indentation pathway of solid supported lipid bilayer by the AFM tip.

1.7.2 Characterizations of water transport through the Aquaporin-incorporated membranes

The hydraulic permeability coefficient L_p (m/s/bar) represents the rate of water movement across a given area, per unit of osmotic gradient and can be calculated from the equation [84]:

$$L_p = \frac{P_f V_w}{RT} \tag{1-5}$$

where R and T are gas constant and temperature, respectively. When the biomimetic membrane transforms from a sphere to a flat surface, the intrinsic water volume flux J_v (m^3/s) can be obtained by using equation [84]:

$$J_{vs} = AL_p\left(\sigma\lambda RT\Delta C - \Delta P\right) \quad (1\text{-}6)$$

where A is the membrane area, in m^2. σ is the reflection coefficient and is assumed to be 1. λ is the molecularity. ΔP is the hydrostatic pressure difference across the membrane, in bar. ΔC is concentration difference across the membrane, in mol/m^3.

1.8 Objectives

The main hypothesis of this work is that an Aquaporin-embedded membrane can be fabricated for water reuse application through optimizing the biomimetic membrane design and the synthesis route.

This dissertation is structured into five chapters and two appendices. Chapter one provides an introduction of the research background and a short discussion on the potential of Aqps incorporated biomimetic membrane.

In the second Chapter, we will mainly use an AFM technique to study two interfacial interactions, namely (a) the interfacial interaction between the lipid and Aqp Z and (b) the interface interaction between the biomimetic membrane and the membrane support. We aim to investigate the factors that could influence the mechanical stability of the selective layer and explore the reason of low coverage of biomimetic membrane on the porous support.

In the third Chapter, we will fabricate the supported pore-spanning biomimetic membrane and tune the factors that could impact the coverage of the biomimetic membrane on the support. We will also demonstrate the water permeation and salt rejection of the membrane in an FO process.

In the fourth Chapter, a novel vesicular biomimetic membrane design is adopted and implemented. The main objective is to improve the mechanical stability of the biomimetic membrane. We will show the preparation methods and permeability characteristics of the membrane formation process.

In the fifth Chapter, a transport model of vesicular biomimetic membrane will be built. The key factors that could impact the water permeability of the membrane will be explored and discussed based on a mathematic modeling.

In the sixth Chapter, general conclusions are summarized and some recommendations as well as ideas for future research are proposed.

Appendix covers the detailed calculations that are involved from Chapter one to Chapter five.

CHAPTER 2: Preparation and characterization of pore-spanning biomimetic membranes embedded with Aquaporin Z on carboxylated polyethylene glycol polymer cushion

2.1 Introduction

A commonly employed way to prepare planar pore-spanning membranes is through vesicle fusion and spreading [85]. Even though Aqps can be incorporated into both lipids and amphiphilic block copolymers, the soft polymer chains of the block copolymer substrate may hinder the vesicle fusion and hence impede the formation of a planar membrane. Thus, it will need a well-controlled technique to form a block copolymer film on a solid support. Lipids may possess a higher propensity to cause vesicle fusion due to a more rigid structure. 1,2-dimyristoyl-sn-glycero-3-phosphocholine (DMPC) was selected because the reconstitution of aquaporin can benefit from the relatively low phase transition temperature (23 °C) of DMPC. The mechanical stability of the supported DMPC bilayer was found to be much higher than the unsaturated lipids by atomic force microscopy (AFM) indentation [86], although the unsaturated lipids which undergo phase transitions at temperatures below 0 °C also allow aquaporin reconstituted at an appropriate temperature (i.e. lower than 37 °C).

It has been known that the performance of a biomimetic membrane is highly dependent on the integrity of the selective layer and the density of the water channel inside the

membrane. So far, no aquaporin embedded planar biomimetic membranes have been demonstrated for water reuse. The key hurdles in the fabrication of planar biomimetic membranes are (a) lack of compatibility data between Aqps and lipids (for example, DMPC); (b) defect formation owing to the fragile planar lipid bilayer coupled with substrate roughness; (c) insufficient knowledge about local mechanical stability of the pore-spanning planar lipid membrane with reconstituted transmembrane proteins. To address these questions, experiments were firstly conducted to optimize the AqpZ-DMPC ratio through permeability analyses using a stop-flow apparatus. Further investigation was carried out to examine the local mechanical stability of pore-spanning membranes on each of the two designs based on different interfacial interactions between the membranes and the substrates (Figure 2-1). Sequentially, the effects of aquaporin content on local mechanical properties of these biomimetic membranes were studied by means of force indentation experiments in the center of the unsupported membrane using AFM. It is envisioned these studies would lay the foundation for the molecular design of AqpZ-embedded biomimetic membranes for useful applications.

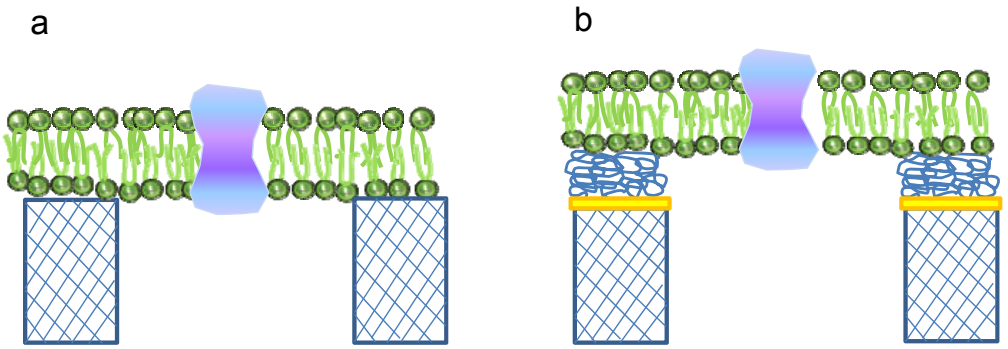

Figure 2-1 Schematic representation of two biomimetic membranes on porous substrates: (a) biomimetic membrane formed directly on a porous alumina in design A; (b) in design B, biomimetic membrane formed on a carboxylated PEG cushion chemisorbed on a 60 nm gold layer that was deposited on a porous alumina.

2.2 Experimental Methods

2.2.1 Preparation of liposome and aquaporin reconstitution

Vesicle suspension was prepared using the film rehydration method. DMPC (Avanti polar lipids, USA) was dissolved in an appropriate amount of chloroform, and then dried on the walls of a round bottom flask using a rotary evaporator. The film was further dried under vacuum overnight to fully remove the chloroform residue and afterward rehydrated by adding 1×phosphate buffered saline (PBS) buffer at 25ºC for 12 hours. The lipid suspension was vortexed twice. The unilamellar vesicles were obtained by extruding the vesicle solution (1 mg/mL) for 21 times using a polycarbonate membrane of 400 nm and 100 nm pore sizes, sequentially. For reconstitution experiments, 20 μl of AqpZ solution (1 mg/mL in 9 mM dodecyl-β-d-maltoside, DDM) was added during forming the lipid vesicles and the mixture was left stirring for more than 8 hours. Then, a total amount of 0.5 g biobeads was added stepwise into the mixture to remove the detergent so as to incorporate the AqpZ into DMPC vesicles. The proteoliposomes were then extruded following the similar method as used in preparing the lipid vesicle suspension, leading to the size distribution between 96 and 124 nm with the maximum around 109.8 nm which is slightly larger than the pore diameter of our alumina substrate (original 80±10 nm and after gold coating 60±15 nm).

2.2.2 Membrane permeability measurements

The permeability of two kinds of vesicles (liposome and proteoliposome) was determined using the stop-flow method (Chirascan Circular Dichroism Spectrometer, Applied Photophysics, UK). Vesicles were rapidly mixed with a hyperosmolar sucrose buffer which can cause water permeating from vesicle to an environmental solution. The reduction of vesicle volume was detected by a 90° light scattering at a wavelength of 577 nm in the stopped-flow apparatus. The measuring temperature was 25°C. A signal increase, which was caused by vesicle size reduction, was fitted to an exponential rise equation as follows:

$$Y = A_s \exp(-kt) \tag{2-1}$$

where Y is the intensity of signal, t is the recording time, in s, A_s is a constant (always negative), k is the initial rate constant, in s^{-1}. The osmotic water permeability P_f(m/s) was calculated from Equation (2-2) [37]:

$$P_f = \frac{k}{(S_0 / V_0) V_w \Delta_{osm}} \tag{2-2}$$

where k is the rate constant obtained from light scattering signal, S_0 (m^2) and V_0 (m^3) are the initial surface area and volume of the vesicle, respectively. V_w is the molar volume of water (18×10^{-6} m^3/mol) and Δ_{osm} is the osmolarity difference that drives the vesicle shrinkage.

2.2.3 Preparation of membrane substrates

To explore the effects of different interface interactions on the local mechanical strength of biomimetic membranes, two configurations were designed as illustrated in Figure 2-1.

In design A, vesicles were ruptured directly on a porous alumina (Synkera technologies, Inc., USA). For design B, a gold coated porous alumina was modified by physical vapor deposition of a 60 nm gold layer. Then, Carboxyl-PEG-SH (molecular weight: 3500 Da) (JenKem Technology USA Inc. 1mg/mL ethanol solution) was incubated upon the gold coated porous alumina for more than 24 hours at 35 °C so that the PEG molecules were chemisorbed on gold by self-assembly of thiol groups. Finally, the vesicles were ruptured on the PEG polymer cushion.

2.2.4 Preparation of pore-spanning membranes and morphology observation by AFM

DMPC liposomes or DMPC- aquaporin Z (AqpZ) proteoliposomes were ruptured on the porous alumina at a temperature above the phase transition temperature of DMPC. The morphologies of the substrate and the pore-spanning membrane were observed by AFM via contact mode using a triangle silicon nitride tip (Agilent technologies, USA, normal constant 0.08 N/m, tip radius <10 nm). The deflection sensitivity was measured on a piece of clean silicon wafer in ultrapure water. The exact spring constants of the cantilevers were determined by the thermal noise method. The force for imaging was maintained around 200 pN. The imaging was performed in water.

2.2.5 Force indentation by AFM

The local mechanical properties of the membrane in each case were tested by conducting force indentation experiments in the centre of the unsupported membrane-covered pores with a constant piezo-electric velocity of 0.5 m s^{-1} at a temperature of 20±1 ºC in water.

Typically, we recorded the force curve for more than 150 times at different pores, providing good statistics.

Upon indentation, a normal force will be applied on the pore-spanning membrane. If the membrane is fixed on the substrate, there will be an increase in the lateral tension. The two-dimensional (2D) Young's modulus may be applicable to describe the lateral tension within the membrane between AqpZ and DMPC, as the maximum strains produced from these interactions can be represented by the Young's modulus. To relate the normal force to the lateral tension within the membrane, a linear response represented by a 2D Young's modulus was assumed. The lateral tension can be related to membrane area dilatation by using Equation (2-3) [87].

$$\sigma_s = E_{2D}\left(\frac{\Delta S}{S}\right) \tag{2-3}$$

where σ_s is the lateral tension, in N/m, E_{2D} is the Young's modulus in N/m, ΔS and S are the dilatation area and pore-spanning membrane area, in nm^2, respectively.

The resultant membrane area after indentation can be estimated by assuming that the curved surface area is part of a hemisphere surface area as shown in Figure 2-2. Hence, the area expansion can be calculated via Equation (2-4) [87]:

$$\frac{\Delta S}{S} = \frac{2R_h^2(1-\cos\theta)-r^2}{r^2} \tag{2-4}$$

where r is the radius of the pore, in nm, θ is the angle, in degree. R_h, which is the radius of the assumed hemisphere, in nm, can be calculated by this equation: $R_h = \left(r^2 + h^2\right)/2h$, (h is the penetration depth, in nm). The elastic energy stored in the membrane can be

calculated by integrating the lateral tension over the surface expansion (ΔS) and expressed by Equation (2-5) [87]:

$$\Omega = 0.5SE_{2D}\left(\frac{\Delta S}{S}\right)^2 \tag{2-5}$$

To simplify the calculation in the next step, θ was assumed to be 60 º according to the topology of the curved surface and ΔS was calculated by the equation $\Delta S = \pi h^2$. The force can thus be estimated by taking the derivative of the elastic energy with respect to the indentation depth h, as written in Equation (2-6) [87].

$$F = 2\pi E_{2D}\frac{h^3}{r^2} \tag{2-6}$$

where r is the hole radius, in nm. The bending rigidity of the membrane can be estimated as ~$0.1E_{2D}d^2$, where d is the bilayer thickness of 4.5 nm.

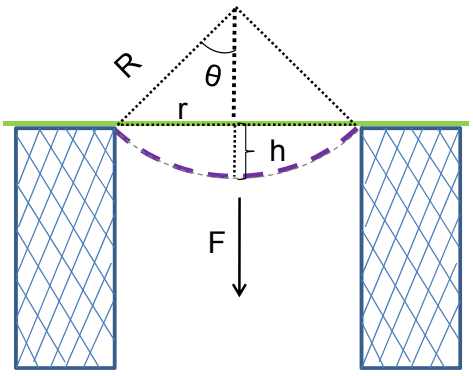

Figure 2-2 Illustration of the membrane area dilatation upon AFM tip indentation. The green line represents the original pore-spanning membrane. The purple dash line represents the area expansion of the membrane. h denotes the penetration depth, r is the pore radius, R is the radius of the assumed hemisphere and F denotes the vertical force exerted by the tip.

2.3 Results and Discussion

2.3.1 Permeability of AqpZ-DMPC vesicles

The permeabilities of DMPC and AqpZ-DMPC vesicles were investigated using a stopped-flow apparatus. Liposomes and preoteoliposomes were rapidly mixed with a 600 mosmol/l sucrose solution as described elsewhere [37]. The efflux of water from vesicle causes an increase of local lipid concentration, which corresponds to an increase in light scattering over time. The initial rise of the light scattering signal was fitted by using Equation (2-1) and the permeability was determined from Equation (2-2). Figure 2-3 shows an example of increase in relative light scattering signals with and without AqpZ into the DMPC membrane at 25 °C. The initial time rise for AqpZ-DMPC vesicles is between 20 and 30 ms, whereas the DMPC vesicles need 4 s to reach equilibrium. The calculated permeabilities of DMPC and AqpZ-DMPC vesicles are 0.08 and 252 cm/s, respectively, which are comparable with those previously reported [37]. The incorporation of AqpZ leads to a 3000-fold greater permeability than pristine DMPC vesicles, thus demonstrating the reconstitution of AqpZ into the DMPC vesicles with a correct configuration. AqpZ was then reconstituted at different protein lipid ratios as shown in Figure 2-4. The observed permeability indicates a remarkable increase as the protein-lipid molar ratio increases from 1:6000 to 1:2000. However, a further increase of protein-lipid molar ratio results in a sharp decrease of permeability. A similar trend was also observed by other researchers. This phenomenon is possibly due to the adopted incorporation method. As the protein-lipid molar ratio increases, the detergent concentration in the mixture also increases. A larger amount of detergent is presented in the system than lipids. Thus, further investigation will be needed to understand how to

effectively remove a large amount of detergent in the mixture to incorporate AqpZ into lipid vesicles.

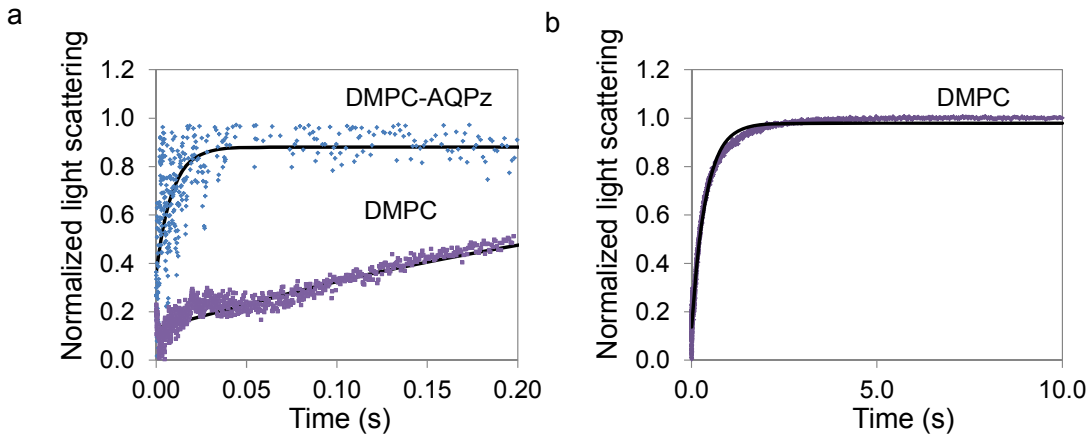

Figure 2-3 The kinetics of water permeability through vesicles in a stopped-flow apparatus. An increase in light scattering signal represents a reduction in vesicle volume due to water flux. The data were normalized to between 0 and 1. The solid lines represent the exponential fitting curves. (a) Increase in the relative light scatting with and without AqpZ into DMPC vesicles at the lipid to protein molar ratio of 2000:1. (b) The rise in light scattering between 0 and 10 s for the DMPC vesicles.

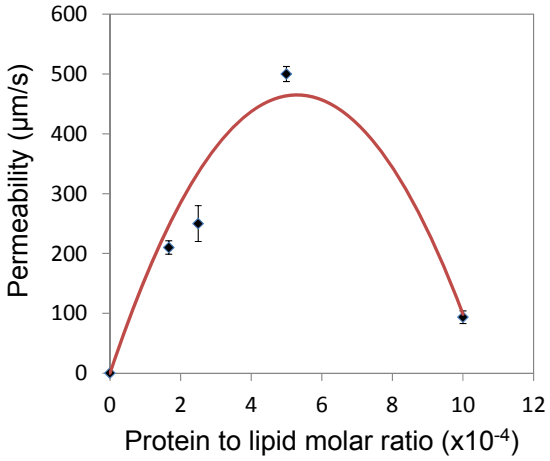

Figure 2-4 Effect of increase AqpZ content on the permeability of DMPC vesicles.

2.3.2 Morphology of pore-spanning bilayers

By examining the FESEM images of the empty alumina substrates (Figures 2-5a and b), the pore diameters before and after gold coating are estimated to be 80±10 nm and 60±15 nm, respectively. The pore size is narrowed down because the deposited gold nanoparticles form another layer on the surface of the porous alumina. Figures 2-5c & d show the hexagonal structure using AFM and the pore-to-pore distance (distance between two valleys) remains about 170±10nm before and after gold coating. The theoretical maximal penetration depth (h_{depth}), which is dependent on both the tip geometry (i.e., the radius of the tip, R_{tip}) and the pore topology (i.e., the radius of the pore, R_{pore}), is about 80 nm for pristine porous alumina and 45 nm for gold coated alumina, by using this equation $h_{depth}=R_{pore}^2/2R_{tip}$ [88]. In practice, our experiments show that the penetration depth (the shortest distance between the peak and the valley) observed from the profile in Figure 2-5 is 45±15 nm for the empty substrate, reduces to 40±10 nm after gold coating, and further decreases to 20±5 nm after carboxylated-PEG chemisorbed on the gold-coating layer. The morphologies shown in Figures 2-5d and e indicate that PEG cushion not only yields a smoother the surface, but also narrows the pore size. One can easily identify membrane-covered and –uncovered pores from the height profile of these two designs in Figures 2-5f and g. Comparisons of penetration depth between Figures 2-5c and f as well as 2-5e and g show that there is a significant drop in penetration depth (i.e., from 45±15 nm down to 15±5 nm and from 20±5 nm down to 10±5 nm, respectively), revealing that DMPC liposomes have spread and formed pore-spanning membrane on top of the porous alumina. The observed images of pore-spanning membrane are comparable with those shown in literature [88]. At the moment, FESEM was used to identify the pore

coverage of the membrane. As shown in Figure 2-5 h and i, the pore coverage of the membrane on the PEG cushion is about 70-75% which is much higher than the one without any cushion, indicating the presence of PEG cushion on the support enhances the membrane mechanical stability. Nevertheless, such technique may underestimate the membrane area, because the membrane could be damaged in the process of sample preparation, such as freeze-drying process.

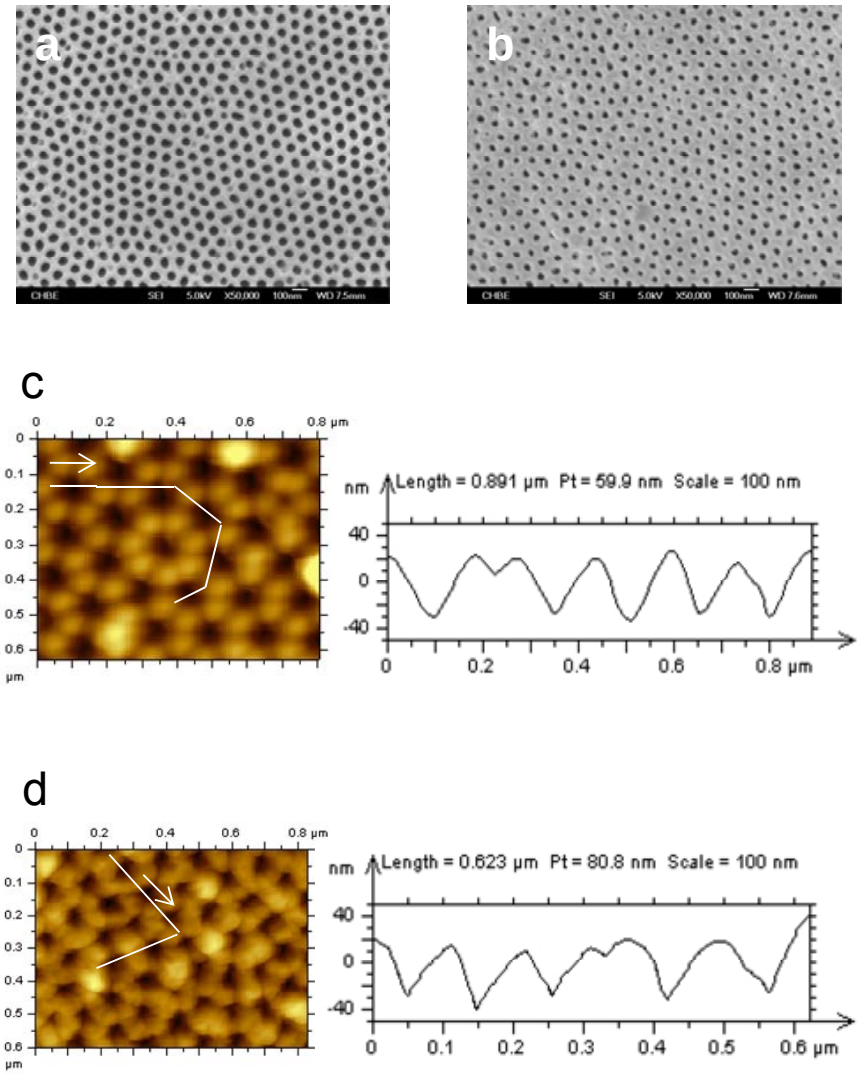

e

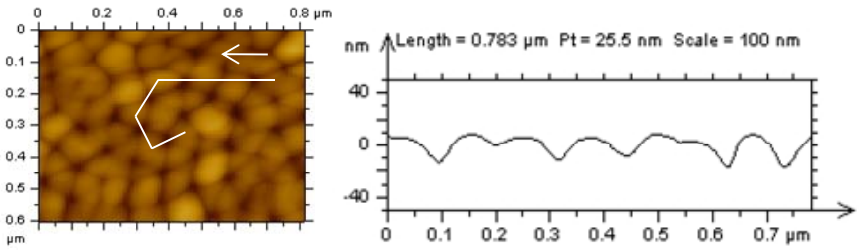
0 0.2 0.4 0.6 0.8 µm
0 0.1 0.2 0.3 0.4 0.5 0.6 µm
nm
Length = 0.783 µm Pt = 25.5 nm Scale = 100 nm
40
0
-40
0 0.1 0.2 0.3 0.4 0.5 0.6 0.7 µm

f

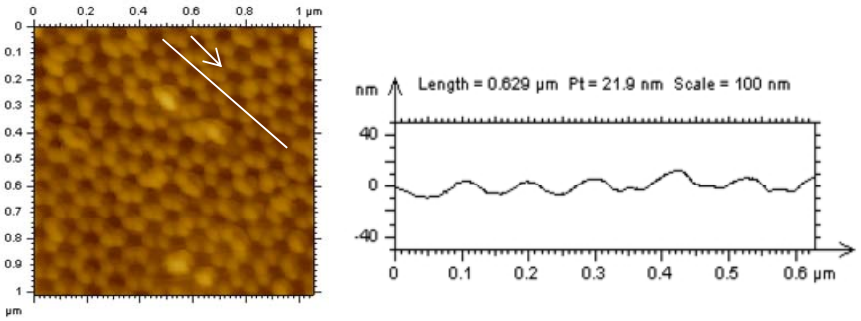
0 0.2 0.4 0.6 0.8 1 µm
0 0.1 0.2 0.3 0.4 0.5 0.6 0.7 0.8 0.9 1 µm
nm
Length = 0.629 µm Pt = 21.9 nm Scale = 100 nm
40
0
-40
0 0.1 0.2 0.3 0.4 0.5 0.6 µm

g

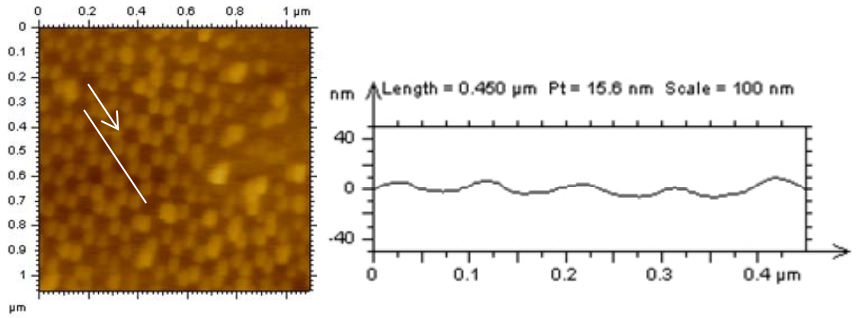
0 0.2 0.4 0.6 0.8 1 µm
0 0.1 0.2 0.3 0.4 0.5 0.6 0.7 0.8 0.9 1 µm
nm
Length = 0.450 µm Pt = 15.6 nm Scale = 100 nm
40
0
-40
0 0.1 0.2 0.3 0.4 µm

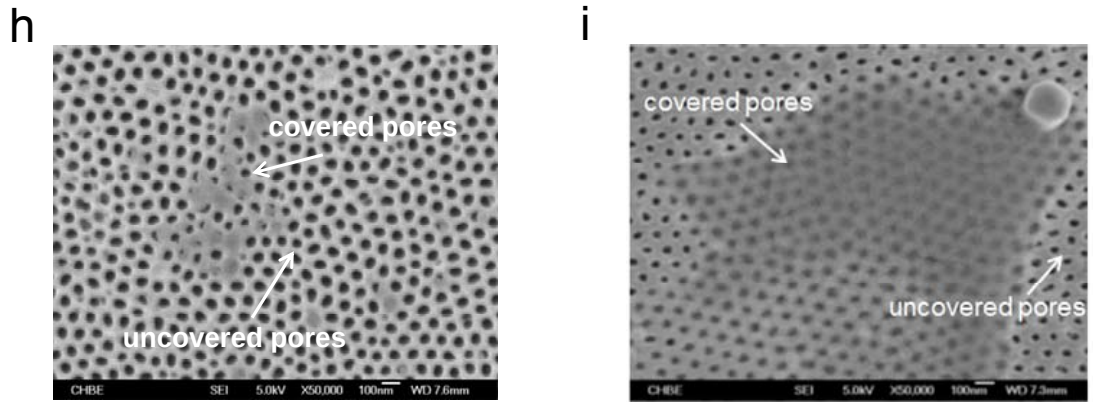

Figure 2-5 Field Emission Scanning Electron Microscope (FESEM) images of alumina substrates. (a) before and (b) after gold coating; AFM images of substrate and pore spanning DMPC membranes on different designs (c) plain porous alumina; (d) porous alumina coated with a 60 nm gold layer; (e) carboxylated PEG 3500 chemisorbed gold-coated porous alumina; (f) DMPC membrane in design A; (g) DMPC membrane in design B. (The white arrows indicate in the direction from which the pore to pore depth profiles were obtained. The profiles of penetration depths are along the white line.) (h) FESEM image of the DMPC membrane on the pristine alumina substrate. (i) FESEM image of the DMPC membrane on the PEG cushioned alumina substrate.

2.3.3 Force indentation measurements

The force indentation measurements were performed in the centre of the pore-spanning membrane in order to obtain the elastic response of the membrane. The typical force indentation curve obtained from membranes in Figure 2-6 is similar with previous reports [82, 87]. After the initial contact between the tip and the membrane, the membrane is indented until rupture happens (Figure 2-6). The maximal force that the membrane can sustain is dependent on the intrinsic lateral tension and bending rigidity of the membrane. After rupture, the cantilever suddenly relaxes until the tip reaches the maximum penetration depth of the pore.

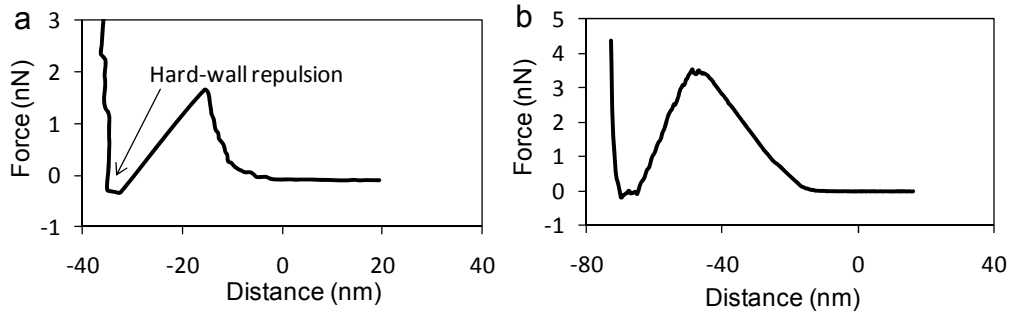

Figure 2-6 Representative force indentation curves of pore-spanning biomimetic membranes (a) DMPC membrane in design A, (b) DMPC membrane in design B.

2.3.4 Effect of carboxylated-PEG on the local mechanical stabilities of membranes

In design B, a dense PEG cushion layer was grafted on the porous alumina through chemisorption. The PEG can work as a cushion for AqpZ, due to that the transmembrane protein is about 1 nm higher than the lipid bilayer from the bottom. In addition, the negatively charged surface can enhance the spreading of DMPC vesicles [89].

The histograms of breakthrough forces of the pristine DMPC bilayer membrane as a function of design configurations are shown in Figures 2-7 a and c. The membrane suspended on the substrate consisting of a carboxylated-PEG coating layer (i.e., deign B) exhibits an average breakthrough force of 2.3±2.1 nN, which is relatively comparable to the one formed directly on the pristine alumina substrate (i.e., deign A). However, the former shows a narrower rupture force distribution compared with the latter. This is due to the fact that the PEG polymer layer may smooth the rough alumina surface with its soft polymer chains. In other words, a smooth surface can ease packing of lipids, effectively dissipate indentation stresses and improve the membrane stability, while a spike-like

structure on the substrate surface may lead to discontinuous lipids packing and decrease membrane stability under indentation because of less flexibility [90].

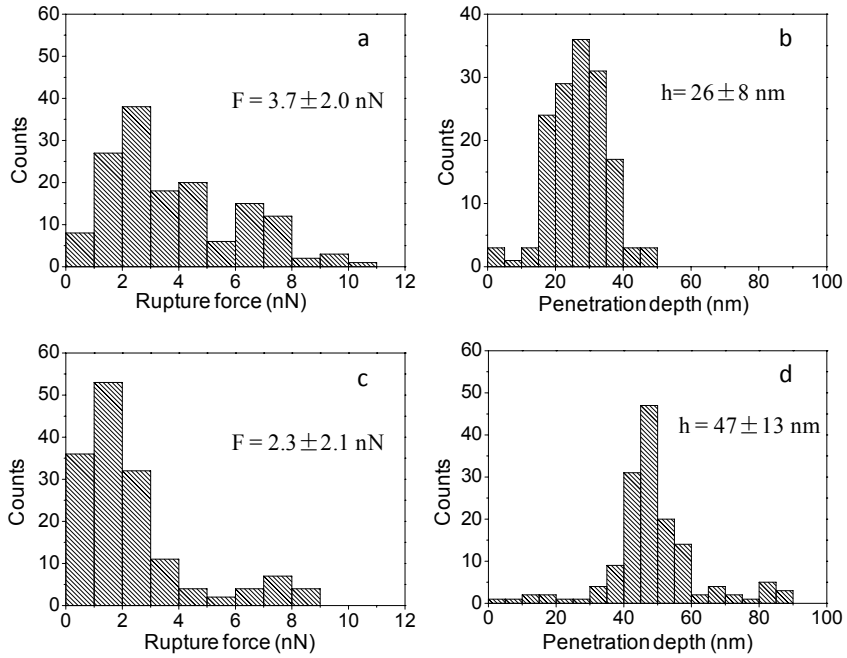

Figure 2-7 Histograms of rupture forces and their corresponding indentation depths (a, b) DMPC membrane in design A; (c,d) DMPC membrane in design B. The mean values of rupture force, F, and its corresponding penetration depth, h, are denoted on the diagrams.

The significant difference in membrane dilatation between the two designs (Figures 2-7 b and d) may give a strong support for the aforementioned hypothesis. By adopting the geometry of a hemisphere to imitate the surface morphology of the indented membrane, the dilatation of the membrane in design A is about 0~4% (Equation (2-4)). However, the total distance between the initial contact and the rupture point in the force-distance curve of the membrane in design B are tens of nanometer larger (26±8 vs. 47±13 nm, Figures 2-7b and d). A dilatation of 15-30% can be calculated from the penetration depth by using Equation (2-4). Assuming that the boundary of the lipid bilayer membrane is affixed on

the substrate, a pure stretch of a lipid bilayer without rupture should be only less than 5% of area dilatation [82]. The difference in dilatation value implies that the lipid layer may flow from the edge into the pores upon indentation due to the soft PEG polymer cushion in design B increases the flexibility between the membrane and the substrate. In contrast, the strong interfacial adhesion between the membrane and substrate surface creates a lateral tension in the membrane that hampers the flow in design A.

2.3.5 Effect of AqpZ on the local mechanical stability of membranes

The pore-spanning membrane with AqpZ incorporated was also prepared by vesicle fusion on the PEG modified substrate (i.e., design B). As observed by previous researchers, only about 50% of the activity of transmembrane proteins in the supported planar lipid layer can be preserved by vesicle fusion, because the method of vesicle rupture can result in two opposite protein orientations [91]. However, aquaporin is a bidirectional water channel; hence the orientation of transmembrane protein is not critical during vesicle fusion in this case. In fact, it was also found in literature that the phosphodiester groups on lipids in direct contact with a membrane protein associate tightly with transmembrane proteins [92]. Thus, the AqpZ can still retain its correct configuration after vesicle fusion, provided that there exists zero steric hindrance in the periphery.

The pore-spanning membranes with or without AqpZ incorporation are indistinguishable under AFM imaging because of several reasons. Other than the low AqpZ to lipid molar ratio, the main reason is that the height of AqpZ is only 1nm larger than the lipid bilayer,

which makes differentiation on a relatively rough substrate virtually impossible. Nevertheless, we can distinguish them from the histograms of rupture events before and after AqpZ incorporation, since they are strikingly different as shown in Figures 2-7c, d and 2-8.

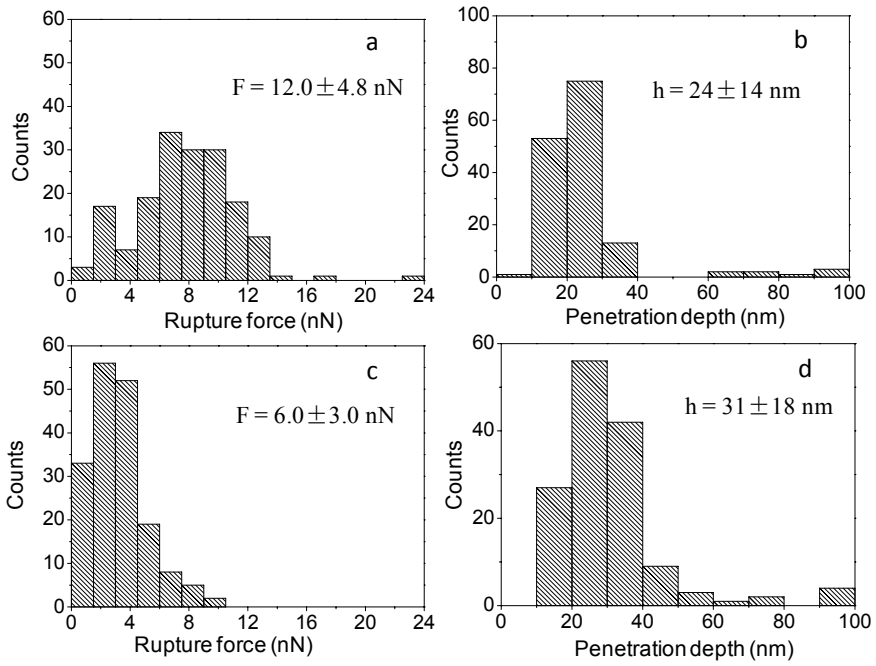

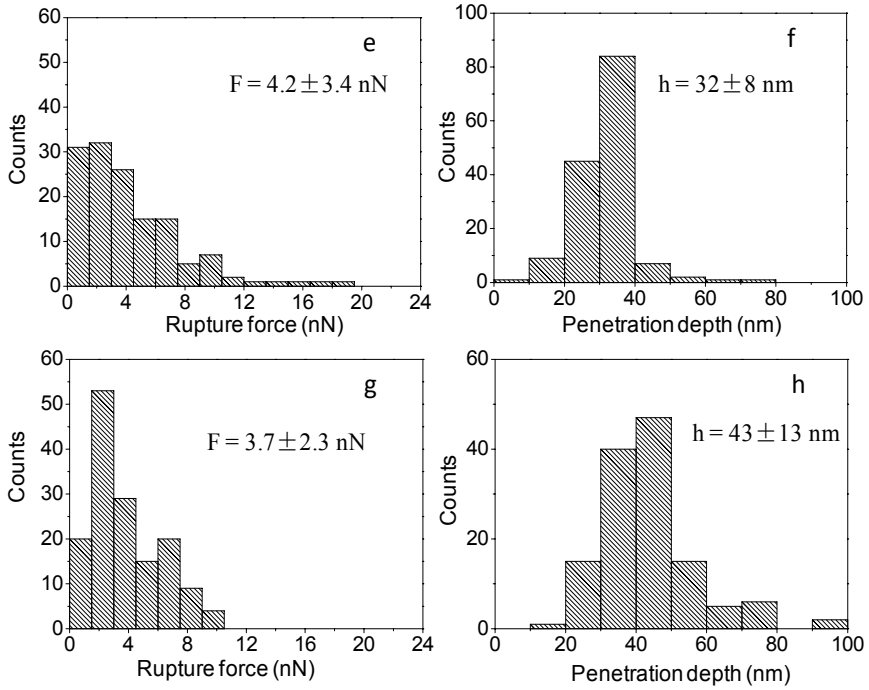

Figure 2-8 Histograms of rupture forces and their corresponding indentation depths using design B: (a, b) DMPC-AqpZ membrane LPR 1000:1, (c,d) DMPC-AqpZ membrane LPR 2000:1, (e,f) DMPC-AqpZ membrane LPR 4000:1, (g,h) DMPC-AqpZ membrane LPR 6000:1. The mean values of rupture force, F, and its corresponding penetration depth, h, are denoted on the diagrams.

The histograms of the breakthrough force of membranes with different content of AqpZ are shown in Figures 2-8a, c, e and g. After AqpZ incorporation, the average breakthrough force increases compared with the pristine DMPC bilayer. Even at a very high lipid protein ratio (LPR=6000), the increase of the average breakthrough forces is visible. As the LPR ratio decreases from 6000 to 1000, the breakthrough force increases drastically from 3.7 to 12.0 nN. This phenomenon is attributed to the fluidity of the membrane and the lateral tensions between AqpZ molecules and lipids. Firstly, as the LPR value is ~ 6000, the penetration depths are quite similar to the one containing no AqpZ (Figures 2-7d and 2-8h). The area dilatation is about 15-30% by using Equation (2-

4) (higher than 5%), which is not pure stretch as described previously [82]. Thus, it is hypothesized that at a high LPR value, the membrane could still flow from periphery into pores upon indentation due to the weak interfacial interaction between the membrane and the PEG cushion. A further decrease in LPR value to 1000:1, the penetration depth decreases to an extent that the dilatation is within 5-15% (Figure 2-8b). Such dilatation is still higher than the dilation of the pristine lipid membrane, but it is more closely to the cell membrane as reported in literature [87].

The 2D Young's modulus, E_{2D}, of the pore-spanning DMPC membrane in design A is estimated to be 0.06 ± 0.05 N/m on average via Equation (2-6). This value is obtained from the solvent-free lipid layer, which is only about one third of the natural cell membrane owing to the adhesion of the natural cell membrane to the extracellular matrix and the coupling of the lipid bilayer to the cytoskeleton [93]. The lateral tension, σ, of such a membrane is then estimated to be (2.1 ± 1.7) $\times 10^{-3}$ N/m using Equation (2-3), which is slightly higher than the tension reported using diphytanoylphosphatidylcholine (DPhPC) membrane [82]. Using the same method, the E_{2D} and σ of the DMPC-AqpZ (LPR 2000:1) membrane are estimated to be 0.13 ± 0.09 N/m and (1.3 ± 0.9) $\times 10^{-2}$ N/m, respectively. The value of E_{2D} is close to a natural cell membrane 0.2 N/m [87]. Under these conditions, the reconstitution of AqpZ increases the energy barrier required for a normal force to punch through, mimicking the natural cell membrane. The bending rigidity of the DMPC-AqpZ (LPR 2000:1) membrane (~59k_BT) is larger than the bending modulus of a pristine DMPC bilayer (~13 k_BT) [94]. As the LPR value decreases to 1000:1, the bending rigidity increases to ~160k_BT, indicating that the AqpZ molecules

may respond to mechanical stresses less actively than DMPC molecules.

2.4 Conclusions

In summary, as a first step towards the pore-spanning biomimetic membrane for possible application in FO, AqpZ molecules were successfully incorporated into DMPC vesicles and the resulting DMPC-AqpZ vesicles were spread on the substrate to form pore-spanning biomimetic membrane. Meanwhile, the interfacial interactions between the DMPC-AqpZ membrane and the substrate were investigated in terms of local mechanical stability. Upon reconstitution into DMPC vesicles with an optimal ratio, AqpZ displays a 3000-fold greater permeability than the pristine DMPC vesicles. The results are comparable with the performance of AqpZ in the *Escherichia coli* lipid vesicles. Thus, DMPC lipids are compatible with AqpZ molecules. The reconstitution of AqpZ in a pore-spanning planar membrane increases the energy barrier required for a normal force to punch through the membrane but decreases the flexibility of the membrane. Consequently, the local mechanical stability of the membrane is enhanced by increasing the AqpZ content. However, the local mechanical stability that can be reached is limited in practice as the highest performance of the AqpZ can only be achieved with an optimal DMPC-AqpZ ratio. For the substrate and the membrane interfacial interaction, the surface functionalization with carboxylated-PEG improves the flexibility of the membrane, as such that the carboxylated-PEG grafted porous alumina exhibits a promising platform for pore-spanning biomimetic membrane fabrication.

CHAPTER 3: Highly permeable and selective pore-spanning biomimetic membrane embedded with AquaporinZ

3.1 Introduction

The major challenges in current polymeric membranes are how to molecularly design semi-permeable membranes with minimal defects and how to diminish the sublayer resistance and effects [12-15, 95]. Biological membranes overcome these problems by ingeniously embedding highly selective water channels, namely Aquaporins (Aqps), across ultrathin phospholipid bilayers. In the Aqp family, AqpZ is of particular interest for FO applications, not only because AqpZ is the smallest and simplest member but also because the protein can be expressed in Escherichia coli (E. coli) and purified in high concentrations [96]. It is known that a single AqpZ molecule is a tetramer and the water permeability of each subunit is above 10×10^{-14} cm^3/s [37]. Therefore, a biomimetic membrane comprising AqpZ and ABA block copolymers at a molar ratio of 1:50 may possess water permeability of 167 μm/s/bar [18], which is far superior to the current state-of-the-art FO polymeric membranes [11]. Thus, the primary motivation of this work is to demonstrate the fabrication of an AqpZ embedded pore-spanning biomimetic membrane.

In the past few years, Kumar et al have demonstrated that AqpZ can be incorporated into ABA block copolymer vesicles other than just lipid vesicles [18]. Nielsen has sketched out a general strategy to design biomimetic membranes in which channel proteins are embedded in an amphiphilic matrix on a porous hydrophobic partition with soft cushions to support the membranes [79]. Several endeavors have taken this approach but conceptual demonstration remains challenging [77, 97]. Other possible designs of flat-sheet AqpZ embedded biomimetic membranes have also been proposed in some patents and literatures for seawater desalination and osmotic power generation [98]. However, so far no detailed experimental results regarding to the function of AqpZ in these designs have been presented to support their feasibility. The key hurdles in designing such planar biomimetic membranes are (a) defects formed owing to the thin and fragile self-assembled amphiphilic matrix; (b) low coverage of the porous substrate; and (c) delamination at the interface between the selective layer and the substrate. In addition to overcoming these hurdles, maintaining the functionality of AqpZ is another challenge. Thus, despite several years of research, the incorporation of AqpZ in biomimetic membranes has seen only limited progress.

3.2 Experimental Methods

3.2.1 PCTE membrane surface modification

A porous PCTE membrane was modified by physical vapor deposition of a 50-60 nm gold layer. The gold-coated PCTE membrane was then incubated with cysteamine solution (0.5 mg ml^{-1} in 1x PBS buffer) for 12 h at 4 ºC. The modified PCTE membrane was further activated by N-hydroxysuccinimide/ 1-ethyl-3-(3-dimethylaminopropyl)

carbodiimide (NHS/EDC) (1:4 molar ratio, in PBS buffer) and the resultant membrane was immersed in acrylic acid (1% wt in PBS buffer) for more than 12 h at 4 ºC. The membrane substrate was washed thoroughly before use. In order to confirm the surface modification, the X-ray photoelectron spectroscopy measurements were performed by using Kratos AXIS Ultra DLD spectrometer equipped with an Al Kα monochromatized X-ray source. The atomic concentration of each element on the surface was estimated by photoemission peak areas. Spectral analysis was done by using the Gaussian-Lorentzian function.

3.2.2 ABA block copolymer vesicles preparation and AqpZ incorporation

Vesicle suspension was prepared using the film rehydration method. The dry film of ABA block copolymer Poly(2-methyloxazoline)-*b*-poly(dimethylsiloxane)-*b*-poly(2-methyloxazoline) with acrylate ends ($PMOXA_{12}$-$PDMS_{54}$-$PMOXA_{12}$, M_n 6000, Polymer Source Inc. Canada) (5 mg) was rehydrated with an appropriate amount of AqpZ solution (1 mg/mL in 1% dodecyl-β-d-maltoside, DDM). Sequentially, 1×PBS buffer (1 mL) was added during formation of the block copolymer vesicles and the mixture was stirred until a homogeneous mixture was formed. The detergent was then removed by adding biobeads (0.05g) stepwise. The proteopolymersome samples (2 mg/mL) for stopped-flow tests were then extruded 21 times using PCTE membranes (pore size: 100 nm). Another set of proteopolymersome solutions was extruded 21 times through the PCTE membrane (pore size 200 nm) and was then used for vesicle adsorption and rupture experiments. The mean diameters of vesicles were measured at 24 °C with a Malvern Zeta Sizer light

scattering apparatus (3 repeats per measurement). The mean diameters were determined with the Malvern Zetasizer software.

3.2.3 AqpZ incorporation and stopped-flow tests

The permeability of vesicles was determined using the stopped-flow method (Chirascan Circular Dichroism Spectrometer, Applied Photophysics, UK). The process is the same as described in section 2.3.2.

3.2.4 Critical pressure determination

The acrylate-functionalized PCTE membranes, with average pore sizes of 50, 100 and 400 nm, were mounted on a ceramic funnel with a porous support at the bottom. A series of pressures were applied to the ABA polymer vesicle solution at a concentration of 2 mg/mL. The flow rates of vesicle solutions were monitored. A series of applied hydraulic pressures (ΔP_L) as well as the products ($\eta_L Q_L$) of flowrates (Q_L) and viscosities (η_L) were fitted with Darcy's law:

$$\eta_L Q_L = K_L \left(\frac{\Delta P_L}{\Delta L_m} \right) \qquad (3\text{-}1)$$

where ΔL_m is the length of the membrane channel and K_L is a coefficient that is related to number and diameter of the pores on the membrane.

3.2.5 Formation of planar pore-spanning biomimetic membranes through UV crosslinking

The acrylate-functionalized PCTE membrane was mounted on a ceramic funnel with a porous support at the bottom. The proteopolymersome solution, which was saturated with

argon, was dropped onto the surface of the PCTE membrane support upon applying a respective vacuum of about 880, 900, 970 mbar corresponding to the membrane pore size 50, 100 and 400 nm. The UV crosslinking of AqpZ-ABA vesicles and the acrylate-functionalized PCTE support was performed for 15 min at 4 ºC.

3.2.6 AFM imaging and indentation

The morphologies of the bare PCTE substrate and the pore-spanning membranes were observed in ultrapure water by AFM (Agilent Technology, USA) via contact mode using a rectangular silicon cantilever (Ultrasharp, Estonia, normal constant 0.08 N/m, tip radius <10 nm). The V-shaped silicon nitride cantilever (Olympus, OMCL-TR400PSA, tip radiu 20nm, spring constant 0.08 N m^{-1}) was used for force curve measurements. The deflection sensitivity was measured on a piece of freshly cleaved mica in ultrapure water. The exact spring constant of the cantilever was determined by the thermal noise method. The force distance measurements were conducted with a constant piezo-electric velocity of 0.5 m s^{-1} at a temperature of 22 ± 1 ºC in water. Typically, the force curves were recorded more than 10 times at different locations, providing good statistics.

3.2.7 Measurements of water flux and reverse salt flux in FO set-up

The AqpZ-ABA membrane was clamped in between two Teflon chambers. Each chamber has a volume of about 37.5 cm^3. The effective membrane area was standardized by covering the membrane with a piece of aluminum foil tape with a 3.5 mm diameter hole in the center (area of 9.6 mm^2). During the process, the solutions in both chambers were stirred by overhead stirrers. Water fluxes were measured using ultrapure water as

the feed and NaCl solution as the draw solution and were caluclated based on the weight increase of the draw solution in Equation (3-2).

$$J_w = \frac{\Delta W}{S_m \Delta t} \tag{3-2}$$

where ΔW, in g, is the weight increase of draw solution over timing Δt, in s. S_m is the membrane area, in m^2.

The reverse salt flux is obtained via sampling the feed solution and measuring the variation of conductivity in Equation (3-3).

$$J_s = \frac{\Delta C_f V_f}{S_m \Delta t} \tag{3-3}$$

where ΔC_f is the salt concentration change of the feed, in g/mL; V_f is the final volume the feed, in mL.

The water and reverse salt fluxes were measured as an average over 1 h. The experiments have been carried out to 3 different batches of membranes.

3.2.8 Characterization of salt retention ability and selectivity of AqpZ-ABA pore-spanning membrane

The membrane has been tested by using 0.3M sucrose as draw solution and 200 ppm NaCl as feed solution. The conductivity of the draw solution is very close to DI water, which can be ignored. Therefore, the salt rejection and selectivity can be estimated in Equations (3-4) and (3-5), respectively.

$$Salt \quad rejection = (1 - \frac{C_{d1}}{C_{f0}}) \times 100\% \tag{3-4}$$

$$Selectivity = \frac{(\Delta W - C_{d1}V_{d1})/M_w}{C_{d1}V_{d1}/M_s} \quad (3\text{-}5)$$

where C_{d1} and C_{f0} are the final salt concentration of the draw solution and initial salt concentration of the feed, respectively, in g/mL; V_{d1} is the final volume of draw solution, in mL. The ΔW_d is the weight increase of the draw solution, in g. M_w and M_s are the molecular weights of water (18.02 g/mol) and NaCl (58.44 g/mol) , respectively.

3.2.9 Arrhenius activation energy determination

The FO experiments were conducted over the temperature range of 5 to 37 ºC. The activation energy of water transport through the pore-spanning membrane can be calculated by Equation (3-6).

$$J_w = P_f \cdot \Delta_{osm} \quad (3\text{-}6)$$

where J_w is the water flux, which is related to water permeability P_f.

3.3 Results and Discussion

3.3.1 Pore-spanning biomimetic membrane design

A new scheme to molecularly design the planar pore-spanning biomimetic membrane has been proposed. As shown in Scheme 3-1a, AqpZ proteins are firstly incorporated into triblock copolymer vesicles through typical proteopolymersome synthesis, by which the dried triblock copolymer film of (poly-(2-methyloxazoline)-poly-(dimethylsiloxane)-poly-(2-methyl-oxazoline, end functionalized with acrylate), $PMOXA_{12}$-$PDMS_{54}$-$PMOXA_{12}$, ABA) is rehydrated with an AqpZ-detergent buffer solution. The proteins are then refolded into the ABA polymersomes after the detergent molecules have been

removed by biobeads. In step (b), the surface of polycarbonate tracked-etched (PCTE) substrates is coated with a 60 nm-thick gold layer and a monolayer of photo-reactive acrylate functional groups is deposited on top of the gold surface (Scheme 3-1b). Subsequently, a critical pressure is applied to a proteopolymersome solution above the PCTE substrate so that the proteopolymersomes deform, slightly intrude into and seamlessly cover the pores of the support (Scheme 3-1c). To induce vesicle fusion, UV crosslinking polymerization is carried out, as a covalent linkage is formed between the methacrylate head groups of the ABA polymer and the acrylate residues on the porous PCTE membrane support (Scheme 3-1d).

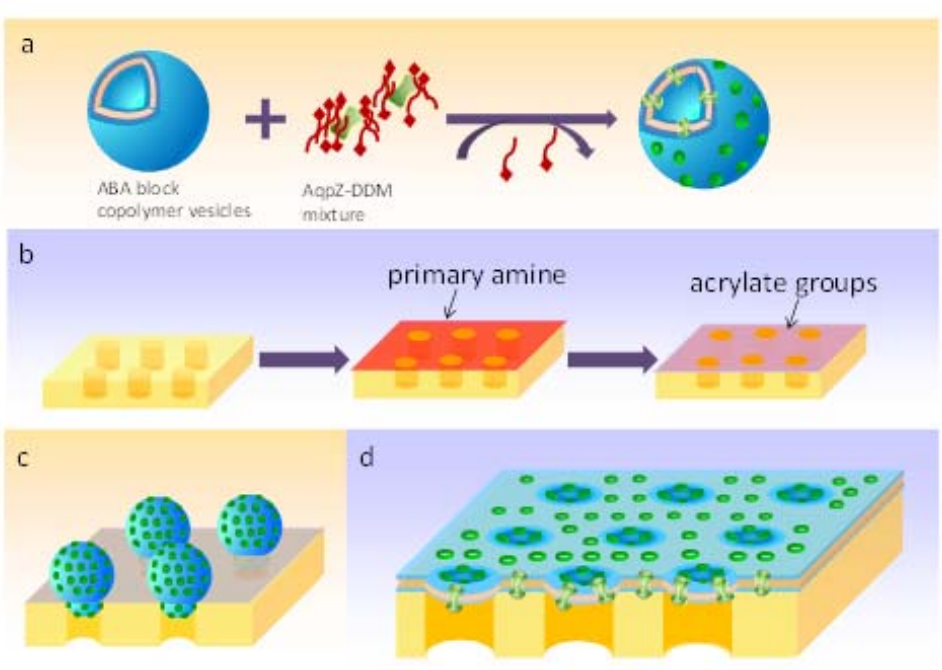

Scheme 3-1 Schematic diagram of pore-spanning membrane design and synthesis: (a) Incorporation of AqpZ in ABA block copolymer vesicles. (b) Surface modification of the PCTE membrane support. A series of PCTE membranes with different average pore sizes (50, 100, 400 nm) are firstly coated with a 60 nm-thick gold layer and sequentially coated with another monolayer of cysteamine through chemisorption. The primary amine residues are converted to acrylate residues via conjugating with acrylic acid. (c) Pressure-

assisted vesicle adsorption on the PCTE support. (d) Covalent conjugation-driven vesicle rupture and pore-spanning membrane formation.

3.3.2 Permeability characterization of AqpZ-embedded vesicles

The water flux and salt rejection of the pore-spanning membrane are dependent on many factors such as AqpZ functionality, substrate surface chemistry, and UV crosslinking efficiency at the interface. To evaluate the properties and better understand the process of pore-spanning polymer membrane formation, we characterized the resultant products at each step of the synthesis.

AqpZ with a 10-histidine residue produced as a recombinant protein in E. coli (Figure A-2 and A-3 in Appendix A-2) was incorporated into ABA polymer vesicles. After extrusion by the PCTE membrane (diameter: 100 nm), the polydispersity indexes of the vesicles are all below or close to 0.1, which indicates that the vesicle samples are reasonably narrow mono-disbursed (Table 3-1). The water permeability of the extruded vesicles was monitored by using the stopped-flow light-scattering experiments [37]. The osmotic pressure triggers water permeation through the vesicles, corresponding to an increase in the light scattering signal over time. As shown in Figure 3-1a, AqpZ-ABA vesicles exhibit an initial rise less than 1×10^{-2} s, whereas no obvious change is observed for pure ABA vesicles until 10 s (Figure 3-1c). The calculated permeability increases from 1700 to 2800 μm s^{-1} and then drops to 1700 μm/s at elevated AqpZ-ABA molar ratios (Figure 3-1b). The estimated water permeability of each AqpZ subunit in ABA (AqpZ: ABA molar ratio = 1:100) is about 42×10^{-14} cm^3/s (Appendix A-3), which is slightly higher than the literature values because of a higher testing temperature in our

study [18]. The permeability decreases significantly when the molar ratio of AqpZ to ABA reaches 1:50, so this ratio was not used for pore-spanning membranes in order to utilize AqpZ efficiently.

Table 3-1 Vesicle size and polydispersity index after extrusion by using100nm PCTE membrane (n=3)

AqpZ-ABA molar ratio	Mean diameter of vesicles [nm]	Polydispersity index (PDI)
1-50	154.7±1.8	0.101±0.01
1-100	149.4±2.7	0.088±0.01
1-200	149.9±0.5	0.058±0.01
1-300	152.7±0.7	0.076±0.01
1-400	144.0±0.4	0.063±0.01
Control (ABA)	152.5±0.5	0.076±0.01

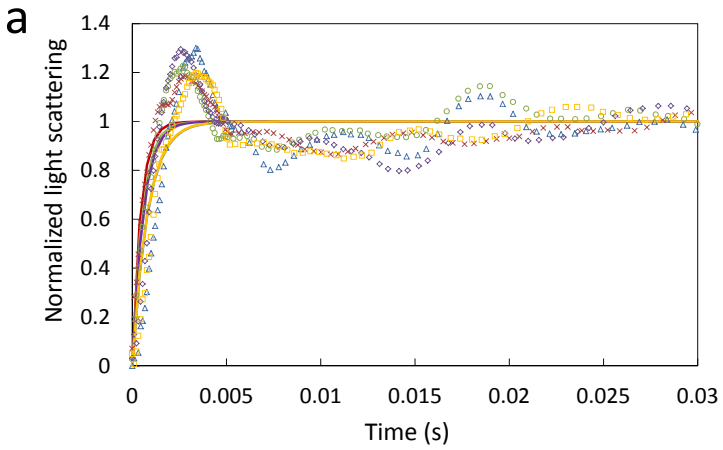

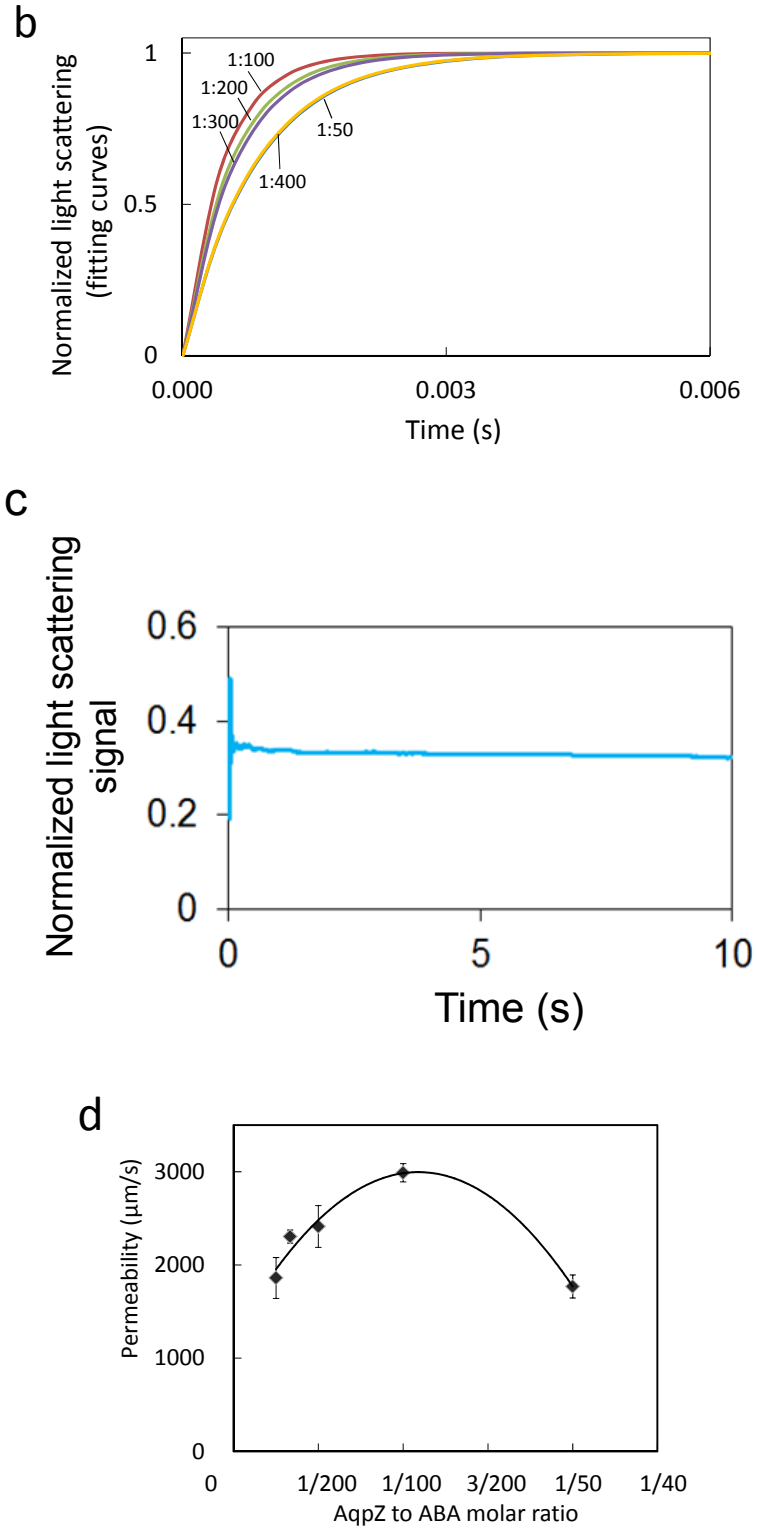

Figure 3-1 Permeability of AqpZ in ABA polymer vesicles. (a) The light scattering response of vesicles in a stopped-flow apparatus. The open symbols Δ, ×, ○, ◊, □

represent AqpZ-to-ABA molar ratios 1:50, 1:100, 1:200, 1:300 and 1:400, respectively. The solid curves represent exponential fittings of the data points which are indicated by the open symbols. (b) The normalized light scattering as a function of the molar ratio of AqpZ to ABA. (c) The light scattering response of the ABA vesicles. (d) The permeability of ABA polymer vesicles varies with AqpZ content, (n=5).

3.3.3 Substrate characterization of pore-spanning biomimetic membrane

The acrylate-functionalized membrane surface has been characterized by XPS. As shown in Figure 3-2, for the amine-functionalized PCTE membrane, the main C-C is at 284.9 eV. The other higher binding energy peak at 285.8 eV represents the C-N bond in the primary amine (CH_2-NH_2). For the amide-functionalized PCTE, an additional higher binding energy peak at 287.6 eV indicates that the primary amine groups are converted to amide groups (-N-C=O-) [99]. According to peak area integration, the conjugation yield is about 85%. The atomic concentration variation in Table 3-2 also implies the primary amine functionalization and conversion from amine to amide step by step.

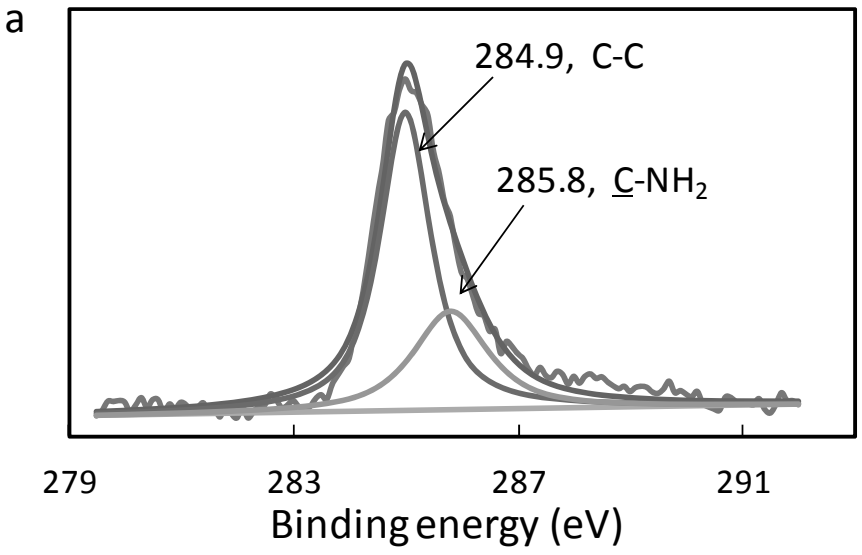

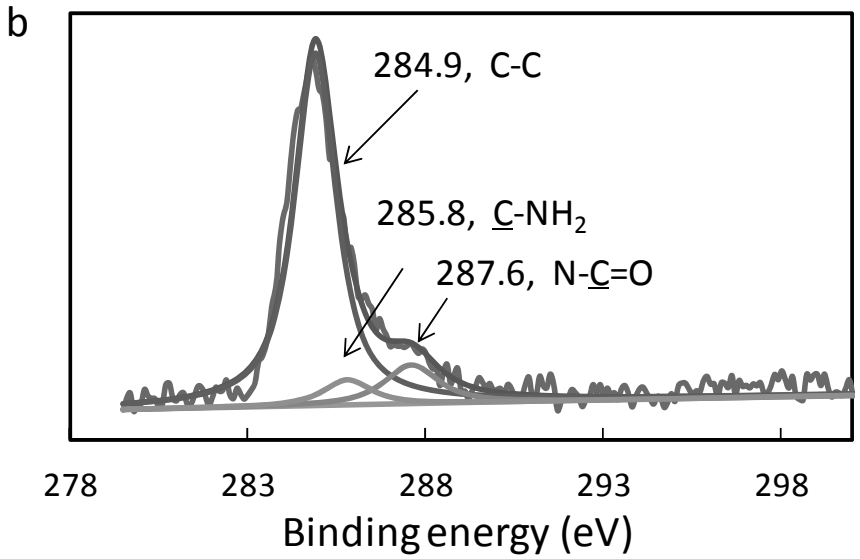

Figure 3-2 XPS spectra of modified PCTE membrane samples (a) amine-functionalized PCTE membrane C1s spectra. (b) amide-functionalized PCTE C1s spectra.

Table 3-2 Comparison among the atomic concentration of the membrane samples via different surface modification

Element	Atomic concentration (before modification) [%]	Atomic concentration (after functionalized with NH_2) [%]	Atomic concentration (after functionalized with acrylate groups) [%]
O	26.04	21.37	25.79
C	73.96	69.93	69.77
N	0	4.83	1.82
S	0	3.87	2.62

3.3.4 Critical pressure for vesicle intrusion

An ideal membrane must ensure that all substrate pores are covered by the AqpZ-ABA membrane. This can be accomplished by seamlessly covering all pores with a layer of vesicles and then causing the vesicles to rupture. A linear relationship is confirmed between the viscosity-corrected flow rate and the applied pressure as predicted by Darcy's law when a large-unilamellar-vesicle (LUV) solution is pushed toward the PCTE

membrane (Figure 3-3) [100]. As obtained through the extrapolation of linear fit in Figure 3-3, the minimum pressures required for the LUVs to block the PCTE support with normal pore sizes of 50, 100 and 400 nm are 100, 84 and 11 mbar, respectively.

Under the critical pressures, a small fragment of the vesicle will partially intrude into the pore and the vesicle will be stuck at the entrance. The pressure across the vesicle is balanced by the force due to the line tension around the neck of the fragment, so that fission will not occur. Above this pressure, the vesicle will be extruded through the holes resulting in small unilamellar vesicles (Figure 3-3).

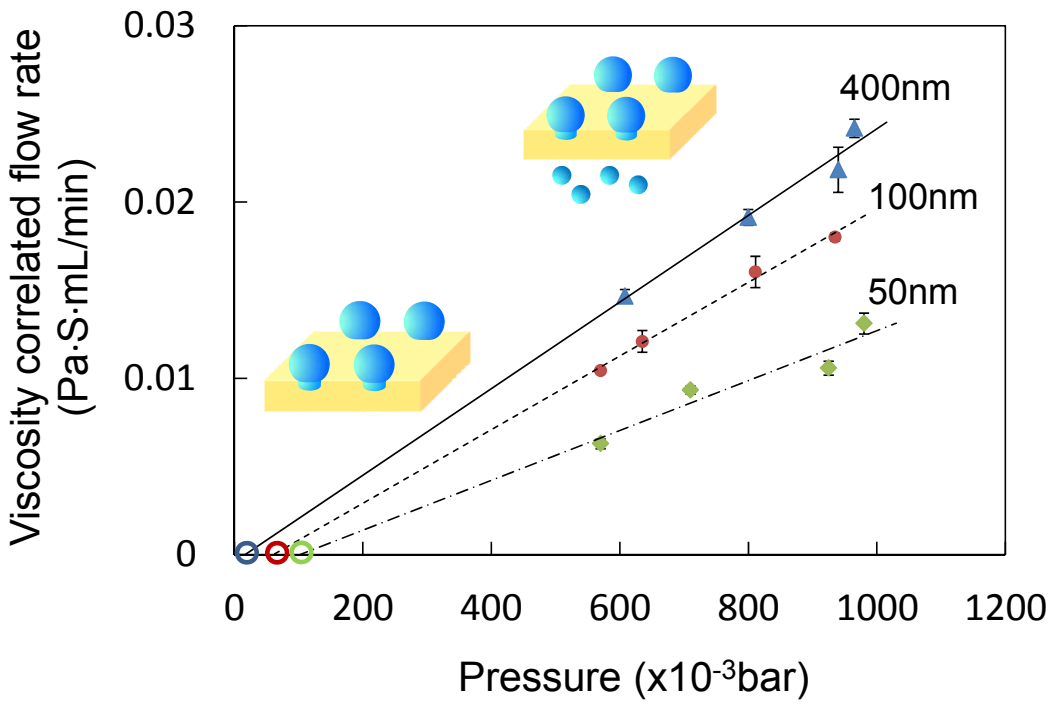

Figure 3-3 Viscosity-correlated flow rate as a function of pressure using PCTE membranes with different pore sizes (n=3). The solid symbols ▲, ● and ♦ represent the viscosity-correlated flow rates of PCTE membranes with pore sizes of 400, 100 and 50 nm, respectively. The three hollow circles on the pressure axis indicate the maximum pressures which the LUVs can sustain (i.e. critical pressure).

3.3.5 Morphological characterization of pore-spanning biomimetic membrane

Figures 3-4 a-c show FESEM images of acrylate-functionalized PCTE supports with pore sizes of 50, 100 and 400 nm, respectively, while Figures 3-4 d-f display the corresponding images of pore-spanning membranes on the supports. Even though the pure water permeability of acrylate-functionalized PCTE membrane supports with pore sizes of 50, 100 and 400 nm are all above 1000 L/m^2/h/bar, the PCTE support with 50 nm pores has far fewer defects as compared to other supports with bigger pores (Figure 3-4). Thus, the PCTE support with 50 nm pores was chosen for further studies. The atomic force morphological images provide additional insights. Figure 3-5b shows that after all the un-adsorbed vesicles have been washed away, many vesicles are still found adsorbing on the surface of the support and covering the visible 50 nm pores as shown in Figure 3-5a. Moreover, statistical analyses prove that the RMS roughness (root-mean-squared roughness) decreases from 4.0 to 3.3 nm over the area of 4 μm^2. After UV crosslinking, the vesicles in Figure 3-5b are ruptured to form the pore-spanning membrane upon the PCTE membrane surface, as shown in Figure 3-5c. Meanwhile, the RMS roughness increases to 3.8 nm over the area of 1.4 μm^2, but it is lower than the RMS roughness of the substrate (i.e. 4.0 nm), which may due to that the pores have been covered. These images suggest that vesicle rupture is driven by covalent conjugation of the vesicle to the membrane support, with crosslinking yield above 70% as determined from Fourier Transform Infrared (FT-IR) analyses (Figure 3-6a). This is not surprising, because the conjugation can only happen between the adjacent methacrylate end groups and acrylate residues, this being highly dependent on the alignment of ABA polymer chains.

Consistent with the thickness measured by transmission electron microscopy (TEM), the average thickness of the pore-spanning membrane was found to be 6 – 8 nm by AFM investigation (Figure 3-6b and c) [86]. Since the unadsorbed vesicles has been washed away before UV crosslinking, it largely decreases the potential to form multilayers of ABA polymer on the support. Therefore, the ABA-AqpZ pore-spanning membrane possesses the hydrophilic-hydrophobic-hydrophilic architecture which is mainly composed of a mixture of monolayer and bilayer.

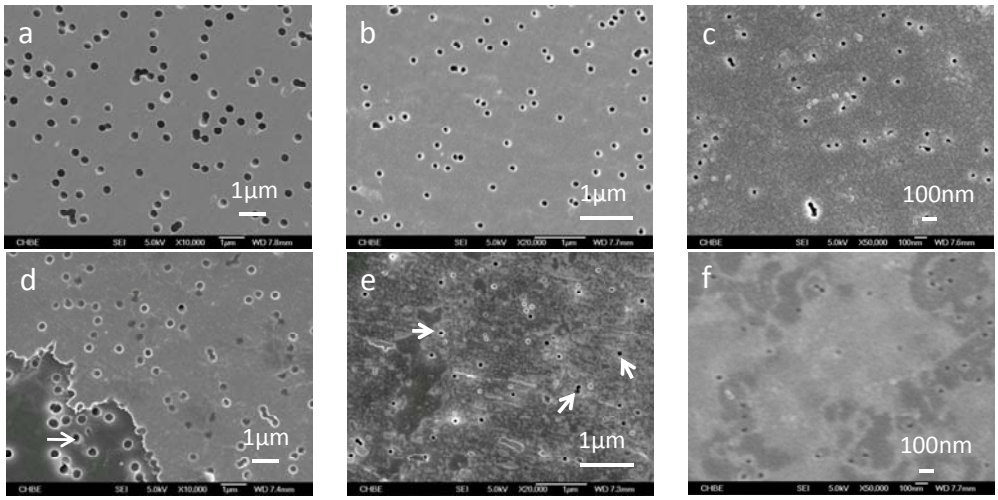

Figure 3-4 Pore-spanning membrane FESEM characterization. (a-c) Surface morphologies of acrylate-functionalized PCTE membrane supports with pore sizes of 50, 100 and 400 nm, respectively; (d-f) Surface morphologies of pore-spanning membranes on supports a, b and c respectively. The white arrows indicate the examples of the unsealed defects.

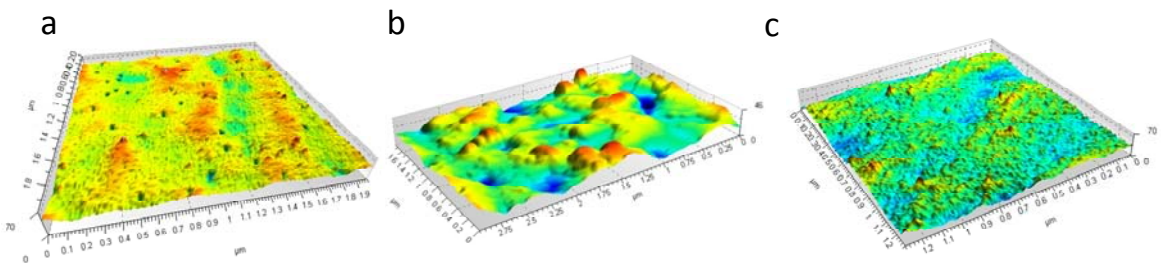

Figure 3-5 AFM surface imaging of pore-spanning membrane. (a) Three-dimensional AFM image of the acrylate-functionalized PCTE membrane support. (b) Three-dimensional AFM image of the acrylate-functionalized PCTE membrane support adsorbed with AqpZ-ABA vesicles. (c) AFM image of pore-spanning membrane ruptured on the acrylate-functionalized PCTE membrane support.

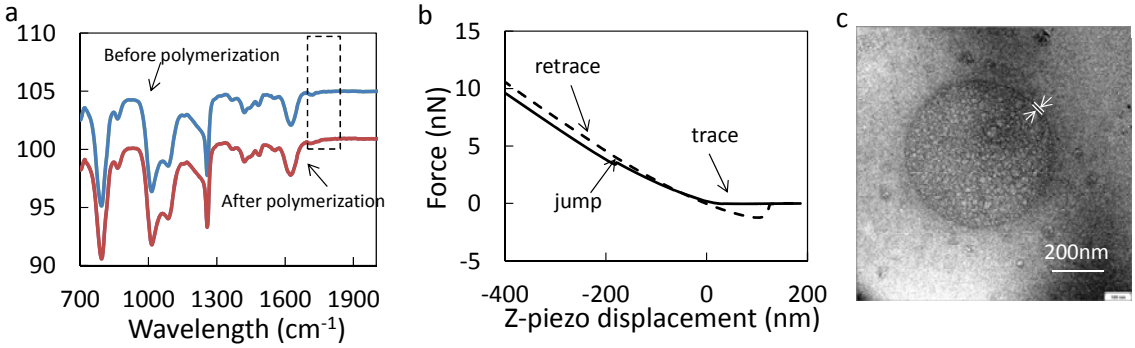

Figure 3-6 Characterization of polymerized thin film. (a) FTIR spectrum of membrane before and after UV crosslinking polymerization. The small peaks that are indicated by arrows on both curves at 1680 cm^{-1} are attributed to the presence of C=C bonds. (b) AFM force piezo displacement curve measured on the pore-spanning membrane. The distinct jump in the approach curve indicates that the AFM tip penetrated through the layer. The 6 nm-jump indicates that the thickness of the pore-spanning layer is ~6 nm. (c) TEM of a large unilamellar vesicle. The thickness of the wall is ~8 nm.

3.3.6 Measurements of water flux and reverse salt flux in FO set-up

The water fluxes of these membranes comprising different AqpZ-to-ABA molar ratios and the control sample without AqpZ were measured using ultrapure water as the feed and NaCl solution as the draw solution. Membranes with an area of 9.6 mm^2 were placed between the two chambers as shown in Figure 3-7a. The water flux increase is almost proportional to the draw solute concentration (Figure 3-7b). The AqpZ-ABA ratio exhibits remarkable positive effects on water flux, indicating that membrane performance relies heavily on the number of active water channels (i.e. AqpZ) embedded in the ABA polymer matrix. The water flux of the biomimetic membrane with an AqpZ-to-ABA

molar ratio of 1:100 reaches 142 L/m^2/h using 2.0 M NaCl as the draw solution. The control samples exhibit negligible water flux and low reverse salt flux (Table 3-3). Although a small number of defects may be inevitable on the pore-spanning layer, the salt reverse fluxes are all below 1×10^{-2} kg/m^2/h, which is comparable with current state-of-the-art polymeric membranes (Table 3-3) [12, 15, 95]. In addition, even though only part of AqpZ proteins remain functional after the amphiphilic matrix transforms from vesicles into the planar form upon vesicle rupture (Appendix A-4), the breakthrough is that this technique enables us to reduce the number of uncovered pores to an insignificant level. In a practical case, in which the membrane was tested by using 0.3 M sucrose as draw solution and 200 ppm NaCl as feed solution, good salt retention ability of the membrane has been demonstrated as salt rejections are all above 90% and the selectivities (water to NaCl) of the membranes are as high as 1.1×10^4 (Table 3-4). Water can transport through the selective layer in two ways: diffusion and channel facilitated transport. The Arrhenius activation energy calculated for the ABA-AqpZ pore-spanning membrane and vesicle are 3.5 kcal/mol and 3.7 kcal/mol, respectively, which are both below the apparent activation energy of self-diffusion of water (i.e. 4.8 kcal/mol) [101]. The ABA vesicles and pore-spanning membrane do not exhibit any measureable flux in the testing temperature range. Thus, our experimental results prove that the AqpZ molecules can facilitate water transport in both vesicles and pore-spanning membranes (Figure 3-8).

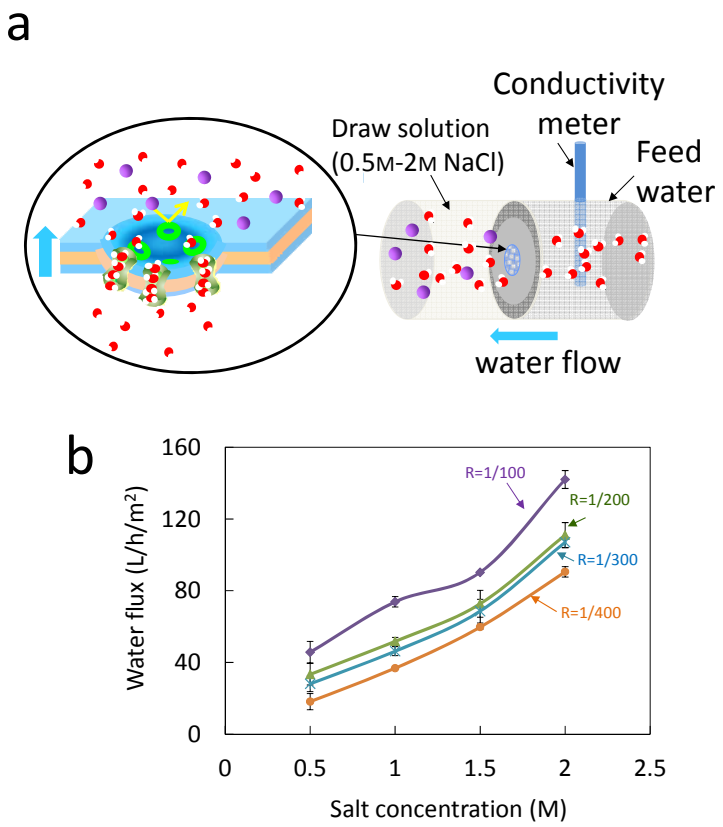

Figure 3-7 (a) Schematic diagram of a static FO permeation cell set-up. The membrane is clamped between the two chambers. The weight increment of the draw solution counts as water flux and the reverse salt flux are monitored by a conductivity meter. The arrows represent the direction of water flow. (b) Plot of water flux versus salt concentration as a function of the molar ratio of AqpZ to ABA polymer (represented by R) (n=3).

Table 3-3 Reverse salt flux as a function of draw solution concentration and AqpZ content in the membrane (n=3)

Concentration of draw solution (M NaCl)	Salt reverse flux (g/m^2/h)				
	AqpZ-ABA (1:100)	AqpZ-ABA (1:200)	AqpZ-ABA (1:300)	AqpZ-ABA (1:400)	Control
2.0	6.2±2.6	10.0±2.0	0.48±0.4	3.7±4.6	4.2±0.1
1.5	7.8±1.1	8.6±0.6	0.6±0.6	2.9±1.6	3.4±0.4
1.0	6.5±0.2	7.1±1.4	0.3±0.02	2.5±0.8	3.2±0.3
0.5	5.4±0.2	4.3±1.7	0.7±0.4	0.7±0.5	2.4±0.3

Table 3-4 Salt rejections and selectivities of the AqpZ-ABA membranes (Draw solution: 0.3M sucrose, feed solution: 200 ppm NaCl) (n=3)

AqpZ-ABA molar ratio	Water flux [L/m^2 /h]	Salt flux [g/m^2 /h]	Salt rejection	Selectivity (water to salt)
1:100	16.4±1.5	0.33±0.04	90.6%	1.6×10^4
1:200	14.3±1.7	0.30±0.09	90.9%	1.6×10^4
1:300	13.6±2.2	0.30±0.08	90.3%	1.5×10^4
1:400	11.3±2.0	0.25±0.06	90.0%	1.4×10^4

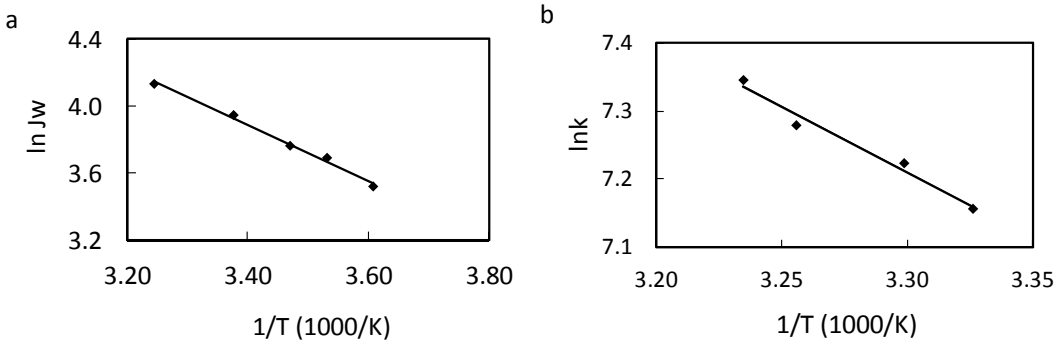

Figure 3-8 Activation energy of water flow across (a) pore-spanning biomimetic membrane (AqpZ to ABA molar ratio 1:100, temperature range: 5 – 37 ºC, regression equation: *ln Jw = 9.57-1.67/T*) and (b) AqpZ-ABA vesicles (molar ratio 1:100, temperature range: 27 – 36 ºC, regression equation: *ln k =13.56 -1.93/T*).

CHAPTER 4: Mechanically robust and highly permeable Aquaporin Z biomimetic membranes (I)

4.1 Introduction

AqpZ-embedded biomimetic membranes are of potential technological significance for freshwater production, but the amphiphilic matrix of the biomimetic membrane is intrinsically fragile, and its structure has to be well-designed for use in technical application [97]. The use of this membrane in water purification processes requires an additional solid support that is sufficiently porous and able to provide mechanical strength for the membrane in the presence of an osmotic gradient or hydraulic pressures [79]. A few attempts have been made to fabricate biomimetic membrane architectures based on the elegant design of nature, such as free-standing lipids membranes [102-104], free-standing block copolymer based membranes [105], hydrogel sandwich supported membranes [48, 106], and hydrophilic-supported pore-spanning membranes [55, 58, 107]. However, there has been very few studies conducted so far that have examined the functions of incorporated Aqps in these membranes that are designed for water purification. Recently, we developed an AqpZ-embedded biomimetic membrane that had a high potential for being used in a forward osmosis (FO) process for water purification. Nevertheless, the fabrication of these membranes through methods such as vesicle rupture and fusion might affect the configuration and the function of these transmembrane proteins. In addition, the mechanical properties of such membranes are

not robust for use over a wide range of applications, because of the thin and the fragile self-assembled amphiphilic matrix that spans the porous support. Therefore, the major challenge that we face in the fabrication of biomimetic membrane is the mitigation of the insufficient mechanical stability while avoiding the possible side effects to the functionality of the AqpZ proteins at the same time.

Introduction of an intermediate layer may help to enhance the interfacial interaction between the selective layer and the substrate. Dopamine, also called "bio-glue", mimics the adhesive protein in the "footprints" of mussels [108]. Polydopamine (PDA) can stick to a wide variety of inorganic and organic materials through the interplay of adhesive and cohesive forces. Via auto-polymerization in the alkaline solution at pH of 8.5, the substrate can be coated with a PDA layer. The resultant surface exhibits latent reactivity towards alkanethiols and amino organosilanes at pH 8.5 as well as imidazoles at pH 7.4 to form self-assembled monolayer-like coatings [108, 109]. Furthermore, the hydrophilic PDA coating layer has been used directly to impart fouling resistance to ultrafiltration, nanofiltration and reverse osmosis membranes [110].

To overcome these challenges, we have implemented a novel robust biomimetic membrane structure and its synthesis route, as shown in Scheme 4-1. AqpZ proteins are reconstituted into ABA block copolymer blends consisting of poly-(2-methyloxazoline)-block-poly-(dimethylsiloxane)-block-poly-(2-methyloxazoline) ($PMOXA_{12}$-$PDMS_{55}$-$PMOXA_{12}$) with acrylate and $PMOXA_{20}$-$PDMS_{75}$-$PMOXA_{20}$ with disulfide end groups, such that the formed unilamellar vesicle could have a mechanically stable hydrophilic

shell with disulfide anchors capable of covalently binding to the gold-coated substrate surface (Scheme 4-1a). To ensure a high coverage of vesicles on the porous support, a critical pressure is used to push the polymerized proteopolymersomes partially into the gold-coated Polycarbonate Track Etch (PCTE) membrane (Scheme 4-1b) [100, 111]. The disulfide bonds on the vesicle surface will tether the vesicle to the channel wall through the disulfide-gold conjugation. Any surface without vesicle immobilization is coated with a self-assembled cysteamine monolayer, which is an intermediate layer to guarantee an effective chemical conjugation between the subsequent polydopamine (PDA) coating layer and the substrate (Scheme 4-1c). The PDA layer can potentially seal the defects between the vesicle surfaces and the pore walls. Then, several cycles of PDA-histidine (His) coating are produced to form a thin network structure on top of the vesicles (Scheme 4-1d).

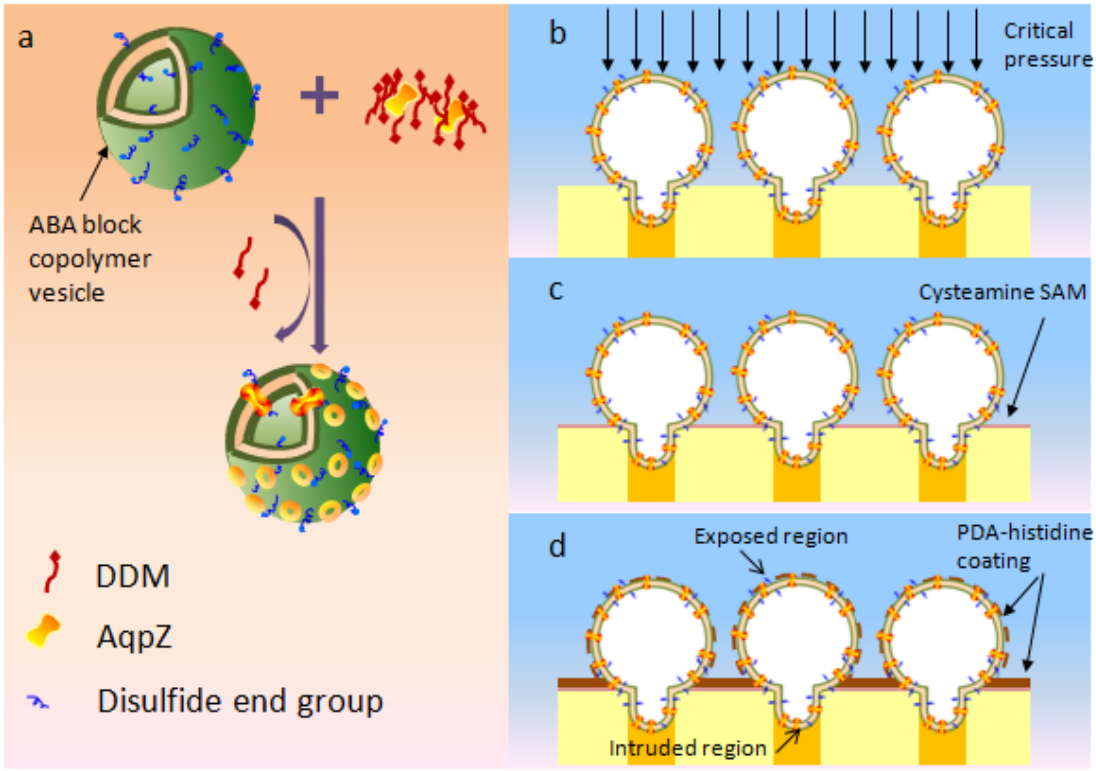

Scheme 4-1 Schematic diagram of AqpZ-embedded vesicular membrane design and synthesis route: (a) Reconstitution of AqpZ into vesicles formed from ABA block copolymer blends (DDM represents dodecyl- β-D-maltoside); (b) Pressure-assisted vesicle adsorption and immobilization; (c) Self-assembled monolayer of cysteamine on gold coating surface through chemisorption; (d) PDA and His alternative layer-by-layer coating on the top of the vesicular membrane.

4.2 Experimental Methods

4.2.1 ABA block copolymer vesicle preparation and AqpZ incorporation

AqpZ was prepared following the protocol described previously [111]. Vesicle suspension was prepared using the film rehydration method. The ABA block copolymer vesicles were prepared by blending (PMOXA-PDMS-PMOXA, Mn 1000-4000-1000) with acrylate ends, Polymer Source Inc. Canada) (9 mg) with (PMOXA-PDMS-PMOXA, Mn 1000-4000-1000) with disulfide ends (1 mg). The PMOXA-PDMS-PMOXA (Mn

1600-5500-1600) with disulfide ends was synthesized as described before with a polydispersity index (PDI) of 1.46 [112]. The AqpZ was incorporated into ABA vesicles by using the same protocol as described previously [111]. For stopped-flow analyses, vesicles were extruded 21 times using PCTE membranes (pore size: 100 nm). Another set of proteopolymersome solutions was extruded 21 times through the PCTE membrane (pore size: 200 nm) and was then used for vesicle immobilization experiments. Subsequently, these vesicle samples were subjected to UV-crosslinking for 15 min at 4 ºC. The samples for transmission electron microscopy (TEM) imaging were prepared from ultrapure water.

4.2.2 Stopped-flow analysis

The permeabilities assays of vesicles before and after UV-crosslinking were performed as described previously on a Chirascan Circular Dichroism Spectrometer (Applied Photophysics, UK) [111]. The permeability coefficients were calculated based on 3 measurements.

4.2.3 Preparation of layer-by-layer PDA coating on gold coated silicon wafers

The gold coated silicon wafers were immersed in a cysteamine solution (0.5mg/ml) and incubated for 10 h at 4 °C. The wafers were then dipped in a dopamine solution (0.2 mg/mL in 10 mM Tris-HCl buffer (pH 8.6)). The solution was continuously stirred for 3 h. Then, the wafers were rinsed by using DI water. Subsequently, the wafers were incubated in a His solution (0.2 mg/mL in 1×PBS buffer) and continuously stirred for 1 h. A series of wafers were prepared based on different coating cycles.

4.2.4 Preparation of vesicle immobilized biomimetic membranes

The PCTE membrane (pore size 50 nm, porosity ~20%) coated with a 50 nm gold layer by vapor deposition was mounted on a filter support that was connected to a vacuum pump. The UV-crosslinked vesicle solution was dropped onto the PCTE membrane surface under a respective vacuum of about 900-925 mbar that is the critical vesicle extrusion pressure [111]. The membrane was then incubated for 24 h at 4 °C. Sequentially, 20 µl of cysteamine solution (0.5mg/ml) was added to the membrane and incubated for 10 h at 4 °C. The membrane was then mounted at the bottom of a dead-end cylinder and a dopamine solution (0.2 mg/mL in 10 mM Tris-HCl buffer (pH 8.6)) was subsequently injected into the cylinder. The solution was continuously stirred for 3 h. Then, the solution in the dead-end cylinder was changed to a His solution (0.2 mg/ml in 1×PBS buffer) and continuously stirred for 1 h. A series of membranes were prepared based on different coating cycles.

4.2.5 Measurements of water flux and reverse salt flux in FO set-up

The AqpZ-ABA membrane was clamped in a membrane testing cell. The effective membrane area was standardized by covering the membrane with a piece of alumina tape with a 5 mm diameter hole in the center. The flow rate is 100 ml/min for both feed and draw solutions that flow co-currently through the membrane testing device in the cross-flow mode. Using ultrapure water as the feed and NaCl solution as the draw solution, the water flux and the reverse salt flux were measured and calculated (supporting information). The water and reverse salt fluxes were measured as an average over 20 min

after the system was run for 10 min. For comparison, additional FO tests were conducted by employing both commercially available HTI membranes (Hydration Technologies Inc.) and AqpZ embedded vesicular biomimetic membranes using 0.8 M sucrose as the draw solute and 6000 ppm NaCl solution as the feed. The water flux and salt rejection were obtained. The experiments were carried out using 3 different batches of membranes.

4.2.6 Measurements of pure water permeability and salt rejection

The pure water permeability and salt rejection were tested with the vesicular layer facing the feed at 1 bar of trans-membrane hydraulic pressure. For salt rejection, a 200 ppm NaCl solution was used.

4.3 Results and Discussion

4.3.1 Characterization of proteopolymersomes

The process of membrane synthesis shown in Scheme 1 is characterized step by step. The morphology of the vesicles, which are formed from the ABA block copolymer blends in 1× PBS buffer, are observed by transmission electron microscopy (TEM). Figure 4-1 shows representative TEM image of unilamellar vesicles after extruded through 200nm PCTE membrane. The physical dimensions of the vesicles were characterized by using dynamic light scattering (DLS). The average hydrodynamic diameter is approximately 212 nm with PDI of 0.16. Subsequently, UV irradiation is applied to these vesicles so that a cross-linked polymer network structure is expected to form (Figure 4-2) [113, 114].

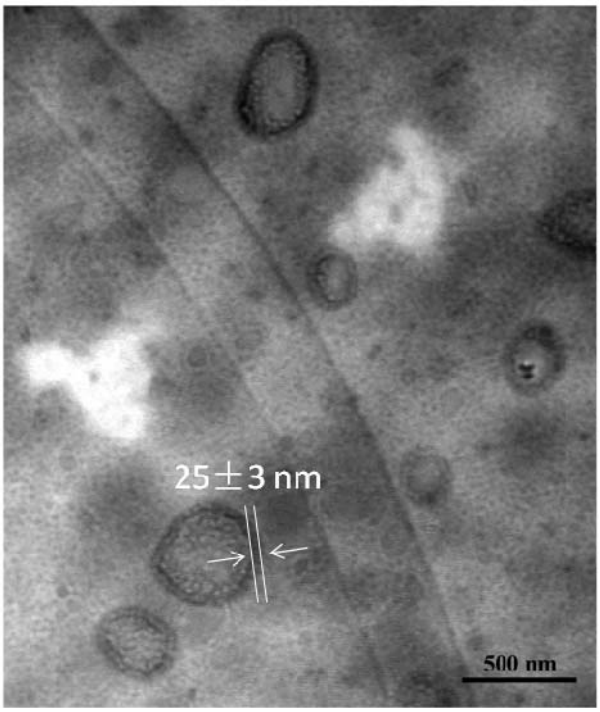

Figure 4-1 Transmission electron microscope (TEM) image of ABA block copolymer vesicles (after extrusion by a 200 nm PCTE membrane).

In Figure 4-2, before UV-crosslinking, the FTIR band at 1648 cm^{-1} is contributed by the presence of tertiary amide groups (1670-1630cm^{-1}) and alkene groups (1648-1615cm^{-1}) [115]. The pronounced band shifting to 1631 cm^{-1}, which represents the amide C=O bond from PMOXA, suggests that the unsaturated methacrylate groups have been converted to the saturated C-C bonds under UV-irradiation. Crosslinking also results in an increase of peak intensity at 850 cm^{-1} due to the formation of methylene bonds which are usually observed at 914 cm^{-1} [116].

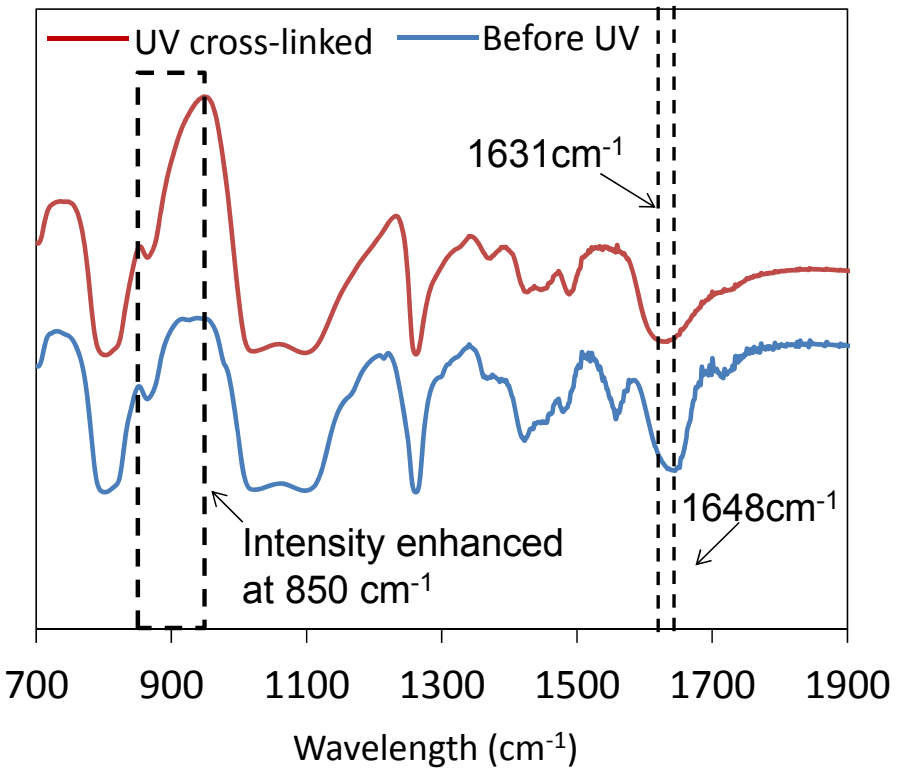

Figure 4-2 FTIR spectra of ABA polymersomes before and after UV-crosslinking.

4.3.2 Water permeability tests of vesicles

On the other hand, the permeability of the AqpZ-embedded vesicles has to be confirmed. The vesicles that are used for permeability tests are extruded by 100 nm PCTE membrane. The hydrodynamic diameters of the reconstituted proteopolymersomes and polymersomes are approximately 145±2 nm with PDI lower than 0.1. No obvious size variation can be observed on both proteopolymersomes and polymersomes after UV-crosslinking. The water transport through ABA polymersomes, AqpZ-ABA proteopolymersomes and the cross-linked vesicles was characterized by using a stopped-flow apparatus [18] and a hypertonic NaCl (Δosm = 1 osmol/L) solution (Figure 4-3). As shown in Figure 4-4, the permeability of AqpZ-ABA vesicles increases almost

proportionally to AqpZ-to-ABA molar ratio from 1:1600 to 1:400. A further increase in molar ratio leads to a decline in permeability. This phenomenon is consistent with the previous Aqp studies based on block copolymer and lipid vesicles [18, 37]. There are two possible causes for the up and down trend between permeability and AqpZ-to-ABA molar ratio. Firstly, the ABA membrane is exposed to more detergents as the AqpZ-to-ABA molar ratio is increased, which may be detrimental to AqpZ reconstitution efficiency [18]. Secondly, blending two PMOXA-PDMS-PMOXA copolymers with different molecular weights (1000-4000-1000 and 1600-5600-1600) exhibits a higher vesicle membrane thickness compared to solely using PMOXA-PDMS-PMOXA (1000-4000-1000) copolymer (25 nm vs. 8 nm) [61]. The dimensional mismatch between ABA copolymer and AqpZ may create a chemically unfavorable environment and hence inhibit the incorporation of more AqpZ proteins [61]. These reasons may also explain why the highest permeability occurring in the current system has a lower AqpZ-to-ABA molar ratio (1: 400) than the previous study (1: 100) [112]. In contrast, no observable permeability can be found for the ABA vesicles up to 10 s of monitoring (Figure 4-3f). Therefore, the fast water transport of proteopolymersomes is mainly contributed by AqpZ. Assuming AqpZ is totally incorporated into the ABA vesicles, there are 134 AqpZ monomers incorporated when the AqpZ-to-ABA molar ratio is 1/400. By taking the vesicle surface area into account, the water permeability of each AqpZ subunit is approximately $2.0\times10^{-13}cm^3/s$, which matches well the reported values [18, 37].

a

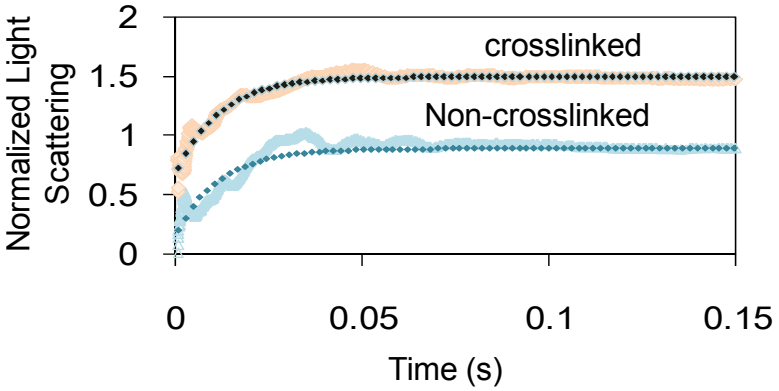
Normalized Light Scattering
2
1.5
1
0.5
0
crosslinked
Non-crosslinked
0
0.05
0.1
0.15
Time (s)

b

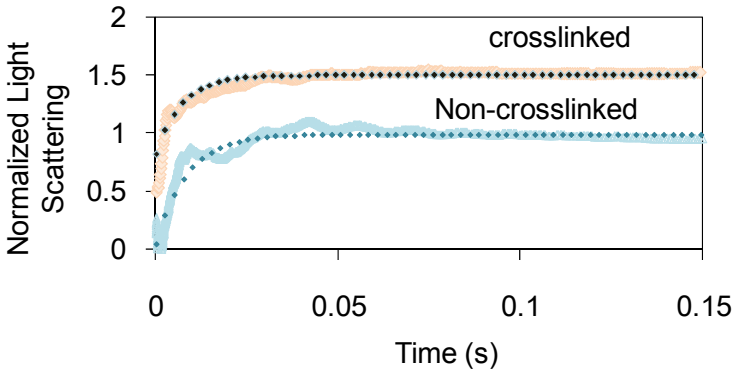
Normalized Light Scattering
2
1.5
1
0.5
0
crosslinked
Non-crosslinked
0
0.05
0.1
0.15
Time (s)

c

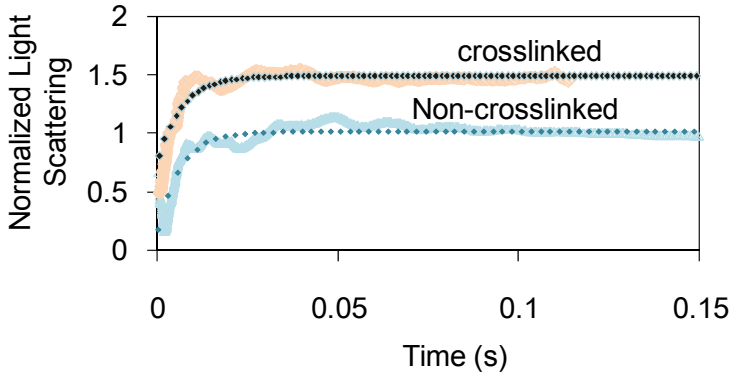
Normalized Light Scattering
2
1.5
1
0.5
0
crosslinked
Non-crosslinked
0
0.05
0.1
0.15
Time (s)

d

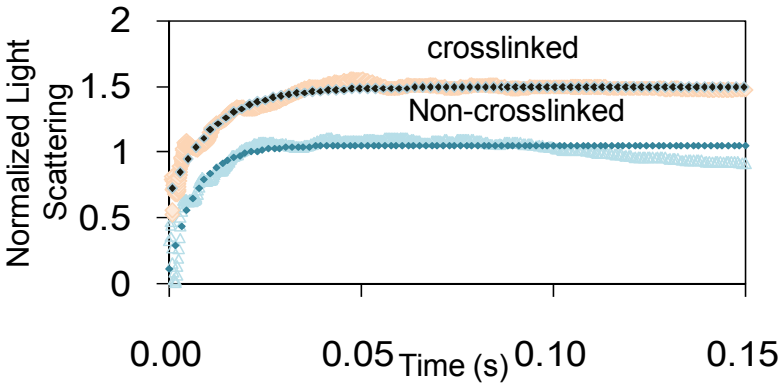
Normalized Light Scattering
2
1.5
1
0.5
0
crosslinked
Non-crosslinked
0.00
0.05
Time (s)
0.10
0.15

e

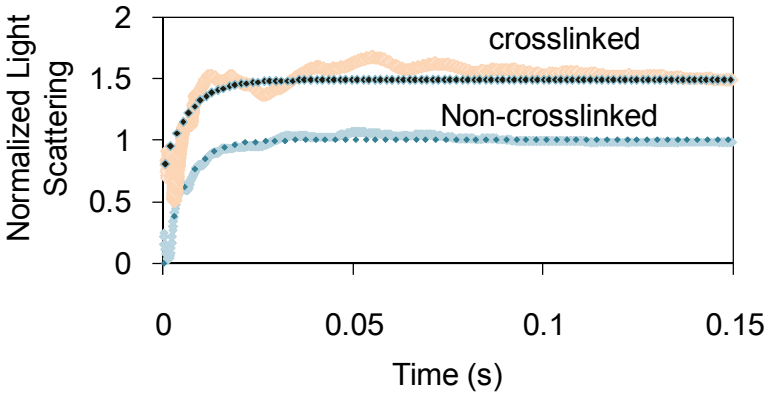
Normalized Light Scattering
2
1.5
1
0.5
0
crosslinked
Non-crosslinked
0
0.05
0.1
0.15
Time (s)

f

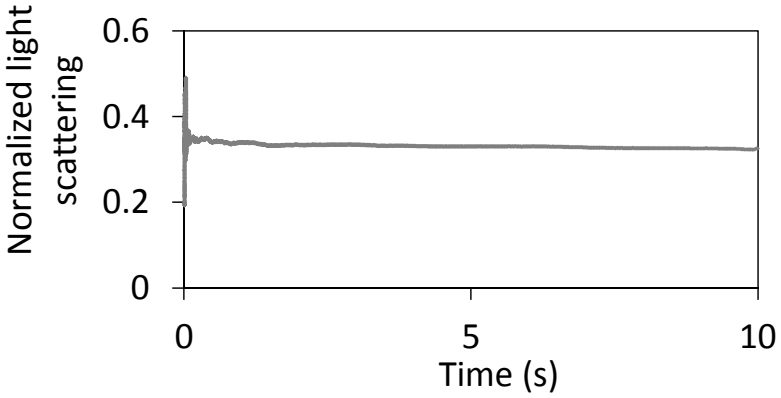
Normalized light scattering
0.6
0.4
0.2
0
0
5
10
Time (s)

Figure 4-3 Stopped-flow tests on UV-crosslinked and non-crosslinked vesicles of different AqpZ to ABA molar ratios. The signals have been normalized to fit between 0 and 1 except curve f. (f) is generated by offset an ambient value. Curves of crosslinked and non-crosslinked vesicles are offset for clarity. The dashed lines are signals and the solid lines are fitting curves. (a) to (e) corresponds to AqpZ to ABA molar ratios of 1: 1600, 1: 800, 1: 400, 1: 200 and 1: 100. (f) is the control sample (i.e. ABA block copolymer vesicles)

Figure 4-4 also shows the permeabilities of polymerized vesicles after cross-linking. At low AqpZ-to-ABA molar ratios, the permeabilities of the cross-linked vesicles are comparable to those of the non-cross-linked ones. However, when the AqpZ-to-ABA molar ratio is greater than 1/400, the permeability drops by approximately 10-18% after UV irradiation. This may be due to the fact that the block copolymers are held together by a cross-linked network after UV irradiation and the vesicle deformation response is thus delayed. Because the AqpZ-ABA vesicles with a molar ratio of 1/400 have the highest permeability, this molar ratio was chosen to prepare the biomimetic membrane for further studies.

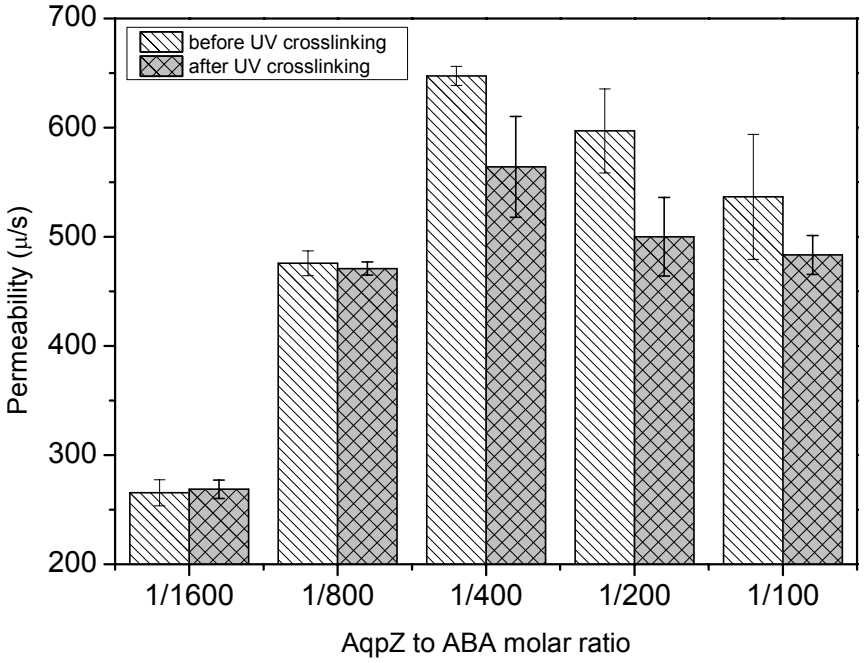

Figure 4-4 Comparison of permeabilities of proteopolymersomes before and after UV-crosslinking.

4.3.3 Optimization of layer-by-layer PDA coating

Another key step is optimizing the layer-by-layer PDA coating to stabilize the vesicles and eliminate the possible defects between the vesicles and the pores. Therefore, prior to building the thin film coating on the vesicle immobilized membrane, AFM was used to analyze the morphology of each coating layer. Three cycles of PDA coatings were applied. Between cycles, a His solution was applied to form favorable amine-dopamine and imidazole-dopamine covalent bonds between each layer [108, 109]. Figure 4-5b shows a significant adsorption of PDA molecules agglomerating on the gold surface after 3 h of coating as compared with Figure 4-5a. In contrast, cysteamine-functionalized gold surface (Figure 4-5c) exhibits a more homogeneous coating with very few PDA

agglomerates after 3h of coating (Figure 4-5d), which suggests that the monolayer of cysteamine facilitates more uniformly coating rather than random PDA adhesion. Figure 4-5d-f also displays that the net increment of root-mean-square roughness (Rm) of each coating cycle transitioning from approximately 0.6 nm to 0.4 nm and finally to 0.3 nm. The decrease in roughness increment per coating indicates that the fresh dopamine monomer, which is a small molecule (Molecular weight 153Da), may diffuse into the loosely-packed underlying PDA film. As a result, the inter-diffusion can alter film architecture by promoting the interaction between the fresh monomer and the PDA network, leading to a lower increase in film roughness.

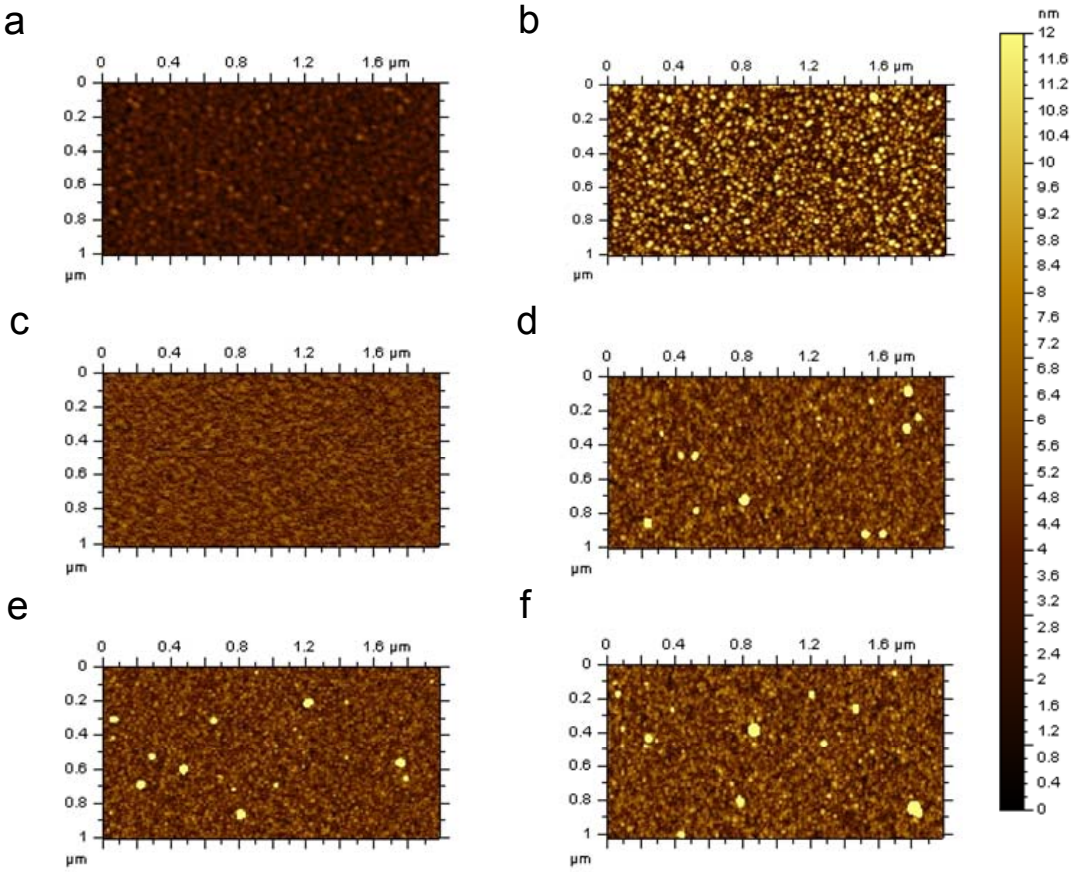

Figure 4-5 AFM images of PDA-His coatings on gold-coated silicon wafer. (a) Gold-coated silicon wafer (Rm=0.8 nm); (b) PDA polymer coating on the gold-coated silicon wafer without pre-adsorbed cysteamine (Rm=2.7 nm); (c) Gold surface coated with cysteamine (Rm=1.1 nm); (d) Gold surface coated with cysteamine -PDA 3h-His 1h (Rm=1.7 nm); (e) Gold surface coated with cysteamine-(PDA 3h-His 1h)$_2$ (Rm=2.1 nm); (f) Gold surface coated with cysteamine-(PDA 3h-His 1h)$_3$ (Rm=2.3 nm).

The effectiveness of different coating layers and the role of His on membrane performance were studied by FO. The membranes were measured using ultrapure water as the feed and NaCl solution (0.5 M) as the draw solution in the pressure retarded osmosis (PRO) mode, in which the vesicular layer faces the draw solution. Table 4-1 shows that the membrane exhibits a significantly lower salt reverse flux and that the water flux was improved with an increase in the number of PDA-coating layers. The membrane coating consisting of PDA and His provides sufficient salt rejection as compared with the one without His between two adjacent PDA layers. Additionally, the control sample (i.e., no embedded AqpZ proteins) does not exhibit any observable water flux in FO tests but does show a comparable salt reverse flux. Clearly, the PDA coating layer helps to seal the defects between the adsorbed vesicles and the membrane support. The coated membrane exhibit a little higher flux after each cycle of coating. The possible reason is that the decrease in reverse salt decrease may facilitate the forward flow of water by increasing the effective osmotic driving across the membranes.

Table 4-1 The effect of PDA coating cycles on the salt reverse fluxes and water fluxes of vesicular biomimetic membrane

Coating cycles*	Draw solution	Flux (L/m^2/h)	Salt reverse flux (g/m^2/h)
Cys-PDA3h -His1h	0.5M NaCl	21.1	38.1
Cys-(PDA3h-His1h)$_2$	0.5M NaCl	31.0	23.1
Cys-(PDA3h-His1h)$_3$	0.5M NaCl	43.6	8.9

Cys-$(PDA3h)_3$	0.5M NaCl	21.8	52.1

4.3.4 Morphology of vesicular biomimetic membrane

In order to confirm the homogeneous immobilization of the vesicles on the membrane surface, we took scanning electron microscopy (SEM) images of the plain membrane (Figure 4-6a), the control sample without vesicles but with 3-cycle PDA-His coatings (Figure 4-6b) and the 3-cycle PDA-His coated vesicular membrane (Figure 4-6c and 4-6d). Compared to Figure 4-6a and 4-6b shows that 3-cycle PDA-His coating is homogeneous and no big agglomerate is formed on the membrane surface. This suggests that the spheres in Figures 4-6c and 4-6d are immobilized vesicles rather than PDA agglomerates. Figures 4-6c and 4-6d also show that almost all the open pores of the PCTE membrane are covered by the vesicles. Furthermore, these vesicles retain their spherical structure and membrane integrity even after experiencing the vacuum drying process. This suggests that the PDA coating not only helps to stabilize the vesicles but also keeps them firmly attached to the substrate channels when the membrane experiences mechanical disturbance from surroundings.

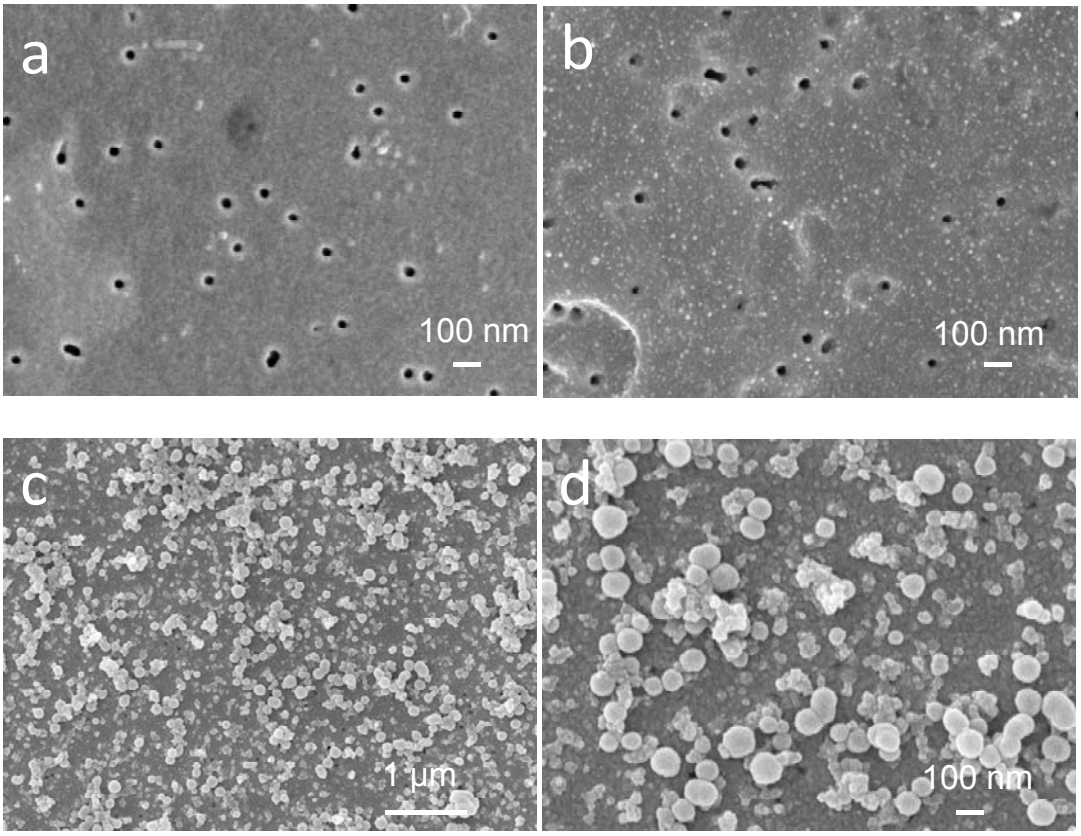

Figure 4-6 Membrane morphology and performance of biomimetic membrane: FESEM images of (a) gold-coated PCTE membrane with a self-assembled monolayer of cysteamine (pore size 50 nm); (b) PCTE membrane with 3-cycle coating of PDA 3h-His 1h on the top of chemisorbed cysteamine (control); (c) the vesicle immobilized PCTE membrane with 3-cycle coating of PDA 3h-His 1h on the top; (d) enlarged view of (c).

4.3.5 FO performance test

Having obtained vesicular membranes with optimized water permeability and salt retention, the membranes were investigated by using different draw and feed solutions. Figure 4-7 and Table 4-2 show the water fluxes and the reverse salt fluxes of the membranes that were subjected to both PRO-mode and FO-mode tests. As expected, the water flux increases almost proportionally with an increase in the draw solute (NaCl) concentration. The salt reverse fluxes are minimized to an insignificant level, which are

comparable with those of current state-of-the-art polymeric membranes [95]. Interestingly, the water flux in the PRO mode is only slightly greater than that in the FO mode. This phenomenon implies that internal concentration polarization is not severe, most likely because the substrate is thin (5 μm) and has straight channels. Comparing this membrane to the previously developed pore-spanning membrane with the same AqpZ-to-ABA molar ratio (1/400), the water flux is greatly improved from 18.2 to 43.6 L/m^2/h under the PRO mode using 0.5 M NaCl as the draw solute [111]. The improvement may be due to the fact that we previously employed the vesicle rupture and fusion processes to form pore-spanning biomimetic membranes. Such processes may denature AqpZ and result in a much lower water flux than that theoretically predicted. A membrane with a layer of large unilamellar vesicles offers a more natural environment with fewer effects inhibiting AqpZ function. In addition, the current vesicular membrane provides sufficient mechanical strength to withstand tangential flow during FO tests. As shown in Figure 4-8, all the vesicles maintain their spherical shape after the FO test. For comparison, both a commercially available HTI membrane and the newly synthesized vesicular biomimetic membrane were tested using 6000 ppm NaCl as the feed solution and 0.8 M sucrose as the draw solution under the PRO-mode. The HTI membrane shows a considerably lower flux (1.26 L/m^2/h) but a remarkably high salt retention (92.3%). In contrast, the biomimetic membrane shows an order-of-magnitude increase in water flux (17.6 L/m^2/h) with comparable salt retention (91.8%). As the membrane was tested at 1 bar, the AqpZ-embedded membrane shows a PWP of 4.3 L/m^2/h/bar and 65.8% rejection towards NaCl. In contrast, the control sample shows a PWP of 0.2 L/m^2/h/bar and 68.6% rejection. The derivation of salt rejection values in different testing modes (91.8% vs. 65.8%) suggests

that this membrane may be subjected to deformation under hydraulic pressure. According to our previous study, vesicles that were suspended in solutions can be extruded through 50 nm pores under a hydraulic pressure less than 1 bar [18]. Even though the vesicles are immobilized and coated with PDA in the current study, it seems that the pore size of the PCTE support is the dominant factor for hydraulic pressure resistance. Therefore, to further enhance the mechanical stability of the membrane, a substrate with a smaller pore size will be recommended.

It should be noted that the membrane surface is very rough due to vesicle immobilization. Water has to transport twice through the biomimetic layer. Therefore, the water flux is only the apparent water flux. It is related to the intrinsic vesicle permeability, area ratios of the immobilized vesicle (exposed region and intruded region in Scheme 1), porosity of the support, vesicle size and the encapsulated salts. The actual open area of the biomimetic membrane can be characterized by mathematically modeling, which will be covered in our future publications.

Table 4-2 Reverse salt flux as a function of draw solution concentration in both FO and PRO modes

Draw solute concentration (M)	Salt reverse flux (g m^{-2} h^{-1})			
	AqpZ-ABA (molar ratio:1/400)		Control	
	FO	PRO	FO	PRO
0.4	1.4 ±0.5	5.2 ±1.2	2.0 ±0.3	5.7 ±0.8
0.5	2.1 ±0.7	7.1 ±1.5	2.6±0.2	6.2 ±0.4
0.6	2.7 ±0.5	7.4 ±0.9	2.7 ±0.4	6.9 ±0.9
0.7	3.5 ±0.4	8.3 ±1.1	3.3 ±0.9	7.8 ±0.6

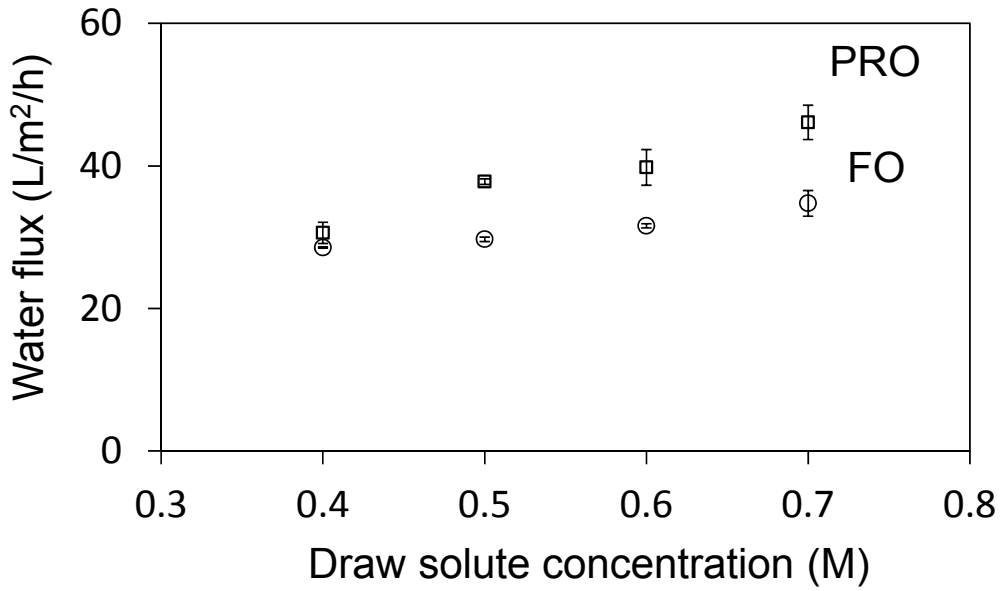

Figure 4-7 FO performance of vesicular biomimetic membrane with the coating layer $(PDA3h\text{-}His1h)_3$ using NaCl as draw solute and water as feed.

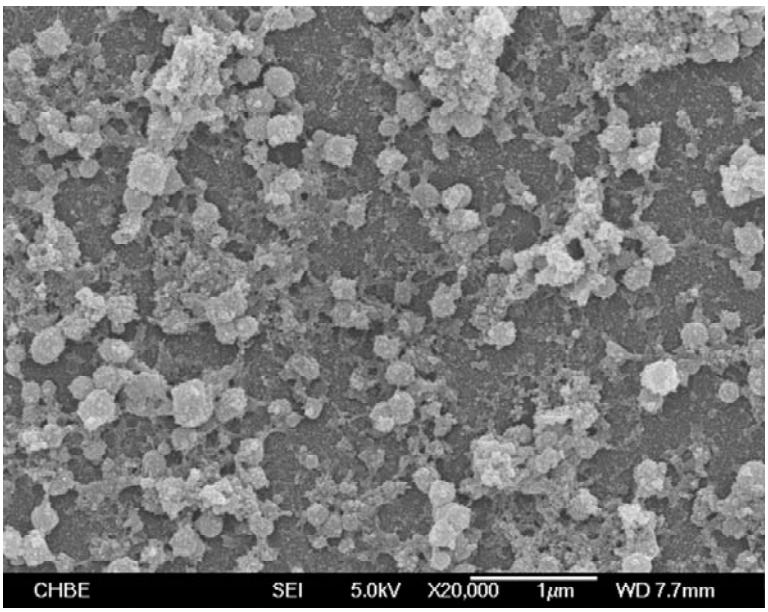

Figure 4-8 FESEM image of vesicular biomimetic membrane after the FO test

4.4 Conclusions

The proposed vesicular membrane design has been realized via an effective synthesis route. As compared with polymer membranes and the previous pore-spanning biomimetic membrane, such a vesicular membrane can achieve a higher water throughput using a lower driving force; thus, it could provide an effective way of saving energy in water reuse and desalination. It can be envisioned that the performance of vesicular biomimetic membranes is mainly circumscribed by selective layer properties, such as vesicle size, vesicle permeability and coverage of the vesicles on the support. The interior solute concentration of vesicles which is a relatively stagnant layer may the rate of water transport. Further improvements in membrane performance and long term permeability test will be needed to be addressed in future development of biomimetic membrane.

CHAPTER 5: Mechanically robust and highly permeable Aquaporin Z biomimetic membranes (II)

5.1 Introduction

Despite the advantage of AqpZ, to functionally reconstitute AqpZ into a stable synthetic membrane for industrial applications is crucial. In 2007, Kumar and his colleagues have verified the potential capability of AqpZ in desalination by incorporating AqpZ into ABA symmetric $PMOXA_{15}$-$PDMS_{110}$-$PMOXA_{15}$ block copolymer vesicles [18]. The AqpZ-ABA vesicles have shown to selectively conduct water at high flow rates. Later, several designs, such as pore-spanning biomimetic membranes and hydrophilic-supported pore-spanning membranes have also been proposed and fabricated, but no study was given to examine the function of incorporated Aqps in these designs [76]. In 2012, Wang and Chung et al demonstrated that the AqpZ-embedded biomimetic membrane exhibited high water flux and rejection to NaCl [111]. Nevertheless, the mechanical properties of such membranes may be a concern for further application. Altogether, Aqp-embedded membranes have not been achieved at a scale applicable for water reuse. A new design is needed urgently to enhance the mechanical stability.

One robust design is to use Aquaporin-embedded vesicles directly as the selective layer. Such design concept has been explored previously. As shown in Scheme 5-1, the UV-crosslinked AqpZ-ABA block copolymer vesicles are immobilized on the membrane support and further stabilized by a layer-by-layer polydopamine (PDA) coating. The resultant membrane has demonstrated high water permeability and good salt rejection properties in a dynamic FO operation. Such membrane exhibits high potential in a real

application. However, a fundamental understanding of the water transport through the Aqp-embedded vesicular biomimetic membrane will be critical to guide future membrane design. Therefore, this work is a continuous study based on the previous experimental results, so as to optimize the membrane design and fabrication. Specifically, we systematically investigate the influence of vesicle properties, such as vesicle structure, vesicle permeability and encapsulated solutes within the interior of the vesicle on water flux.

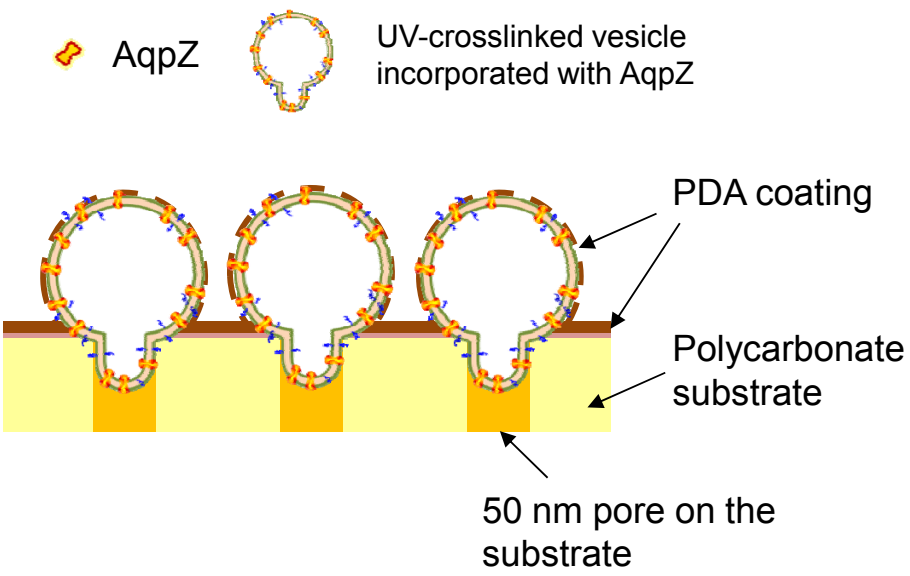

Scheme 5-1 Schematic diagrams of vesicular membrane design

5.2 Theory

In Scheme 5-2, a vesicular biomimetic membrane separates two compartments containing NaCl solution and water, respectively. The vesicle is modeled as being partially intruded into the track-etched membrane channel, as illustrated in the previous study [111]. The vesicle's surface is thus divided into three distinct regions (Scheme 5-2a). The intruded

region bathed by the solution from compartment 1 has an area of A_1. The non-intruded region, which is bathed by the solution from compartment 2 and is able to transport water, has a surface area of A_2. The impermeable region where vesicle surface contacts with the PDA layer or channel wall of the substrate has a surface area of A_3. Except A_3, both of A_1 and A_2 regions are water permeable. In all cases, AqpZ molecules are assumed to be distributed uniformly over the surface of the vesicle.

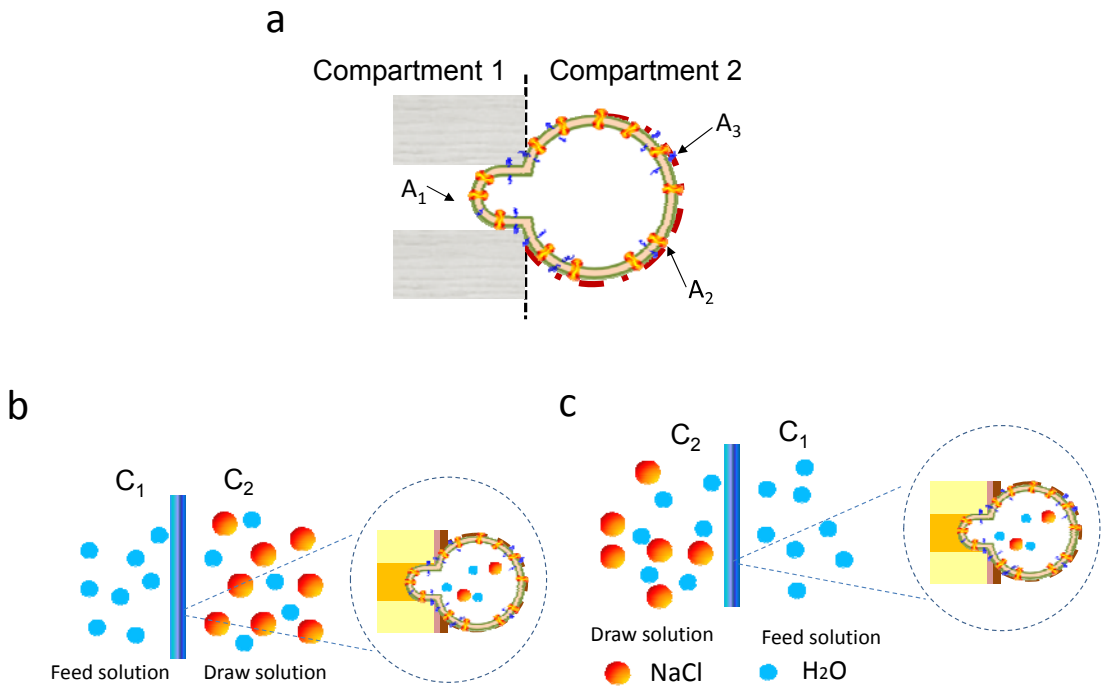

Scheme 5-2 (a) membrane regions and compartments defined for a vesicular biomimetic membrane; (b) pressure retarded osmosis (PRO) testing mode; (c) forward osmosis (FO) testing mode. C_1 and C_2 represent concentration of NaCl in compartments 1 and 2 respectively.

We assume that the vesicle initially has neither an intravesicular hydrostatic pressure nor any tension on its membrane [117]. Since NaCl is impermeable to vesicle [18], we assume only water flows through the vesicle membrane via AqpZ facilitated transport. According to the Kedem-Katchalsky equation for water volumetric flow, the driving

forces are the differences in osmotic and hydrostatic pressure across the membrane [118]. The accumulative flow of water into the vesicle can be described by [119]:

$$\vec{J}_v = L_2\left[RT\sigma\lambda\left(C_v(t) - C_2\right) - \Delta P\right] + L_1\left[RT\sigma\lambda\left(C_v(t) - C_1\right) - \Delta P\right] = -J_{v,out} + J_{v,in} \qquad (5\text{-}1)$$

where σ is the reflection coefficient and is assumed to be 1. λ is the molecularity. In the case of NaCl, λ=2. ΔP is the hydrostatic pressure difference between the inside of the vesicle and the outside solution. $C_v(t)$ is the NaCl concentration inside the vesicle. C_1 and C_2 are the concentrations of NaCl near the surface of the vesicular membrane in compartments 1 and 2, respectively. R and T are gas constant and temperature, respectively. $J_{v,in}$ and $J_{v,out}$ are the absolute values of water flow in and out of the vesicles, respectively. $L_{i(i=1,2)}$ is the hydraulic permeability coefficient of the membrane region in the ith compartment and can be calculated by [120]:

$$L_i = \frac{P_f a_i A_T V_w}{RT} \qquad (i=1,2) \qquad (5\text{-}2)$$

where $a_i = A_i/A_T$, A_T is the total surface area of the vesicle, V_w is the partial molar volume of water and P_f is obtained from Equation (5-2). Even though the PBS buffer is a mixture of several kinds of solutes, but the calculation in the model only considers NaCl due to the fact that it is the dominant solute.

There are two FO operation modes: namely pressure-retarded osmosis (PRO) mode and FO mode. In the PRO mode, the vesicular layer faces the draw solution, while FO mode is the opposite (Scheme 5-2b and 5-2c). Under our operation conditions, the vesicles will shrink in PRO mode, so ΔP is equal to 0 and $C_v(t)$ varies with time before reaching steady

state. Since AqpZ and the vesicle are impermeable to NaCl, the variation of NaCl concentration in the vesicle may be expressed as follows:

$$C_v(t) = \frac{n_0}{V(t)} \tag{5-3}$$

where n_0 is the total mole of NaCl initially inside the vesicle. $V(t)$ is the vesicle volume and may be estimated by:

$$V(t) = V_0 + \sum_{i=1}^{n} \vec{J}_v(i)\,\Delta t \tag{5-4}$$

where V_0 is the initial vesicle volume, Δt is the time interval and $\vec{J}_v(i)$ is the water volume flux evaluated at the start of the i-th time interval. $\vec{J}_v$ is close to 0 when the system reaches steady state. The net steady state water flux J_{vs} is obtained by using equation (5-5):

$$J_{vs} = -L_2\left[2RT\left(C_v(t) - C_2\right) - \Delta P\right] = L_1\left[2RT\left(C_v(t) - C_1\right) - \Delta P\right] \tag{5-5}$$

In the PRO mode, internal concentration polarization (ICP) may be ignored due to the fact that pure water is used as the feed, while external concentration polarization (ECP) must be considered. Hence, C_1=0 while C_2 is estimated to be 45% of the bulk concentration of NaCl in compartment 2 (C_{2b}) according to the experimental conditions [12, 120]. Meanwhile, the concentration polarization effects inside the vesicles are neglected.

The net steady state water flux J_{vs} is calculated based on one vesicle. For a piece of membrane, the steady state water flux, J_m, can be calculated by taking into account the number of vesicles N_v that have been immobilized on the pores.

$$J_m = J_{vs} N_v \tag{5-6}$$

Assuming that each pore is covered by one vesicle, the number of vesicles N_v is calculated by using equation (5-7).

$$N_v = \frac{A_m \varepsilon}{A_p} \tag{5-7}$$

where A_m *is* the area of the membrane (19.6 mm^2). A_p is the area of a single pore (1.96×10^{-9} mm^2), which is estimated according to the pore size of 50 nm. ε is the porosity of membrane, which is 20%. Therefore, the number of pores is estimated to be 2×10^9.

5.3 Results and Discussion

5.3.1 Mechanism of water transport through the vesicular membrane

Driven by osmotic pressure, water molecules are first transported into the vesicles from the feed solution and then out of the vesicles to the draw solution. In the PRO mode, the majority of the vesicular membrane (A_2) faces the draw solution. Presumably, vesicles are initially at their full volume (*t=0*). When the osmoticant (NaCl) solution is added to compartment 2, vesicles start to shrink because the flow outwards is faster than the inward flow. The salt concentration inside the vesicle increases until a steady state is reached. We can measure the steady-state water flux (J_m) through experiments. As shown in Table 5-1, the experimental results suggest that the vesicle intrinsic properties such as vesicle permeability, encapsulated salt concentration and vesicle size can possibly influence the steady-state water flux (Table 5-1) in the PRO mode. Based on the known parameters, MATLAB was used to solve equations (5-1)-(5-4) for membrane area fractions a_1 and a_2, which are estimated to be 0.22 and 0.75, respectively. As shown in

Figure 5-1, the majority of predicted data match well with the experimental data in three different cases. The minor derivation between the experimental data and the predicted may be due to the polydispersity of vesicle size, which has not been considered in this model. It is worth noting that the sum of total area fraction is less than 1, because of the existence of the contact region through which water is less likely to permeate (Scheme 5-2a). In addition, the PDA coating layer may also block part of the vesicle surface.

Table 5-1 The steady state water fluxes measured using a series of AqpZ-embedded vesicular biomimetic membranes under different driving forces in the PRO mode

AqpZ to ABA ratio	Vesicle radius (nm)	Draw solution (M)	Feed solution	Initial concentration in vesicle ($\times 10^{-3}$M)	Permeability (μm/s)	Water flux (L/m^2/h)
1/400	99	0.4	0	137	564	30.6
1/400	102	0.5	0	137	564	37.8
1/400	98	0.6	0	137	564	43.6
1/400	97	0.7	0	137	564	46.1
1/400	102	0.4	0	68.5	517	36.6
1/400	103	0.5	0	68.5	517	40.9
1/400	104	0.6	0	68.5	517	44.0
1/400	106	0.7	0	68.5	517	49.9
1/800	96	0.5	0	68.5	470	21.1
1/1600	96	0.5	0	68.5	269	7.9

a

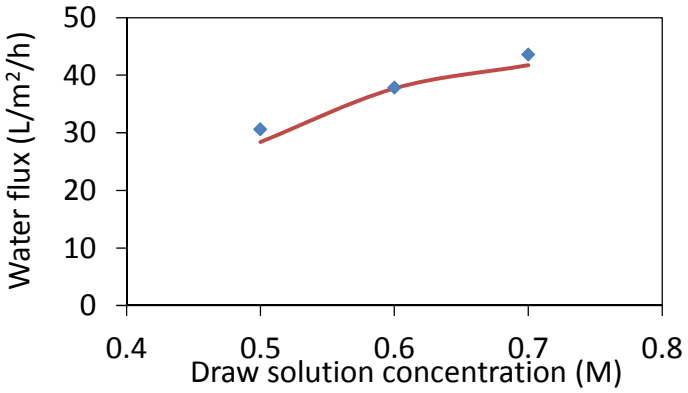
Water flux (L/m²/h)
50
40
30
20
10
0
0.4
0.5
0.6
0.7
0.8
Draw solution concentration (M)

b

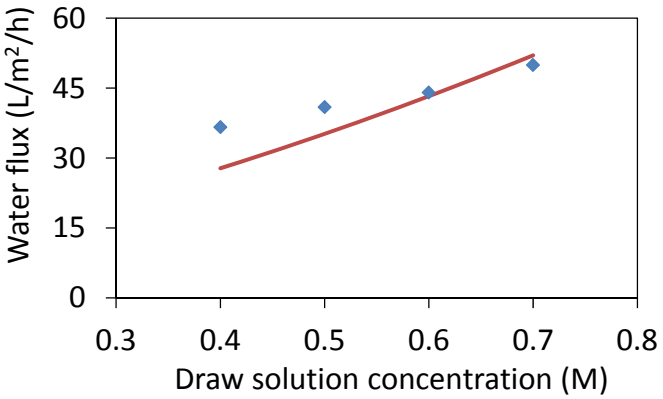
Water flux (L/m²/h)
60
45
30
15
0
0.3
0.4
0.5
0.6
0.7
0.8
Draw solution concentration (M)

c

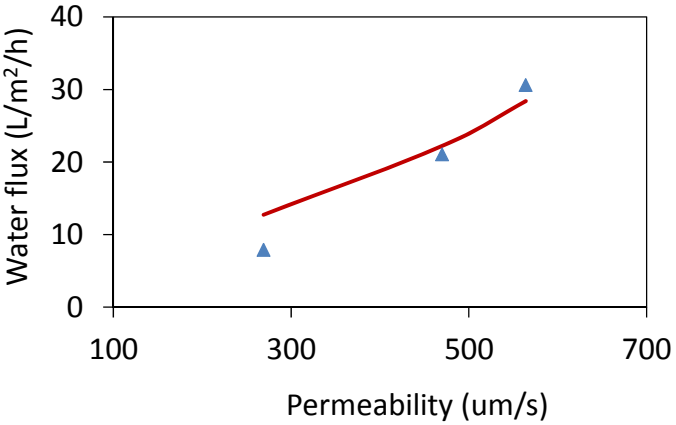
Water flux (L/m²/h)
40
30
20
10
0
100
300
500
700
Permeability (um/s)

Figure 5-1 Experimental vs. modeling predicted water fluxes of vesicular biomimetic membranes using NaCl as the draw solute and water as the feed in the PRO mode: (a) The draw solution concentration varies from 0.4 to 0.7 M by fixing P_f= 564 μm/s and C_{v0}=0.137 M; (b) The draw solution concentration varies from 0.4 to 0.7 M by fixing P_f= 517 μm/s and C_{v0}=0.0685 M; (c) The permeability varies from 269 to 564μm/s by fixing $C_{2,b}$=0.4 M and C_{v0}=0.137 M.

Since we have determined the structure parameters (a_1 and a_2), we are able to isolate the contribution of each vesicle intrinsic property to water flux by considering three hypothetical scenarios using equations (5-1)-(5-4). Overall, the steady-state water fluxes and the evolutions of vesicle shrinkage were investigated by varying one vesicle property while fixing the other two. Figure 5-2 shows the results that are calculated by assuming water as feed (C_1=0) and 0.6 M NaCl as draw solution ($C_{2,b}$=0.6). The water fluxes increase with the increase of either vesicle permeability (Figure 5-2a) or vesicle size (Figure 5-2c), but remain constant while changing NaCl concentration inside the vesicles (Figure 5-2e). According to Equation (5-5), the steady-state water flux is determined by both the permeability coefficient and the driving force. Figure 5-2b shows that the final volume shrinkages of the vesicle and the equilibrium solute concentration C_v are invariant with an increase in vesicle permeability, suggesting that the net osmotic driving forces are the same. Therefore, the increase of steady-state water flux is mainly due to the increase of permeability coefficients (L_1 and L_2), according to Equation (5-2). For the same reason, the water flux also increases with the vesicle radius. In addition, when we either increase vesicle size or decrease vesicle permeability, both the shrinking rate of vesicle and the variation rate of solute concentration become much slower (Figures 5-2b and 5-2d). Based on the simulation results, vesicles with different interior solute concentrations reach steady-state approximately within the same amount of time and

achieve the same level of equilibrium C_v (Figure 5-2f). Because neither the permeability coefficient nor the driving force varies with the initial solute concentration inside the vesicle, the steady state water fluxes are kept constant (Figure 5-2c). In this case, one can observe that the only benefit of a higher interior solute concentration (C_v) is a less volume shrinkage in vesicles. For example, if a 1.25×PBS buffer is encapsulated into the vesicle instead of a 0.75×PBS buffer, the net volume shrinkage drops proportionally from 82% to 49%.

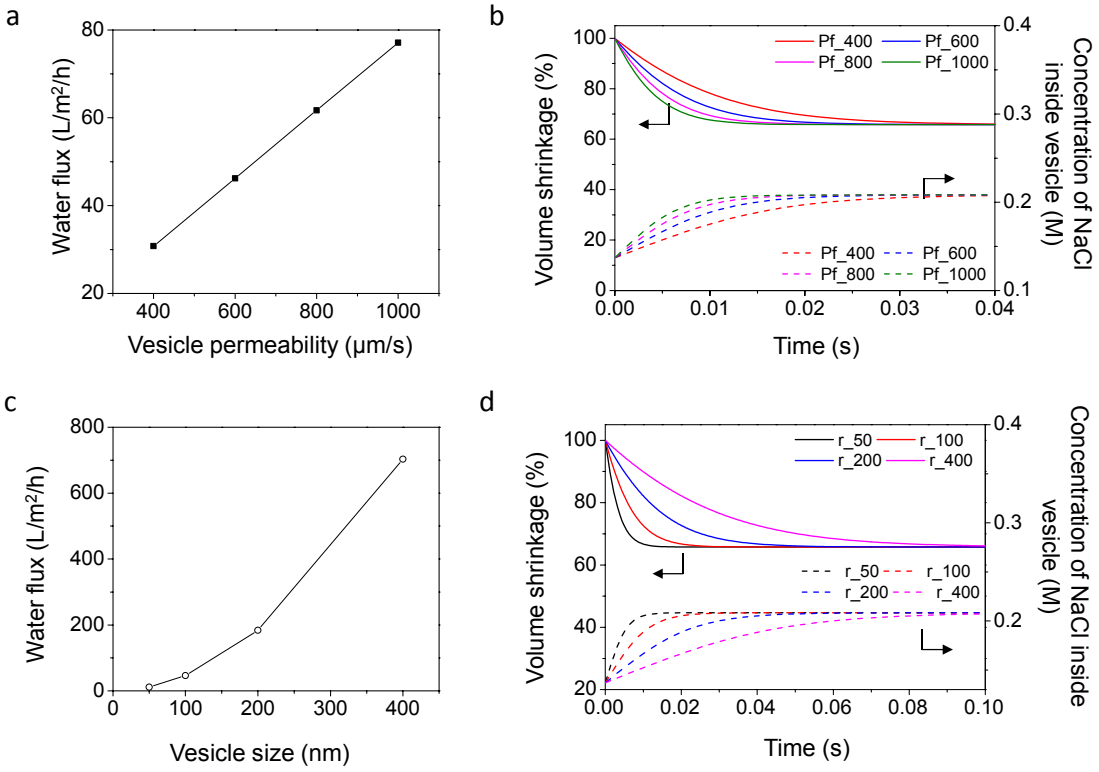

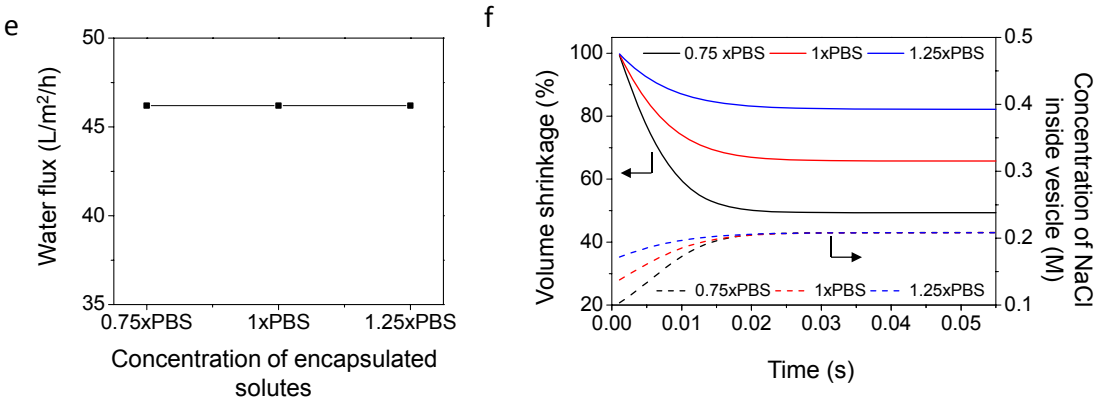

Figure 5-2 The steady-state water fluxes and the corresponding evolutions of vesicle shrinking for different vesicular membranes in the PRO mode: (a and b) effect of vesicle permeability, which varies from 400 to 1000 μm/s by fixing $C_{2,b}$=0.6 M, radius=100nm and C_{v0}=0.137 M; (c and d) effect of vesicle size which varies from 50 to 400 nm by fixing P_f= 600 μm/s, $C_{2,b}$=0.6 M and C_{v0}=0.137 M; (e and f) effect of salt concentration encapsulated inside vesicles which varies from 0.75×PBS to 1.25×PBS by fixing P_f= 600 μm/s, $C_{2,b}$=0.6 M and radius=100nm.

To potentially optimize the water transport property of AqpZ in biomimetic membranes, Figure 5-3 maps the projected water flux as a function of vesicle size and permeability using 0.6 M NaCl as draw solution and water as feed in the PRO mode. Water flux increases with increasing vesicle size and permeability. For industrial applications, the water flux can be achieved by different combinations of vesicle size and permeability. For example, if our targeted water flux is 150 L/m^2/h, it can be achieved by using 100 nm vesicles with a water permeability of 950 μm/s, or alternatively, by using 180 nm vesicles and a permeability of 600 μm/s. Our current operation region is shown in the white box. To further enhance the performance, additional research will be needed to prepare AqpZ-embedded giant unilamellar vesicles [18] or choose better blends of ABA block copolymers so as to increase the AqpZ incorporation ratio and ultimately increase the vesicle permeability.

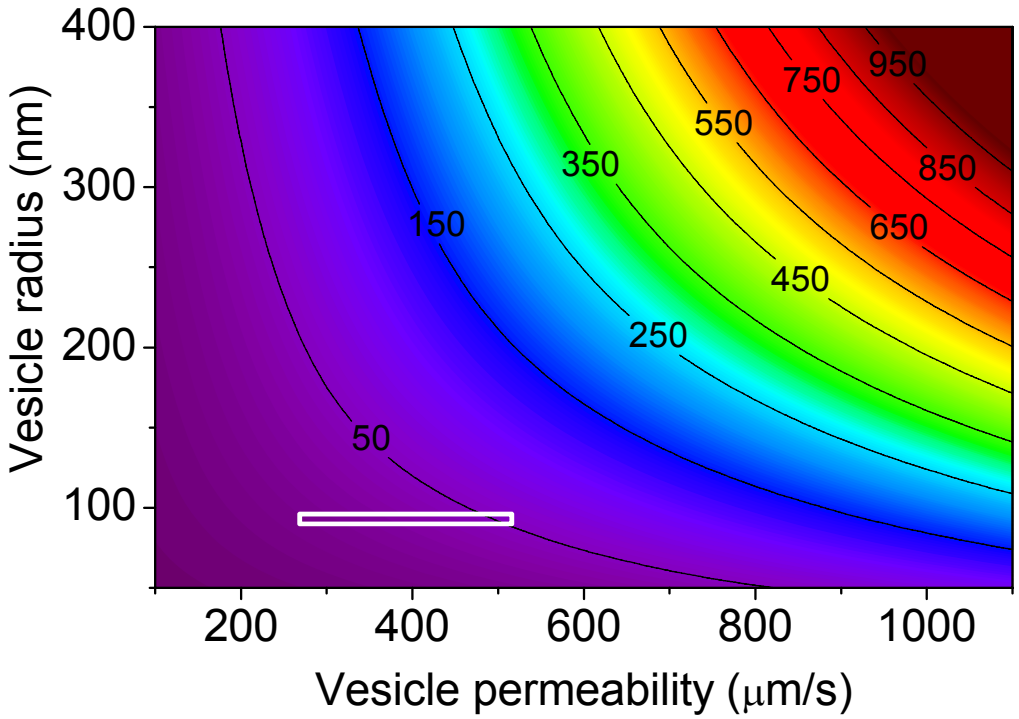

Figure 5-3 Contour map of the projected water flux as a function of vesicle size and permeability in the PRO mode (Draw solution: 0.6M NaCl, feed: water). The white box represents the current operating region.

5.3.2 Calculation of membrane hydrostatic pressure

In the FO mode, the minority of the vesicular membrane (A_1) faces the draw solution. When the osmoticant (NaCl) is added, the water flow into vesicles from the feed is greater than the water flow out of vesicles into the draw solution. Hence, vesicles tend to expand. However, assuming that the vesicles will not swell due to crosslinking and PDA coating, there should be a balance between inward and outward flows. Consequently, a hydrostatic pressure ΔP is developed to avoid excess water accumulation in vesicles by driving water efflux to balance with water influx, i.e. J_v is 0. Owing to the negligible

volume change of vesicle, the interior salt concentration, C_v, remains constant. The flux equations are then solved for the hydrostatic pressure by rearranging equation (5-1) with the aid of equation (5-5) as follows:

$$\Delta P = \frac{2RT\left[L_2\left(C_v(t)-C_2\right)+L_1\left(C_v(t)-C_1\right)\right]}{L_1+L_2}$$
$$= 2RT\left(C_v(t)-C_1\right)-\frac{J_{v,out}}{L_1} = 2RT\left(C_v(t)-C_2\right)+\frac{J_{v,in}}{L_2} \quad (5\text{-}8)$$

Both $J_{v,in}$ and $J_{v,out}$ have the same value as J_{vs} at equilibrium. Due to the dilutive internal concentration polarization effect, there is a derivation of C_1 from the bulk concentration [12, 120]. Thus, ΔP is estimated from the last equation, in which C_2=0.

The vesicles seem remarkably resistant to hypotonic shock. In Figure 5-4, the highest hydrostatic pressure that a vesicle can tolerate is 4.7 atm, which is estimated from the steady-state water flux under the FO mode using equation (5-8). As shown in our previous study, the immobilized vesicles maintain spherical morphology after the FO tests, indicating that the vesicles are effectively crosslinked and mechanically stable. Theoretically, the vesicle with a higher concentration of interior solute will be subjected to a higher hydrostatic pressure in the FO mode tests, which can also be observed from our calculation in Figure 5-4. Therefore, while a high interior solute concentration of the vesicle may provide a mechanical benefit for membrane in PRO mode operation, it could also have an adverse effect on the membrane stability in FO mode.

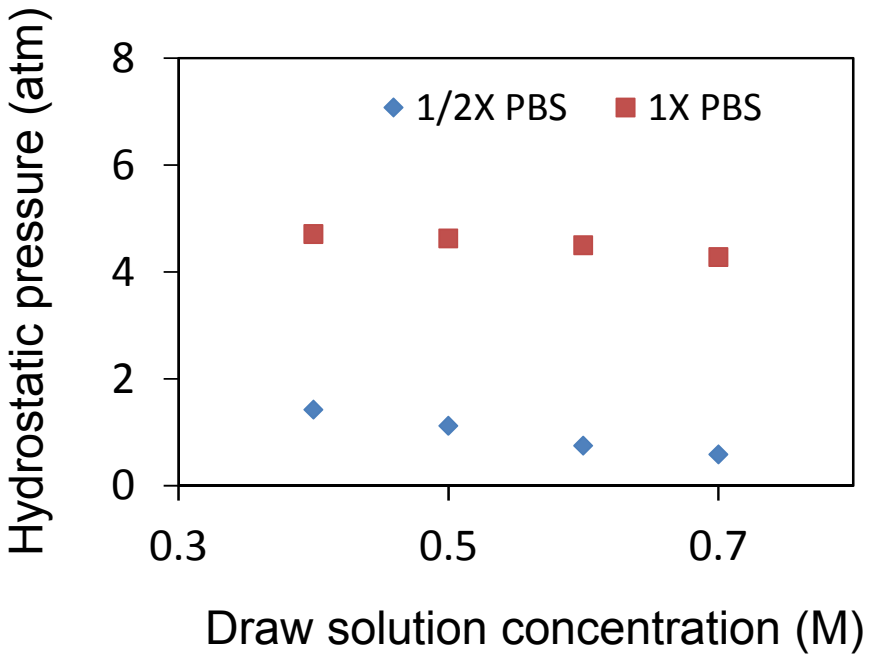

Figure 5-4 The hydrostatic pressure estimated from performance tests in the FO mode.

5.4 Conclusions

In conclusion, according to the mathematically modeling, the performance of vesicular biomimetic membranes is mainly circumscribed by the selective layer properties, such as vesicle size and permeability. The interior solute concentration of vesicles will mainly impact the mechanical stability of the vesicles. The FO performance of the membrane can be further enhanced via increasing either vesicle permeability or vesicle size, or both simultaneously.

CHAPTER 6: Conclusions and Recommendations

6.1 Conclusions

The development of biomimetic membrane embedded with AqpZ for water reuse is of crucial importance and challenging. In this study, a series of biomimetic membranes have been designed and implemented. The water permeability, salt reverse fluxes and water transport mechanism of the biomimetic membrane have been explored in forward osmosis. In order to enhance the mechanical stability, a vesicular biomimetic membrane has been further developed. Based on the studies above, the following conclusion can be drawn.

6.1.1 Preparation and characterization of pore-spanning biomimetic membranes embedded with AquaporinZ on carboxylated polyethylene glycol polymer cushion

This study explores the formation of two pore-spanning biomimetic membranes and the role of PEG cushion in this process. The interfacial interaction between the DMPC-AqpZ membrane and the support are discussed in terms of local mechanical stability. The reconstituted AqpZ molecules are proved to be functional by using the stopped-flow technique. The AqpZ-DMPC vesicles exhibit 2500-fold greater permeability than the pristine DMPC vesicles. The planar pore-spanning biomimetic membranes can be formed by spreading DMPC-AqpZ vesicles on porous alumina substrate. The smoothness of the substrate surface as well as the interfacial interaction between the biomimetic membrane

and the porous support have dominant effects on the coverage of the membrane. The reconstitution of AqpZ in a pore-spanning planar membrane increases the local mechanical stability of the biomimetic membrane but decreases the flexibility. On the other hand, the carboxylated-PEG cushion can improve the flexibility of the membrane.

6.1.2 Highly permeable and selective pore-spanning biomimetic membrane embedded with AquaporinZ

A new synthesis route of biomimetic membrane has been designed and implemented. The combination of surface modification, followed by pressure-assisted vesicle adsorption and then covalent conjugation-driven vesicle rupture and fusion are important means to incorporate AqpZ into the amphiphilic matrix and to deposit an ultrathin ABA-AqpZ membrane onto the porous support, with insignificant defects. The well-controlled pressure-assisted vesicle adsorption enhanced the surface coverage of the biomimetic membrane on the porous support. The subsequent vesicle rupture and fusion is driven by the covalent binding between the amphiphilic matrix and the porous support. The UV irradiation forms a polymer network among the amphiphilic polymer matrix, which largely enhances the mechanical stability of pore-spanning layer. The resulting membrane exhibits high water flux and high salt rejection, demonstrating itself capable of water purification in FO process.

6.1.3 Mechanically robust and highly permeable AquaporinZ biomimetic membranes (I)

Creating a robust and highly permeable yet selective membrane has been a focus of research worldwide. In this study, a vesicular biomimetic structure has been proposed, in order to further enhance the mechanical stability of the membrane. To incorporate the unique properties of AqpZ into biomimetic membranes with enhanced mechanical strength, we have designed a robust vesicular biomimetic membrane. The key step in the membrane synthesis is the application of PDA as a "bioglue". The resulting membrane exhibits great potential for water purification, because it can sustain mechanical disturbance from the surroundings. The water transport of such membranes is mediated by AqpZ water channels but not by the solution-diffusion mechanism. Thus, the vesicular membrane design may provide new possibilities to promote Aqp-embedded biomimetic membranes to industrial application. Further improvements in membrane performance are necessary, including optimization of the biomimetic design to maximize the water transport capabilities of Aqps.

6.1.4 Mechanically robust and highly permeable AquaporinZ biomimetic membranes (II)

Water transport through the robust AqpZ-embedded vesicular membrane has been explored in forward osmosis (FO) process. Simulation indicates that the water flux of the membrane is determined by both vesicle size and permeability, while the interior solute concentration of vesicles will impact the hydrostatic pressure of the vesicles. To further

enhance the FO performance of the membrane, an increment in vesicle permeability or vesicle size or both will be required.

6.2 Recommendations

Based on the experimental results obtained and the conclusions drawn above, some additional projects that resulted from this work can be proposed, which may provide further insights in this area.

(1) Improvement of AqpZ incorporation efficiency. The highest permeability of the active layer, which has been prepared in this study, is $22\times10^{-7}m^3/m^2/s/bar$ (equivalent to 7.92 $L/m^2/h/bar$) (Appendix A-3). Our best permeability just reaches the same order of magnitude of the low pressure RO membrane [121]. Therefore, to make this membrane more competitive in the market will necessitate an order of magnitude increase of its permeability. To achieve this goal, we need to determine and improve the AqpZ incorporation efficiency. Our estimation about the AqpZ permeability is based on the hypothesis that AqpZ molecules are all incorporated into the amphiphilic matrix. In reality, it is difficult to measure the AqpZ molecule density on a membrane, because the protein concentration is too low to be detected. In addition, it is unclear why vesicle permeability will drop at a certain AqpZ to lipid/block copolymer ratio as shown many studies including our results (eg. Figure 2-4 and Figure 3-1). Therefore, it is important to develop a reliable assay so that we can get some clues to explain this phenomenon and the AqpZ incorporation efficiency can be optimized. One quantification

method is to label AqpZ proteins with fluorophores and to measure the fluorescence of the AqpZ incorporated vesicles (Appendix A-5). However, the fluorophores labeling yield may impact our final quantitation. An alternative method is to introduce isotopes into AqpZ proteins to aid the quantitation [122, 123].

(2) Determination of AqpZ permeability and transmembrane configuration. The permeability of AqpZ measurements are all based on the stopped-flow technique, which is an indirect measurement. Such measurement may be coupled with other dynamic changes of vesicles, such as vesicle fission. A more direct method may be preferred, for example, express AqpZ on oocyte cells to measure via cryoelectron microscopy [124] or optical microscope.

(3) Water transport is often regulated in plant and mammalian cells. This behavior relates to the gating phenomenon of aquaporins as they response to specific pH or osmolality or ions. In the plant plasma membrane intrinsic proteins (PIPs), water conductance is higher at neutral or basic pH and reduces about 98% in the acidic cytoplasmic pH or in Ca^{2+} enriched cytoplasm [125]. It has been found that Aqp0 [126], Aqp3 [127] and Aqp6 [128] are pH gating, while Aqp4 and Aqp5 [129] are insensitive to extracellular acidification and nickel. AqpZ is from *Escherichia coli*. In molecular dynamic simulation of AqpZ, it has been observed that Arg 189 which is located at the ar/R selectivity filter can flip between two distinct conformations: open and close states [129]. However, the thermodynamic

gradient of these two states are not significant, so it is insufficient to stabilize AqpZ in one or the other state. Borgnia and coworkers has found that the permeability of AqpZ is consistently similar in 1 mM mercury ions and in buffers with pH range of 5-7. Thus, no water gating phenomenon or simulation work has been reported for AqpZ so far. For water purification purpose, we are more interested in Aqps' stability in a wider pH range, specifically, pH 2-11. In addition, the stability of AqpZ in the presence of different heavy metal ions is worth to investigate. Finally, all the permeabilities of Aquaporin family are characterized by biochemists using osmotic pressure as the driving force. It will be interesting to investigate and understand whether and how Aqps can exhibit its capability under hydraulic pressure.

(4) AqpZ proteins are biodegradable. It has been questioned whether AqpZ will be digested by bacteria or prone to biofouling and mineral scaling in real water purification. However, in fact, AqpZ proteins are not just immobilized on the solid surface, but incorporated in an amphiphilic matrix. Thus, it is uncertain how stable this polymer-protein hybrid system can be. Therefore, it is worth to provide some experimental evidences to prove the long term stability of AqpZ.

(5) The biomimetic membrane is still far from commercialization. In order to make it a solution for all the world's water woes, this technology needs to be simple and cheap enough to offer an opportunity to the world's poor (Appendix A-5). Based on our current calculation, the cost of the selective layer can reach ~USD 5960/m^2,

which does not take into account of the substrate and the cost of module fabrication. It is worth noting that the cost of AqpZ is above 75% of the total cost of the selective layer. As compared with commercial RO membrane module, the cost of biomimetic membrane makes it far less competitive. Therefore, it is crucial to further reduce the production cost of biomimetic membranes.

REFERENCE

[1] D. Zejli, K.E. Aroui, A. Lazrak, K.E. Boury, A. Elmidaoui, Economic feasibility of a 11-MW wind powered reverse osmosis desalination system in Morocco, Desalin. Water Treat., 18 (2010) 164-174.

[2] L.F. Greenlee, D.F. Lawler, B.D. Freeman, B. Marrot, P. Moulin, Reverse osmosis desalination: Water sources, technology, and today's challenges, Water Research, 43 (2009) 2317-2348.

[3] A. Rahardianto, J.B. Gao, C.J. Gabelich, M.D. Williams, Y. Cohen, High recovery membrane desalting of low-salinity brackish water: Integration of accelerated precipitation softening with membrane RO, J. Membr. Sci., 289 (2007) 123-137.

[4] M.D. Afonso, J.O. Jaber, M.S. Mohsen, Brackish groundwater treatment by reverse osmosis in Jordan, Desalination, 164 (2004) 157-171.

[5] I. Akin, G. Arslan, A. Tor, Y. Cengeloglu, M. Ersoz, Removal of arsenate As(V) and arsenite As(III) from water by SWHR and BW-30 reverse osmosis, Desalination, 281 (2011) 88-92.

[6] S. Lee, R.M. Lueptow, Reverse osmosis filtration for space mission wastewater: membrane properties and operating conditions, J. Membr. Sci., 182 (2001) 77-90.

[7] A.H. Zhu, A. Rahardianto, P.D. Christofides, Y. Cohen, Reverse osmosis desalination with high permeability membranes - Cost optimization and research needs, Desalin. Water Treat., 15 (2010) 256-266.

[8] H.J. Oh, T.M. Hwang, S. Lee, A simplified simulation model of RO systems for seawater desalination, Desalination, 238 (2009) 128-139.

[9] A.H. Zhu, P.D. Christofides, Y. Cohen, Minimization of energy consumption for a two-pass membrane desalination: Effect of energy recovery, membrane rejection and retentate recycling, J. Membr. Sci., 339 (2009) 126-137.

[10] T.Y. Cath, A.E. Childress, M. Elimelech, Forward osmosis: Principles, applications, and recent developments, J. Membr. Sci., 281 (2006) 70-87.

[11] T.S. Chung, S. Zhang, K.Y. Wang, J.C. Su, M.M. Ling, Forward osmosis processes: yesterday, today and tomorrow, Desalination, 287 (2012) 78-81.

[12] J. Su, T.-S. Chung, Sublayer structure and reflection coefficient and their effects on concentration polarization and membrane performance in FO processes, J. Membr. Sci., 376 (2011) 214-224.

[13] R.C. Ong, T.S. Chung, Fabrication and positron annihilation spectroscopy (PAS) characterization of cellulose triacetate membranes for forward osmosis, J. Membr. Sci., (2012).

[14] K.Y. Wang, Q. Yang, T.S. Chung, R. Rajagopalan, Enhanced forward osmosis from chemically modified polybenzimidazole (PBI) nanofiltration hollow fiber membranes with a thin wall, Chem. Eng. Sci., 64 (2009) 1577-1584.

[15] K.Y. Wang, T.-S. Chung, G. Amy, Developing Thin-film-composite forward osmosis membranes based on the PES/SPSf substrate through interfacial polymerization, AIChE J., (2012).

[16] R.B. Bird, W.E. Stewart, E.N. Lightfoot, Transport Phenomena, 2nd ed. Wiley: New York, (2002).

[17] J.G. Wijmans, R.W. Baker, The solution-diffusion model - A review, J. Membr. Sci., 107 (1995) 1-21.

[18] M. Kumar, M. Grzelakowski, J. Zilles, M. Clark, W. Meier, Highly permeable polymeric membranes based on the incorporation of the functional water channel protein Aquaporin Z, Proc. Natl. Acad. Sci. USA, 104 (2007) 20719-20724.

[19] P. Agre, The aquaporin water channels, Proc. Am. Thorac. Soc., 3 (2006) 5-13.

[20] C. Maurel, Aquaporins and water permeability of plant membranes, Annu. Rev. Plant. Biol., 48 (1997) 399-429.

[21] G. Calamita, W.R. Bishai, G.M. Preston, W.B. Guggino, P. Agre, Molecular-cloning and olecular-cloning and characterization of AQPZ, a water channel from Escherichia-Coli, J. Biol. Chem., 270 (1995) 29063-29066.

[22] M. Bonhivers, J.M. Carbrey, S.J. Gould, P. Agren, Aquaporins in Saccharomyces - Genetic and functional distinctions between laboratory and wild-type strains, J Biol Chem, 273 (1998) 27565-27572.

[23] K. Ishibashi, S. Sasaki, K. Fushimi, S. Uchida, M. Kuwahara, H. Saito, T. Furukawa, K. Nakajima, Y. Yamaguchi, T. Gojobori, F. Marumo, Molecular-cloning and expression of A member of the aquaporin family with permeability to glycerol and urea in addiotn to water expressed at the basolateral membrane of kidney collecting duct cells, Proc. Natl. Acad. Sci. USA, 91 (1994) 6269-6273.

[24] K. Ishibashi, M. Kuwahara, Y. Gu, Y. Kageyama, A. Tohsaka, F. Suzuki, F. Marumo, S. Sasaki, Cloning and functional expression of a new water channel abundantly expressed in the testis permeable to water, glycerol, and urea, J. Biol. Chem., 272 (1997) 20782-20786.

[25] M. Ikeda, E. Beitz, D. Kozono, W.B. Guggino, P. Agre, M. Yasui, Characterization of aquaporin-6 as a nitrate channel in mammalian cells - Requirement of pore-lining residue threonine 63, J. Biol. Chem., 277 (2002) 39873-39879.

[26] T.P. Jahn, A.L.B. Moller, T. Zeuthen, L.M. Holm, D.A. Klaerke, B. Mohsin, W. Kuhlbrandt, J.K. Schjoerring, Aquaporin homologues in plants and mammals transport ammonia, Febs Letters, 574 (2004) 31-36.

[27] S.M. Saparov, K. Liu, P. Agre, P. Pohl, Fast and selective ammonia transport by aquaporin-8, J. Biol. Chem., 282 (2007) 5296-5301.

[28] R. Wysocki, C.C. Chery, D. Wawrzycka, M. Van Hulle, R. Cornelis, J.M. Thevelein, M.J. Tamas, The glycerol channel Fps1p mediates the uptake of arsenite and antimonite in Saccharomyces cerevisiae, Mol Microbiol, 40 (2001) 1391-1401.

[29] O.I. Sanders, C. Rensing, M. Kuroda, B. Mitra, B.P. Rosen, Antimonite is accumulated by the glycerol facilitator GlpFin Escherichia coli, J. Bacteriology, 179 (1997) 3365-3367.

[30] G.V.R. Prasad, L.A. Coury, F. Finn, M.L. Zeidel, Reconstituted aquaporin 1 water channels transport CO2 across membranes, J. Biol. Chem., 273 (1998) 33123-33126.

[31] N.L. Nakhoul, B.A. Davis, M.F. Romero, W.F. Boron, Effect of expressing the water channel aquaporin-1 on the CO2 permeability of Xenopus oocytes, Am J. Physiol. Cell Physiol., 274 (1998) C543-C548.

[32] M. Herrera, N.J. Hong, J.L. Garvin, Aquaporin-1 transports NO across cell membranes, Hypertension, 48 (2006) 157-164.

[33] B.X. Yang, D. Zhao, E. Solenov, A.S. Verkman, Evidence from knockout mice against physiologically significant aquaporin 8-facilitated ammonia transport, Am J. Physiol. Cell Physiol., 291 (2006) C417-C423.

[34] B.L. de Groot, H. Grubmuller, The dynamics and energetics of water permeation and proton exclusion in aquaporins, Curr. Opin. Struct. Biol., 15 (2005) 176-183.

[35] B.L. de Groot, H. Grubmuller, Water permeation across biological membranes: Mechanism and dynamics of aquaporin-1 and GlpF, Science, 294 (2001) 2353-2357.

[36] M.L. Zeidel, S.V. Ambudkar, B.L. Smith, P. Agre, Reconstitution of functioal water channels in liposomes containing purified red-cell CHIP28, Biochemistry, 31 (1992) 7436-7440.

[37] M.J. Borgnia, D. Kozono, G. Calamita, P.C. Maloney, P. Agre, Functional reconstitution and characterization of AqpZ, the E-coli water channel protein, J. Mol. Biol., 291 (1999) 1169-1179.

[38] S.M. Gruner, Stability of lyotropic phases with curved interfaces, J. Phys. Chem., 93 (1989) 7562-7570.

[39] D. Papahadjopoulos, T.M. Allen, A. Gabizon, E. Mayhew, K. Matthay, S.K. Huang, K.D. Lee, M.C. Woodle, D.D. Lasic, C. Redemann, F.J. Martin, Sterically stablized liposomes-improvements in pharmacokinetics and antitumor therapeutic efficacy, Proc. Natl. Acad. Sci. USA, 88 (1991) 11460-11464.

[40] W.S. Davidson, A. Jonas, D.F. Clayton, J.M. George, Stabilization of alpha-synuclein secondary structure upon binding to synthetic membranes, J. Biol. Chem., 273 (1998) 9443-9449.

[41] S.L. Schendel, Z.H. Xie, M.O. Montal, S. Matsuyama, M. Montal, J.C. Reed, Channel formation by antiapoptotic protein Bcl-2, Proc. Natl. Acad. Sci. USA, 94 (1997) 5113-5118.

[42] C. Dietrich, L.A. Bagatolli, Z.N. Volovyk, N.L. Thompson, M. Levi, K. Jacobson, E. Gratton, Lipid rafts reconstituted in model membranes, Biophys. J., 80 (2001) 1417-1428.

[43] E. Sackmann, Supported membranes: Scientific and practical applications, Science, 271 (1996) 43-48.

[44] A.L. Plant, Supported hybrid bilayer membranes as rugged cell membrane mimics, Langmuir, 15 (1999) 5128-5135.

[45] B. Raguse, V. Braach-Maksvytis, B.A. Cornell, L.G. King, P.D.J. Osman, R.J. Pace, L. Wieczorek, Tethered lipid bilayer membranes: Formation and ionic reservoir characterization, Langmuir, 14 (1998) 648-659.

[46] M.L. Wagner, L.K. Tamm, Tethered polymer-supported planar lipid bilayers for reconstitution of integral membrane proteins: Silane-polyethyleneglycol-lipid as a cushion and covalent linker, Biophys. J., 79 (2000) 1400-1414.

[47] T. Haefele, K. Kita-Tokarczyk, W. Meier, Phase behavior of mixed Langmuir monolayers from amphiphilic block copolymers and an antimicrobial peptide, Langmuir, 22 (2006) 1164-1172.

[48] B.M. Discher, Y.Y. Won, D.S. Ege, J.C.M. Lee, F.S. Bates, D.E. Discher, D.A. Hammer, Polymersomes: Tough vesicles made from diblock copolymers, Science, 284 (1999) 1143-1146.

[49] R. Stoenescu, A. Graff, W. Meier, Asymmetric ABC-triblock copolymer membranes induce a directed insertion of membrane proteins, Macromol. Biosci., 4 (2004) 930-935.

[50] K. Kita-Tokarczyk, J. Grumelard, T. Haefele, W. Meier, Block copolymer vesicles - using concepts from polymer chemistry to mimic biomembranes, Polymer, 46 (2005) 3540-3563.

[51] S. Egli, M.G. Nussbaumer, V. Balasubramanian, M. Chami, N. Bruns, C. Palivan, W. Meier, Biocompatible Functionalization of Polymersome Surfaces: A new approach to surface immobilization and cell targeting using polymersomes, J. Am. Chem. Soc., 133 (2011) 4476-4483.

[52] F. Ahmed, D.E. Discher, Self-porating polymersomes of PEG-PLA and PEG-PCL: hydrolysis-triggered controlled release vesicles, J. Controlled Release, 96 (2004) 37-53.

[53] E.R. Gillies, J.M.J. Frechet, pH-responsive copolymer assemblies for controlled release of doxorubicin, Bioconjug. Chem., 16 (2005) 361-368.

[54] B.A. Lewis, D.M. Engelman, Lipid bilayer thickness varies linearly with acyl chain-length in fluid phosphatidylcholine vesicles, J. Mol. Biol., 166 (1983) 211-217.

[55] A. Graff, Insertion of membrane proteins in artificial polymer membranes, PhD Thesis, University of Basel, (2004).

[56] V. Pata, N. Dan, The effect of chain length on protein solubilization in polymer-based vesicles (polymersomes), Biophys. J., 85 (2003) 2111-2118.

[57] M. Grzelakowski, O. Onaca, P. Rigler, M. Kumar, W. Meier, Immobilized protein-polymer nanoreactors, Small, 5 (2009) 2545-2548.

[58] A. Mecke, C. Dittrich, W. Meier, Biomimetic membranes designed from amphiphilic block copolymers, Soft Matter, 2 (2006) 751-759.

[59] F. Najafi, M.N. Sarbolouki, Biodegradable micelles/polymersomes from fumaric/sebacic acids and poly(ethylene glycol), Biomaterials, 24 (2003) 1175-1182.

[60] A. Chonn, P.R. Cullis, Recent advances in lipsomal drug-delivery systems, Curr. Opin. Biotechnol., 6 (1995) 698-708.

[61] J.L. Rigaud, B. Pitard, D. Levy, Reconstution of membrane-proteins into liposomes-application to energy transducing membrane-proteins, Biochim. Biophys. Acta-Bioenergetics, 1231 (1995) 223-246.

[62] J.J. Lacapere, F. Delavoie, H. Li, G. Peranzi, J. Maccario, V. Papadopoulos, B. Vidic, Structural and functional study of reconstituted peripheral benzodiazepine receptor, Biochem. Biophys. Res. Commun., 284 (2001) 536-541.

[63] M. Sauer, T. Haefele, A. Graff, C. Nardin, W. Meier, Ion-carrier controlled precipitation of calcium phosphate in giant ABA triblock copolymer vesicles, Chem.Commun., (2001) 2452-2453.

[64] K. Nakatani, T. Morita, S. Kimura, Vertical and directional insertion of helical peptide into lipid bilayer membrane, Langmuir, 23 (2007) 7170-7177.

[65] J.P. Reeves, R.M. Dowben, Formation and properties of thin walled phospholipid vesicles, J. Cell Physiol., 73 (1969) 49-60.

[66] D. Needham, E. Evans, Structure and mechanical-properties of giant lipid (DMPC) vesicle bilayers from 20-degrees-C beflow to 10-degree-C above the liquid crystal crystalline phase transition at 24-degree-C, Biochemistry, 27 (1988) 8261-8269.

[67] M.I. Angelova, D.S. Dimitrov, Liposome electroformation, Faraday Discuss., 81 (1986) 303-311.

[68] J.M.H. Kremer, M.W.J. Esker, C. Pathmamanoharan, P.H. Wiersema, Vesicles of variable diameter prepared by a modified injection method, Biochemistry, 16 (1977) 3932-3935.

[69] W. S.H., The physical nature of bilayer membranes, Ion Channel Reconstitution, (1986) 1-32.

[70] A.P. Girard-Egrot, B. L.J., Langmuir-blodgett technique for synthesis of biomimetic lipid membranes, Nanobiotechnology of Biomimetic Membranes, (2006) 23-74.

[71] K.L. Weirich, J.N. Israelachvili, D.K. Fygenson, Bilayer edges catalyze supported lipid bilayer formation, Biophys. J., 98 (2010) 85-92.

[72] H. Bermudez, A.K. Brannan, D.A. Hammer, F.S. Bates, D.E. Discher, Molecular weight dependence of polymersome membrane structure, elasticity, and stability, Macromolecules, 35 (2002) 8203-8208.

[73] J. Dorn, S. Belegrinou, M. Kreiter, E.K. Sinner, W. Meier, Planar block copolymer membranes by vesicle spreading, Macromol. Biosci., 11 (2011) 514-525.

[74] E. Rakhmatullina, W. Meier, Solid-supported block copolymer membranes through interfacial adsorption of charged block copolymer vesicles, Langmuir, 24 (2008) 6254-6261.

[75] A.K. Meinild, D.A. Klaerke, T. Zeuthen, Bidirectional water fluxes and specificity for small hydrophilic molecules in aquaporins 0-5, J. Biol. Chem., 273 (1998) 32446-32451.

[76] Y. Kaufman, A. Berman, V. Freger, Supported lipid bilayer membranes for water purification by reverse osmosis, Langmuir, 26 (2010) 7388-7395.

[77] S. Ibragimova, K. Stibius, P. Szewczykowski, M. Perry, H. Bohr, C. Helix-Nielsen, Hydrogels for in situ encapsulation of biomimetic membrane arrays, Polymers for Advanced Technologies, 23 (2012) 182-189.

[78] T.J. Jeon, N. Malmstadt, J.J. Schmidt, Hydrogel-encapsulated lipid membranes, J. Am. Chem. Soc., 128 (2006) 42-43.

[79] C.H. Nielsen, Biomimetic membranes for sensor and separation applications, Anal. Bioanal. Chem., 395 (2009) 697-718.

[80] M.B. Lande, N.A. Priver, M.L. Zeidel, Determinants of apical membrane permeabilities of barrier epthelia, Am. J. Physiol. Cell Physiol., 267 (1994) C367-C374.

[81] M.R. Toon, A.K. Solomon, Transport parameters in the human red-cell membrane-solute-membrane interaction of amides and ureas, Biochim. Biophys. Acta, 1063 (1991) 179-190.

[82] I. Mey, M. Stephan, E.K. Schmitt, M.M. Muller, M. Ben Amar, C. Steinem, A. Janshoff, Local membrane mechanics of pore-spanning bilayers, J. Am. Chem. Soc., 131 (2009) 7031-7039.

[83] S. Garcia-Manyes, F. Sanz, Nanomechanics of lipid bilayers by force spectroscopy with AFM: A perspective, Biochim Biophys Acta-Biomembranes, 1798 (2010) 741-749.

[84] S. Hillyard, Biomimetic membranes for sensor and separation spplications, Sensing meets separation: water transport across biological membranes. In: Hélix-Nielsen C (ed) (2012) 2-4.

[85] C. Hennesthal, J. Drexler, C. Steinem, Membrane-suspended nanocompartments based on ordered pores in alumina, Chemphyschem, 3 (2002) 885-889.

[86] S. Garcia-Manyes, L. Redondo-Morata, G. Oncins, F. Sanz, Nanomechanics of Lipid Bilayers: Heads or Tails?, J. Am. Chem. Soc., 132 (2010) 12874-12886.

[87] R.P. Goncalves, G. Agnus, P. Sens, C. Houssin, B. Bartenlian, S. Scheuring, Two-chamber AFM: probing membrane proteins separating two aqueous compartments, Nature Methods, 3 (2006) 1007-1012.

[88] S. Steltenkamp, M.M. Muller, M. Deserno, C. Hennesthal, C. Steinem, A. Janshoff, Mechanical properties of pore-spanning lipid bilayers probed by atomic force microscopy, Biophys. J., 91 (2006) 217-226.

[89] S. Kaufmann, G. Papastavrou, K. Kumar, M. Textor, E. Reimhult, A detailed investigation of the formation kinetics and layer structure of poly(ethylene glycol) tether supported lipid bilayers, Soft Matter, 5 (2009) 2804-2814.

[90] C. Hennesthal, C. Steinem, Pore-spanning lipid bilayers visualized by scanning force microscopy, J. Am. Chem. Soc., 122 (2000) 8085-8086.

[91] P.B. Contino, C.A. Hasselbacher, J.B.A. Ross, Y. Nemerson, Use of an oriented transmembrane protein to probe the assembly of a supported phospholipid-bilayer, Biophys. J., 67 (1994) 1113-1116.

[92] R.K. Hite, Z.L. Li, T. Walz, Principles of membrane protein interactions with annular lipids deduced from aquaporin-0 2D crystals, Embo Journal, 29 (2010) 1652-1658.

[93] B. Lorenz, I. Mey, S. Steltenkamp, T. Fine, C. Rommel, M.M. Muller, A. Maiwald, J. Wegener, C. Steinem, A. Janshoff, Elasticity mapping of pore-suspending native cell membranes, Small, 5 (2009) 832-838.

[94] E. Evans, W. Rawicz, Entropy-driven tension and bending elasticity in concensed-fluid membranes, Phys. Rev. Lett., 64 (1990) 2094-2097.

[95] K.Y. Wang, R.C. Ong, T.-S. Chung, Double-Skinned Forward Osmosis Membranes for Reducing Internal Concentration Polarization within the Porous Sublayer, Ind. Eng. Chem. Res., 49 (2010) 4824-4831.

[96] P. Pohl, S.M. Saparov, M.J. Borgnia, P. Agre, Highly selective water channel activity measured by voltage clamp: Analysis of planar lipid bilayers reconstituted with purified AqpZ, Proc. Natl. Acad. Sci. USA, 98 (2001) 9624-9629.

[97] H. Wang, T.-S. Chung, Y.W. Tong, W. Meier, Z. Chen, M. Hong, K. Jeyaseelan, A. Armugam, Preparation and characterization of pore-suspending biomimetic membranes embedded with Aquaporin Z on carboxylated polyethylene glycol polymer cushion, Soft Matter, 7 (2011) 7274-7280.

[98] J.P. Hensen., Biomimetic water membrane comprising aquaporins used in the production of salinity power., USA, Invention patent, US2009/0007555 A1., (2009).

[99] M. Wirde, U. Gelius, L. Nyholm, Self-assembled monolayers of cystamine and cysteamine on gold studied by XPS and voltammetry, Langmuir, 15 (1999) 6370-6378.

[100] P.J. Patty, B.J. Frisken, The pressure-dependence of the size of extruded vesicles, Biophys. J., 85 (2003) 996-1004.

[101] J.H. Wang, Self-diffusion coefficients of water, J. Phys. Chem., 69 (1965) 4412.

[102] J.S. Hansen, M. Perry, J. Vogel, T. Vissing, C.R. Hansen, O. Geschke, J. Emneus, C.H. Nielsen, Development of an automation technique for the establishment of functional lipid bilayer arrays, J. Micromech. Microeng., 19 (2009).

[103] J. Vogel, M. Perry, J.S. Hansen, P.Y. Bolinger, C.H. Nielsen, O. Geschke, A support structure for biomimetic applications, J. Micromech. Microeng., 19 (2009).

[104] J.S. Hansen, M. Perry, J. Vogel, J.S. Groth, T. Vissing, M.S. Larsen, O. Geschke, J. Emneus, H. Bohr, C.H. Nielsen, Large scale biomimetic membrane arrays, Anal. Bioanal. Chem., 395 (2009) 719-727.

[105] A. Gonzalez-Perez, K.B. Stibius, T. Vissing, C.H. Nielsen, O.G. Mouritsen, Biomimetic triblock copolymer membrane arrays: a stable template for functional membrane proteins, Langmuir, 25 (2009) 10447-10450.

[106] M.R. Lander, S. Ibragimova, C. Rein, J. Vogel, K. Stibius, O. Geschke, M. Perry, C. Helix-Nielsen, Biomimetic membrane arrays on cast hydrogel supports, Langmuir, 27 (2011) 7002-7007.

[107] H.L. Wang, T.S. Chung, Y.W. Tong, W. Meier, Z.C. Chen, M.H. Hong, K. Jeyaseelan, A. Armugam, Preparation and characterization of pore-suspending biomimetic membranes embedded with Aquaporin Z on carboxylated polyethylene glycol polymer cushion, Soft Matter, 7 (2011) 7274-7280.

[108] H. Lee, J. Rho, P.B. Messersmith, Facile Conjugation of Biomolecules onto Surfaces via Mussel Adhesive Protein Inspired Coatings, Adv. Mater., 21 (2009) 431-434.

[109] H. Lee, S.M. Dellatore, W.M. Miller, P.B. Messersmith, Mussel-inspired surface chemistry for multifunctional coatings, Science, 318 (2007) 426-430.

[110] B.D. McCloskey, H.B. Park, H. Ju, B.W. Rowe, D.J. Miller, B.J. Chun, K. Kin, B.D. Freeman, Influence of polydopamine deposition conditions on pure water flux and foulant adhesion resistance of reverse osmosis, ultrafiltration, and microfiltration membranes, Polymer, 51 (2010) 3472-3485.

[111] H. Wang, T.S. Chung, Y.W. Tong, K. Jeyaseelan, A. Armugam, Z. Chen, M. Hong, W. Meier, Highly permeable and selective pore-spanning biomimetic membrane embedded with Aquaporin Z, Small, 8 (2012) 1185-1190.

[112] P.H.H. Duong, T.S. T.S. Chung, K. Jeyaseelan, A. Armugam, Z. Chen, J. Yang, M. Hong, Planar biomimetic aquaporin-incorporated triblock copolymer membranes on porous alumina supports for nanofiltration, J. Membr. Sci., 409-410 (2012) 34-43.

[113] C. Nardin, S. Thoeni, J. Widmer, M. Winterhalter, W. Meier, Nanoreactors based on (polymerized) ABA-triblock copolymer vesicles, Chemical Communications, (2000) 1433-1434.

[114] C. Nardin, T. Hirt, J. Leukel, W. Meier, Polymerized ABA triblock copolymer vesicles, Langmuir, 16 (2000) 1035-1041.

[115] J. Dean, Analytical chemistry handbook, McGraw-Hill Book Co., (1995).

[116] M. Grzelakowski, Design at nano-scale: biomimetic block copolymers for polymer-protein hybrid materials, PhD Thesis, University of Basel, (2009).

[117] C. Tanford, HYDROSTATIC-PRESSURE IN SMALL PHOSPHOLIPID-VESICLES, Proc. Natl. Acad. Sci. USA, 76 (1979) 3318-3319.

[118] O. Kedem, A. Katchalsky, Thermodynamic analysis of the permeability of biological membranes to non-electrolytes, Biochim Biophys Acta, 27 (1958) 229-246.

[120] W.D. Niles, F.S. Cohen, A. Finkelstein, HYDROSTATIC PRESSURES DEVELOPED BY OSMOTICALLY SWELLING VESICLES BOUND TO PLANAR MEMBRANES, Journal of General Physiology, 93 (1989) 211-244.

[120] J.R. McCutcheon, M. Elimelech, Influence of concentrative and dilutive internal concentration polarization on flux behavior in forward osmosis, J. Membr. Sci., 284 (2006) 237-247.

[121] A.H. Zhu, P.D. Christofides, Y. Cohen, On RO membrane and energy costs and associated incentives for future enhancements of membrane permeability (vol 344, pg 1, 2009), J. Membr. Sci., 346 (2010) 361-361.

[122] G.W. Becker, Stable isotopic labeling of proteins for quantitative proteomic applications, Briefings in Functional Genomics & Proteomics, 7 (2008) 371-382.

[123] D. Nanavati, M. Gucek, J.L.S. Milne, S. Subramaniam, S.P. Markey, Stoichiometry and absolute quantification of proteins with mass spectrometry using fluorescent and isotope-labeled concatenated peptide standards, Molecular & Cellular Proteomics, 7 (2008) 442-447.

[124] C. Delamarche, D. Thomas, J.P. Rolland, A. Froger, J. Gouranton, M. Svelto, P. Agre, G. Calamita, Visualization of AqpZ-mediated water permeability in Escherichia coli by cryoelectron microscopy, Journal of Bacteriology, 181 (1999) 4193-4197.

[125] L. Verdoucq, A. Grondin, C. Maurel, Structure-function analysis of plant aquaporin AtPIP2;1 gating by divalent cations and protons, Biochemical Journal, 415 (2008) 409-416.

[126] K.L. Nemeth-Cahalan, K. Kalman, J.E. Hall, Molecular basis of pH and Ca2+ regulation of aquaporin water permeability, Journal of General Physiology, 123 (2004) 573-580.

[127] M. Zelenina, A.A. Bondar, S. Zelenin, A. Aperia, Nickel and extracellular acidification inhibit the water permeability of human aquaporin-3 in lung epithelial cells, J. Biol. Chem., 278 (2003) 30037-30043.

[128] M. Yasui, A. Hazama, T.H. Kwon, S. Nielsen, W.B. Guggino, P. Agre, Rapid gating and anion permeability of an intracellular aquaporin, Nature, 402 (1999) 184-187.

[129] J.S. Jiang, B.V. Daniels, D. Fu, Crystal structure of AqpZ tetramer reveals two distinct Arg-189 conformations associated with water permeation through the narrowest constriction of the water-conducting channel, J. Biol. Chem., 281 (2006) 454-460.

APPENDIX

A-1 Calculation of specific energy consumption in single stage RO

As an example of the analysis of RO energy consumption, the most simplified one-step RO system is considered (Figure A-1). The fixed parameters in this example are listed in Table A-1. We assume that water recovery is 0.5 and the water productivity is 0.5m^3/s. According to the fixed parameters, the required membrane area that can achieve the permeate flux (water productivity) of 0.5m^3/s can be estimated.

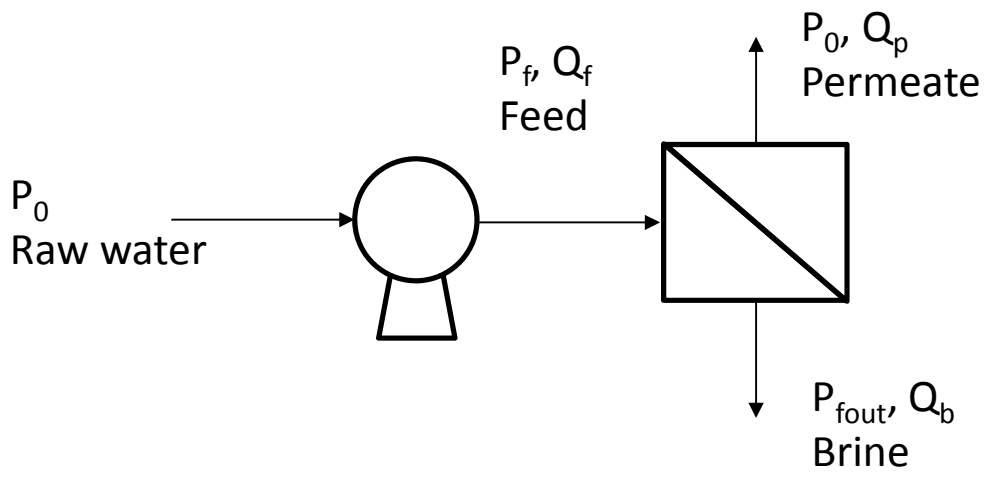

Figure A-1 Schematic diagram of a simplified one-step RO system.

Table A-1 Known parameters in the one-step RO process

Item	Symbol	Value	Unit
Water recovery	r_w	0.5	m3
Feed inlet flowrate	Q_f	1	m^3/s
Permeate flowrate	Q_p	0.5	m^3/s
Feed inlet pressure	$P_{f,in}$	60	bar
Feed outlet pressure	$P_{f,out}$	57	bar
Inlet salt	C_{in}	0.6	mol/L

concentration			
Pressure of permeate	P_0	1	atm
Conventional RO membrane permeability	$L_{p,RO}$	6×10^{-7}	$m^3/m^2/s/bar$

The outlet salt concentration is

$$C_{out} = \frac{C_{in}}{1-r} = \frac{0.6mol/L}{1-0.5} = 1.2mol/L$$

The osmotic pressures of inlet and brine flows can be calculated respectively:

$$\pi_{in} = \lambda cRT = 2\times0.6mol/L\times8.314\times10^{-2}Lbar/K/mol\times293K = 29.2bar$$

$$\pi_{out} = \lambda cRT = 2\times1.2mol/L\times8.314\times10^{-2}Lbar/K/mol\times293K = 58.4bar$$

The net transmembrane driving pressure $\overline{NDP}$ can be calculated based on the inlet and brine osmotic pressure:

$$\overline{NDP} = \Delta P - \overline{\Delta\pi} = \frac{\left(P_{f,in} - P_0 - \pi_{in}\right) + \left(P_{f,out} - P_0 - \pi_{out}\right)}{2}$$
$$= \frac{(60-1-29.2)bar + (57-1-58.4)bar}{2}$$
$$= 13.7bar$$

Thus, the membrane area can be estimated as below:

$$A_{RO} = \frac{Q_p}{\overline{NDP}\cdot L_{p,RO}} = \frac{0.5m^3/s}{13.7bar\times6\times10^{-7}m^3/m^2/s/bar} = 6.1\times10^4 m^2$$

The rate of work done by the pump:

$$\dot{W} = \Delta P\cdot Q_f = \left(P_{f,in} - P_0\right)Q_f$$

Accordingly, the specific energy consumption for this RO process is given by:

$$SEC = \frac{\dot{W}}{Q_p} = \frac{\left(P_{f,in} - P_0\right)Q_f}{\overline{NDP} \cdot A_{RO} \cdot L_{p,RO}}$$

Taking the fixed parameters in Table 8.1 as an example, the specific energy consumption can be calculated using equation (8-6) and (8-7):

$$\dot{W} = \Delta P \cdot Q_f = \left(P_{f,in} - P_0\right)Q_f = (60-1)bar \times 1m^3/s \times 10^5 = 5.9 \times 10^6 W$$

$$SEC = \frac{\dot{W}}{Q_p} = \frac{5.9 \times 10^6 W}{0.5m^3/s} \frac{1kW}{3600s/h \times 1000W} = 3.3kW/h$$

By fixing the membrane area and all the parameters in Table A-1, except $L_{p,RO}$, a relationship between SEC and $L_{p,RO}$ can thus be obtained.

A-2 Expression and purification of AqpZ

Genomic DNA of E. coli K-12 strain DH5α was extracted and subsequently used to clone the AqpZ gene based on Calamita *et al* [1]. The AqpZ gene was amplified and cloned into the pCR-4 vector using the TOPO cloning kit (Invitrogen, USA). The positive clones were sequenced and further subcloned into an expression vector, pQE-30-Xa with ampicillin selection and an amino-terminal 6×His affinity tag followed by Factor Xa digestion site (Qiagen, USA). The vector was modified in our laboratory by removing the Factor Xa protease digestion site and increasing the length of the histidine tag from 6 to 10 residues. The plasmids were then transformed into the E. coli strain TOP10F, and the transformants were grown at 37 °C to 0.6 – 1 OD at 600 nm in LB with ampicillin (100 mg/l), and induced with isopropyl-D-thiogalactoside (1 mM) for 5 hours at 30 °C. Cells were harvested and lysed by sonication in phosphate buffered saline (PBS, pH 7.4)

containing β-dodecyl maltoside (1%) (Anatrace, Maumee, Ohio, United States) and phenylmethylsulforyl fluoride (0.5 mM). Cellular debris was pelleted at 10000 rpm for 45 min and discarded. Membranes were recovered from supernatant by centrifugation at 37000 rpm for 60 min. AqpZ was solubilized from membranes by agitation in dodecyl maltoside (1%) and PBS for 12 – 16 hours. Solubilized protein was subjected to a second centrifugation at 40,000 rpm for another 60 min. The resulting recombinant AqpZ protein containing the 10 His tag at the N-terminal region was checked on 10% SDS-PAGE before using it for incorporation in membranes (Figure A-2 and Figure A-3).

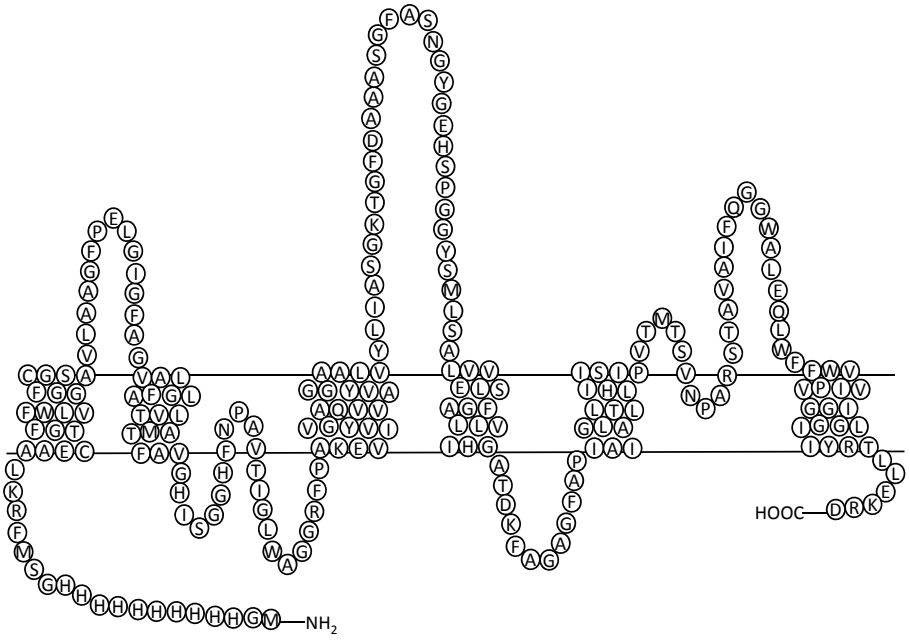

Figure A-2 Predicted amino acid sequence of 10 his-AqpZ prepared in this study.

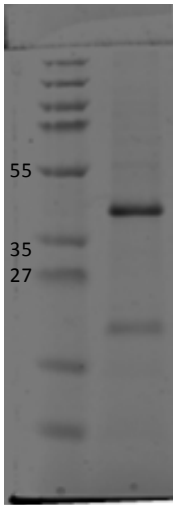

Figure A-3 Electrophoretic analysis of purified 10-His-AqpZ. Purified recombinant his-tag AqpZ was resolved on a 10% SDS-PAGE using Tris/Tricine buffer system. Lane M contains protein ladder (kDa) marked. Both monomer and dimer form of the protein is observed.

A-3 Estimation of water permeability of an AqpZ monomer

In order to estimate the number of AqpZ in a vesicle, the molecular weight of a vesicle M_v has to be estimated first using the equation below [2]:

$$M_v = \frac{4\pi N_A}{3\upsilon}\left(3R_v{}^2\delta - 3R_v\delta^2 + \delta^3\right)$$

where N_A is the Avogardro's number, ν is the specific volume of a vesicle (~1 cm^3/g), R_v is the vesicle radius and δ is the wall thickness of vesicle.

$$M_v = \frac{4\pi N_A}{3\upsilon}\left(3R_v{}^2\delta - 3R_v\delta^2 + \delta^3\right)$$
$$= \frac{4\times 3.14\times 6.02\times 10^{23}/mol}{3\times 1 cm^3/g}$$
$$\times\left[3\times\left(149\times10^{-7}cm/2\right)^2\times\left(8\times10^{-7}cm\right) - 3\times\left(149\times10^{-7}cm/2\right)\times\left(8\times10^{-7}cm\right)^2 + \left(8\times10^{-7}cm\right)^3\right]$$
$$= 3.0\times10^8 g/mol$$

The number of ABA block copolymer units N_{ABA} can be calculated as:

$$N_{ABA} = \frac{M_v}{M_{ABA}} = \frac{3\times10^8\, g/mol}{6000\, g/mol} = 5\times10^4$$

Accordingly, the number of incorporated AqpZ subunits N_{AqpZ} can be calculated below:

$$N_{AqpZ} = \frac{N_{ABA}}{R_{ABA/AqpZ}} = \frac{5\times10^4}{100} = 5\times10^2$$

The average permeability $P_{f,\,\text{vesicle}}$ of vesicles is 3000 μm/s, thus the permeability of AqpZ, p_f, is below:

$$p_f = \frac{P_f A_v}{N_{AqpZ}} = \frac{3000\times10^{-4}\, cm/s}{500} \times 4\times3.14\times\left(\frac{149}{2}\times10^{-7}\, cm\right)^2 = 4.2\times10^{-13}\, cm^3/s$$

A-4 Calculation of the theoretical water flux of biomimetic membrane

Assume that the permeability Pf is 3000μm/s, the permeability coefficient can be calculated as below:

$$L_p = \frac{P_f \overline{V}_w}{RT} = \frac{3000\times10^{-6}\, m/s\times18\times10^{-6}\, m^3/mol}{8.314\times293\, Pa\cdot m^3/mol}\frac{100000\, Pa}{1 bar} \approx 22\times10^{-7}\, m^3/(m^2\cdot s\cdot bar)$$

Table A-2 Theoretical water flux estimated from vesicle permeability (Driving force 1M NaCl)

Molar ratio of polymer to AqpZ	P_f ($\times10^{-3}$ μm/s)	L_p ($\times10^3$ $m^3/m^2/h/bar$)	Flux of the selective layer ($L/m^2/h$)	Flux after consider porosity ($L/m^2/h$)*	Water flux in FO test ($L/m^2/h$)
100:1	2.89	7.69	374	93.6	73.8
200:1	2.33	6.21	302	75.6	51.8
300:1	2.23	5.93	289	72.1	46.3
400:1	1.80	4.79	233	58.2	36.8

*Porosity is measure about 20-25%. 25% is used for calculation.

A-5 Calculation of the cost of biomimetic membrane

The production and purification cost of AqpZ from our lab including manpower is about e_p USD115/mg. The unit price of the commercialized ABA block copolymer is e_{ABA} USD1800/5g.

In our study, 20 μl of vesicle solution (4 mg/mL) is used to prepare the selective layer on a porous substrate with an area of 1.9625×10^{-5} m^2. Amount of AqpZ that is consumed in the preparation can be estimated below:

$$m_{p1} = \frac{c_{ABA}}{M_{ABA}} \cdot r_{ABA/p} \cdot M_p \cdot \frac{V_{pre}}{V_{sample}} = \frac{4mg/ml}{6000g/mol}\frac{1}{400} \times 23000g/mol \times 0.020ml \approx 7.7\times10^{-4} mg$$

where c_{ABA} is the concentration of vesicle, M_{ABA} is the molecular weight of ABA block copolymer, $r_{ABA/p}$ is the molar ratio of ABA to AqpZ, M_p is the molecular weight of AqpZ, and V_{pre} is the volume that is consumed to prepare the selective layer with a membrane area of 1.9625×10^{-5} m^2.

Based on the calculation above, C_p, the cost of AqpZ that is consumed to prepare a membrane area of 1 m^2 can be estimated:

$$C_p = \frac{A_{tot}}{A_e} m_{p1} e_p = \frac{1m^2}{1.9625\times10^{-5} m^2} \times 7.7\times10^{-4} mg \times USD115/mg \approx USD4492.6$$

where A_{tot} is the assumed total membrane area 1 m^2, A_e is the membrane area that we obtain in our experiment.

The cost of the block copolymer is below:

$$C_{ABA} = \frac{A_{tot}}{A_e} V_{pre} \cdot c_{ABA} \cdot e_{ABA} = \frac{1m^2}{1.9625 \times 10^{-5} m^2} \times 0.02ml \times 4mg/ml \times \frac{USD1800}{5000mg} \approx USD1467.5$$

The total cost of the selective layer is about USD 5960/m^2. The cost of AqpZ is above 75% of the total cost of the selective layer.

A-6 Observation of AqpZ in lipid bilayer

The experimental results will be more convincing if we can observe the incorporated AqpZ molecules in the lipid bilayer and prove its configuration. However, technically, it is difficult to achieve. A preliminary experiment was designed and carried out to observe AqpZ in a DMPC lipid bilayer using Confocal Microscopy. 0.5% wt of rhodamine B 1,2-dihexadecanoyl-sn-glycero-3-phosphoethanolamine, triethylammonium salt (rhodamine B-DHPE, Invitrogen, USA) was mixed with DMPC before reconstitution of AqpZ proteins that are labeled with fluorescein isothiocyanate (FITC). Each AqpZ molecule was labeled with several FITC which reacts specifically to primary amine group. In Figure A-4a shows the red and green profiles of a multi-lamellar vesicle can be overlapped well at wall region of the vesicle. It indicates that the AqpZ molecules are incorporated in the vesicle membrane, but not encapsulated by the vesicle. A membrane patch can be obtained if we rupture the vesicles on a piece of glass coverslip. Figure A-4b and A-4c exhibit the solid supported DMPC bilayer with AqpZ incorporated. It is worth to notice that vesicle rupture does not lead to aggregation of FITC-labeled AqpZ molecules on the support. In contrast, the AqpZ molecules are segregated nicely on the support.

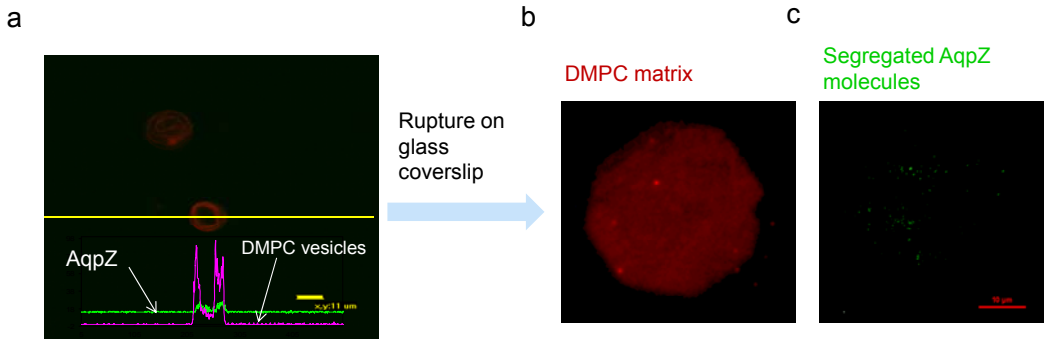

Figure A-4 Confocal Microscopy of fluorescence labeled vesicle.

Reference

[1] G. Calamita, W. R. Bishai, G. M. Preston, W. B. Guggino, and P. Agre. Molecular cloning and characterization of AqpZ, a water channel from Escherichia coli. *J. Biol. Chem.* 270 (1995) 270, 29063-29066.

[2] J.H. van Zanten, Unilamellar vesicle diameter and wall thickness determined by Zimm's light scattering technique. *Langmuir* 10 (1994) 4391–4393.

PUBLICATIONS

Journal Papers

H. L. Wang, G. F. Sun, H. H. P. Duong, P. S. Zhong, T.S. Chung. Book chapter: Aquaporin incorporated biomimetic membranes.Encyclopedia of Membranes. 2012

T.S. Chung, X. Li, R. C. Ong, Q. Ge, **H. L.Wang** and G. Han. Emerging forward osmosis (FO) technologies and challenges ahead for clean water and clean energy applications. Curr. Opin. Chem. Eng. (In press).

H. L. Wang, T. S. Chung, Y. W. Tong, K. Jeyaseelan, A. Armugam, Z. C. Chen, M. H. Hong, W. Meier,"Highly permeable and selective pore-spanning biomimetic membrane embedded with Aquaporin Z," Small. Volume 8 (8), 2012, pages 6001-6011.

H. L. Wang, T. S. Chung, Y. W. Tong, Z. C. Chen, M. H. Hong, K. Jeyaseelan, and A. Armugam, "Preparation and characterization of pore-suspending biomimetic membranes embedded with Aquaporin Z on carboxylated polyethylene glycol polymer brush," Soft Matter. Volume 7, 2011, pages 7274-7280.

R. Y. Wang, **H. L. Wang,** X. C. Wu,Y. L. Ji,Y. Qu, and T. S. Chung, "Chiral Assembly of Gold Nanorods with Collective Plasmonic Circular Dichroism Response," Soft Matter. Volume 7, 2011, pages 8370-8375.

H. L. Wang, Y. Li and T. S. Chung, "A fine match between the stereoselective ligands and membrane pore size for enhanced chiral separation performance via affinity ultrafiltration", AIChE. J. Volume 55(9), 2009, pages 2284-2291.

Upcoming papers and book chapter

H. L. Wang, T.S. Chung, Y.W. Tong, K. Jeyaseelan, A. Armugam, H.H.P. Duong, F.Fu, H.Seah, J. Yang, M. Hong. Mechanically robust and highly permeable AquaporinZ biomimetic membranes (I). (under review)

H. L. Wang, T.S. Chung, Y.W. Tong. Mechanically robust and highly permeable AquaporinZ biomimetic membranes (II). (under review).

H. L. Wang, W.Y. Xiem Y.W. Tong. Obtaining highly pure single-protein solutions from a cell broth mixture using molecularly imprinted membranes. (under review)

Patents

H. L. Wang, T.S. Chung, Y.W. Tong, Z. Chen, M. Hong, K. Jeyaseelan, A. Armugam, Aquaporin embedded biomimetic membranesPore-Spanning Biomimetic Membranes Embedded with Aquaporin. Singapore Patent Application No. 201103837-9.

W. Xie, Y. W. Tong, **H. L. Wang**, B. Wang, F. He, K. Jeyaseelan, A. Armugam, Fabrication of vesicular membranes for nano-filtration. Fabrication of Aquaporin-incorporated Vesicular Membrane for Water Purification. SG Provisional Application No. 201204108-3

Conference Papers

H. L. Wang, T.S. Chung, Y.W. Tong, K. Jeyaseelan, A. Armugam, Z. Chen, M. Hong. Ultra-Thin Pore-Spanning Biomimetic Membrane Embedded with Aquaporin Z In Forward Osmosis. North American Membrane Society (NAMS), New Orleans, USA, June 9-15, 2012.

H. L. Wang, P.S. Zhong, P.H.H. Duong, T.S. Chung, Y.W. Tong, K. Jeyaseelan, A. Armugam, Z. Chen, M. Hong. Biomimetic membranes embedded with Aquaporin Z for water reuse and desalination. Desalination for the environment clean water and energy, Barcelona, Spain, Apr 22-26, 2012.

H. L. Wang, P. Zhong, T.S. Chung, Y.W. Tong, Z. Chen, M. Hong, K. Jeyaseelan, A. Armugam, Ultrafast water permeation of biomimetic membranes embedded with Aquaporin, Singapore, APCChE, 2012.

H. L. Wang, T.S. Chung, Y.W. Tong, Z. Chen, M. Hong, K. Jeyaseelan, A. Armugam, Ultrafast water permeation of biomimetic membranes embedded with Aquaporin, AIChE annual meeting, Minneapolis Convention Center, Minneapolis, October 16-21, 2011.

H. L. Wang, T.S. Chung, Y.W. Tong, Z. Chen, M. Hong, K. Jeyaseelan, A. Armugam, Preparation and characterization of pore-suspending biomimetic membranes embedded with Aquaporin Z, North American Membrane Society (NAMS), Las Vegas, Nevada, June 4-8, 2011.